WASHINGTON UNIVERSITY

Department of Physics

Dissertation Examination Committee:
Henric Krawczynski, Chair
James Buckley
Ramanath Cowsik
Sophia Hayes
Charles Hohenburg
Martin Israel
Roger Phillips

HIGH ENERGY X-RAY AND GAMMA-RAY OBSERVATIONS OF GALAXY CLUSTERS

by

Jeremy Shane Perkins

A dissertation presented to the
Graduate School of Arts and Sciences
of Washington University in
partial fulfillment of the
requirements for the degree
of Doctor of Philosophy

April 2006

Saint Louis, Missouri

Acknowledgements

I would first like to thank all those who have taught me through the years starting with my mother and father who home-schooled me during elementary school and supported me. I had wonderful math and science teachers in high school such as Kathy Beck and Eric Unger who dedicated their time to teaching me to love the physical sciences. This continued in college and I would not have gotten here today without the guidance of Dr. Tommy Tarvin and Dr. Perry Tompkins who always pushed me into doing more and better. Without the educational background that these wonderful friends and teachers gave me, I would not be writing this now.

The most influential person to this work and my career has been my adviser, Dr. Henric Krawczynski. Without his constant help and expertise this work could not have been accomplished. Thank you very much for all of the time and energy you have invested in me. In addition to Henric, Dr. James Buckley, Dr. Marty Israel and Dr. Bob Binns have never failed to answer my questions or provided advice. I feel honored to have been able to work with you.

I would also like to thank Trevor Weekes and the VERITAS[1] collaboration for

[1] The VERITAS Collaboration is supported by the U.S. Dept. of Energy, N.S.F., the Smithsonian Institution, P.P.A.R.C. (U.K.), N.S.E.R.C. (Canada), and Enterprise-Ireland.

providing me with data and feedback. The Dean of the Graduate School of Arts and Sciences at Washington University generously provided me with a Dissertation Fellowship to enable me to complete this thesis on time. Dr. Martin Hardcastle also provided valuable assistance in the analysis of the XMM data.

Graduate school could not be done without graduate students in more ways than one: graduate students are not only the workhorses of academia but they are also friends, peers and relief valves. There is an accumulated knowledge that is carried around in graduate students' heads that is passed on from student to student and these people have given me much: Karl Kosack, Lauren Scott, Scott Hughes, Paul Rebillot, Brian Raugh, Kris Gutierrez, Kuen "Vicky" Lee, Trey Garson, Christopher Aubin, Kelley Lave, Tom Mitchel, Weylin McMillin, and many more. Thank you for everything.

Many other people in the department were vital to my research and life in general and have taught me everything from electronics and shop to the intricacies of academia as well as physics: Paul Dowkontt, Ira Jung, Richard Bose, Dana Braun, Marty Olevitch, Garry Simburger, Denny Huelsman, Tony Biondo, Todd Hardt, Sarah Jordan, Julia Hamilton, Christine Monteith, Jamie Eikmeier and Allison Verbeck.

I would like to thank my friends and neighbors who have really made St. Louis my home for these past five years. Ellen, thank you for editing many of these pages. I thank my friends at La Dolce Via for providing the espresso, food and wine that has spoiled my taste buds for years to come.

Finally, I would like to thank my wife Donna for following me to St. Louis and always being there for me. Thank you for thoroughly editing my thesis; usually you can only take so much of me talking Physics but here you endured over a hundred pages of it in a very short amount of time. I could not have done it without you.

Contents

List of Figures

List of Tables

Abstract

Galaxy clusters are the largest and most massive gravitationally bound systems in the Universe. Galaxy clusters are bright sources of X-rays owing to thermal emission of the hot intracluster medium. Furthermore, galaxy clusters might be sources of TeV gamma rays emitted by non-thermal high-energy protons and electrons accelerated by large scale structure formation shocks, galactic winds, or active galactic nuclei. In addition, gamma rays may be produced in dark matter particle annihilation processes at the cluster cores. I report on observations of the galaxy cluster 3C 129 with the XMM-Newton X-ray observatory. These observations have two major aims. First, I search for interactions of the nonthermal plasma of the large head-tail radio galaxy 3C 129 with the thermal intracluster medium. Second, I study the X-ray emission from the core of the radio galaxy. I derive an upper limit on the deficit in the ICM plasma due to the interacting radio jet which is less than the expected 10%. Additionally, I find an excess in the core emission over the Chandra observations, suggesting the presence of extended emission near the core. I also report on the search for TeV emission from the galaxy clusters Perseus and Abell 2029 using the 10 m Whipple Cherenkov telescope during the 2003-2004 and 2004-2005 observing

seasons. I apply a two-dimensional analysis technique to scrutinize the clusters for TeV emission, first determining flux upper limits on TeV gamma-ray emission from point sources within the clusters then deriving upper limits on the extended cluster emission. I subsequently compare the flux upper limits with EGRET upper limits at 100 MeV and theoretical models. Assuming that the gamma-ray surface brightness profile mimics that of the thermal X-ray emission and that the spectrum of cluster cosmic rays extends all the way from thermal energies to multi-TeV energies with a differential spectral index of -2.1, the results imply that the cosmic ray proton energy density is less than 7.9% of the thermal energy density for the Perseus cluster.

Chapter 1

Overview

Galaxy clusters are the largest and most massive gravitationally bound structures in the Universe. The most important components of galaxy clusters are (i) a dark matter halo which defines the gravitational potential of the cluster, (ii) the intracluster medium which contains the major fraction of the cluster barions and consists of hot thermal gas, cosmic rays and magnetic fields, and (iii) galaxies which move in the dark matter potential and contain most of the stars of the cluster.

In this thesis, I studied clusters with the X-ray observatory XMM-Newton and the Whipple 10m gamma-ray telescope. I combined XMM-Newton observations of the galaxy cluster 3C 129 (named after the radio galaxy it contains) with radio observations of the archetypical head-tail radio galaxy 3C 129 to study the interaction of the plasma of the radio galaxy with the intracluster medium. For this purpose, I conducted a search for cavities in the X-ray emitting gas. Furthermore, I scrutinized the X-ray emission from the head of the radio galaxy searching for evidence of emission

from shocked gas ahead of the radio core. The results constrain the nature of the radio emitting plasma in the tail of the radio galaxy and the interaction of the radio galaxy with the cluster gas.

As part of the VERITAS collaboration, I observed the Perseus and Abell 2029 galaxy clusters with the Whipple 10m Cherenkov telescope. While X-ray observations give information about the hot thermal gas, gamma-ray observations allow us to study non-thermal high-energy particle populations. In particular, TeV gamma-ray observations make it possible to search for "Cosmological Cosmic Rays" that accumulate over the total lifetime of the clusters. Combining the TeV gamma-ray observations with archival X-ray observations allowed me to constrain the ratio between the intracluster energy density in thermal plasma and in the non-thermal Cosmological Cosmic Rays. I complemented the cluster observations with observations of the Crab Nebula (a steady well calibrated source of TeV gamma-rays) at different locations in the field of view of the telescope and with Monte Carlo simulations to determine the sensitivity of the Whipple telescope for extended sources.

In addition to analyzing data, I worked on the development of Cadmium Zinc Telluride (CZT) detectors. CZT is a high-Z large bandgap semiconductor for the room-temperature detection of hard X-rays. CZT detectors find application in space-borne X-ray astronomy, medical imaging, and homeland security devices. Owing its good energy resolution and excellent spatial resolution, CZT detectors are expected to play an important role in many future space-based X-ray missions, as the hard X-ray detectors on board of Constellation-X, NuSTAR and EXIST. I used CZT substrates

from a variety of manufacturers to test the effects of different contact-materials using electron beam deposition. I programmed the data acquisition with a 500 MHz oscilloscope and set up a four point measurement of the surface conductivity. Furthermore, I evaluated the possibility to correct the charge measured at the pixels of the detector for the depth of the interaction below pixels.

The rest of the thesis is structured as follows: I will first introduce the astrophysics of galaxy clusters, focusing on their very high energy emission (Chapter 2). In Chapter 3, I will give an overview of the observatories used to acquire the results obtained in my thesis. Following this, I describe the X-ray observations of the galaxy cluster 3C 129 in Chapter 4 and the TeV gamma-ray observations of the Perseus and Abell 2029 galaxy clusters in Chapter 5. I describe the results of the CZT research in Chapter 6. I conclude with a discussion of future directions in the study of gamma-ray emission from galaxy clusters and future X-ray and gamma-ray observatories in Chapter 7. In Appendices A and B, I summarize the properties of the XMM data set and the Whipple 10m data sets, respectively. In Appendix C, I describe the I-V measurement set-up. In Appendices D and E, I describe the CZT data acquisition system and the method used to derive upper limits.

Chapter 2

Introduction

The phenomenology of galaxy clusters spans an enormous range in sizes and time scales. Clusters can contain hundreds of individual galaxies that are gravitationally bound to a large central cusp of dark matter. The most massive clusters are the largest gravitationally bound objects in the universe and can contain up to $10^{15} M_{\odot}$ down to the smallest clusters with only $10^{10} M_{\odot}$. The closest massive clusters are the Virgo, Perseus and Coma clusters at distances of 16, 75, and 99 Mpc from us. The most distant cluster detected so far is RDCS0848.6+4453 at a redshift of 1.24 (Rosati et al., 2004). The intra-cluster medium (ICM) of a cluster, made up of an optically thin hot gas, has more mass than all the cluster galaxies together. Clusters are additionally a promising testing ground for dark matter studies since they are thought to form around a large central dark matter cusp.

Clusters of galaxies have inspired intensive astrophysical study at all wavelengths. Clusters are ideal cosmological laboratories and allow for the study of structure for-

mation, dark matter and cosmology. With the advent of High Energy Astrophysics a new window of cluster research has been opened with spectacular results coming from the X-ray observatories, Einstein (or HEAO-2, launched in 1981) then ROSAT (launched in 1990) and ASCA (or Astro-D, launched in 1993). These early observatories provided a wealth of information about the composition and structure of clusters. The next generation of imaging-spectrometer observatories (the early satellites were either spectrometers or imagers but not both), Chandra and XMM-Newton (both launched in 1999) expanded on this by incorporating the best aspects of the previous generation. Multiwavelength studies of clusters using radio, microwave, optical and X-ray bands allow astrophysicists to observe interactions of thermal and non-thermal plasmas, and to study the magnetic field.

In this theses, I present Very High Energy (VHE)[1] observations of two galaxy clusters, Perseus and Abell 2029 and Low Energy (LE) [2] observations of the galaxy cluster, 3C 129. The addition of new tools is constantly needed to provide improved results and I will describe several recent instruments and developments in the field of High Energy astrophysics. In galaxy clusters, collisionless structure formation shocks are thought to be the main agents responsible for heating the ICM to temperatures of $k_{\rm B}{\rm T}\simeq$10 keV. Through this and other processes, gravitational energy is converted into the random kinetic energy of non-thermal baryons (protons) and leptons (electrons). Galactic winds (Völk and Atoyan, 1999) and re-acceleration of mildly rel-

[1] 100 GeV - 100 TeV

[2] 0.1 keV - 10 keV

ativistic particles injected into the ICM by powerful cluster members (Enßlin and Biermann, 1998) may accelerate additional particles to non-thermal energies. Using galactic cosmic rays (CR) as a yard stick, one expects that the energy density of cosmic ray protons (CRp) dominates over cosmic ray electrons (CRe) by approximately two orders of magnitude, and may be comparable to thermal particles and the ICM magnetic field. CRp can divisively escape clusters only on time scales much longer than the Hubble time. Therefore, they accumulate over the entire formation history (Völk and Atoyan, 1999).

2.1 Three Archetypical Galaxy Clusters

2.1.1 The Perseus Cluster

The Perseus cluster of galaxies[3] (Abell 426 or Perseus A) within the Perseus constellation is at a distance of 75 Mpc ($z = 0.0179$) from us and has a total mass of $4{\times}10^{14}$ $M_{\odot}$; making it one of the largest and closest galaxy clusters (Girardi et al., 1998). As such, it is one of the most studied clusters at all wavelengths and has provided some interesting results.

Optical

The Perseus cluster is one of the largest objects in the sky and numerous optical studies of the cluster exist (see Figure 2.1 for an example). The Central Dominant (CD) galaxy, NGC 1275, was one of the prototypical group of six galaxies studied by

[3] RA: 03h 19m 13s Dec: 41d 33' 00" Epoch 2000

FIGURE 2.1: Optical image of the Perseus cluster of galaxies. Each of the extended sources in this image are individual galaxies. The size of the image is approximately 14 by 21 arcminutes (Image Credit: Jim Misty, Misti Mountain Observatory).

Seyfert giving rise to the name Seyfert galaxy (Seyfert, 1943). Recently, the Hubble telescope provided a spectacular view of the central region of the cluster (Figure 2.2).

One of the most intriguing optical results about NGC 1275 was the discovery of ionized gas filaments in the Hα band (Conselice et al., 2001) which may be interpreted as explosive outflow, slow inflow (cooling flow) or heating by galaxy collisions. Based upon the information provided throughout the spectrum, cooling flows seem the most likely interpretation (Pedlar et al., 1990). There are two distinct velocity components of $\sim$ 50000 and $\sim$ 8000km s^{-1}. The higher component cannot correspond to outflow but is associated with an in-falling spiral galaxy giving rise to low-velocity filaments that are exceptionally bright (Pedlar et al., 1990).

Radio

Edge et al. (1959) cataloged the radio source 3C 84.0 which is now associated with NGC 1275, the CD galaxy of the Perseus cluster (Shakeshaft et al. (1955) cataloged this as 2C 296 previously). Miley and Perola (1975) first identified an extensive radio structure associated with NGC 1275 which is now cataloged as a radio loud giant elliptical galaxy. The relativistic electrons are accelerated relatively inefficiently and

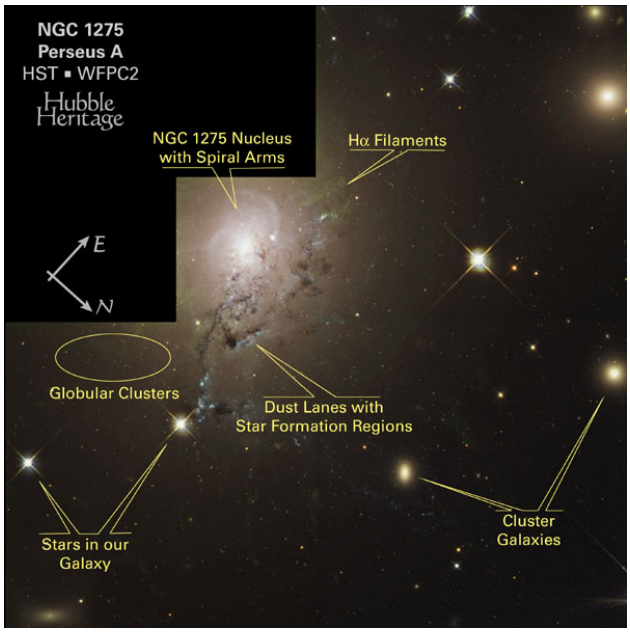

FIGURE 2.2: Hubble image taken with the Wide Field Planetary Camera 2 showing traces of spiral structure with dust lanes and blue active star forming regions. These features are taken as evidence that a spiral galaxy is falling in to the CD elliptical galaxy NGC 1275.

may significantly contribute to the production of the thermal X-ray emitting gas (Pedlar et al., 1990). Recent observations by Romney et al. (1996) using VLBI have displayed several unusual features including a counter-jet. See Figure 2.3 for an example of the structure seen with radio observations.

X-Ray

The Perseus cluster is the brightest X-ray cluster in the sky and has been studied by all X-ray telescopes (Fabian et al., 1974, 1981) and labeled as the prototypical Cooling Flow Galaxy cluster (see Section below). The X-ray emission is mainly due to thermal bremsstrahlung and line radiation (typical for clusters) from the hot ICM and is centered on NCG 1275. The emission is highly peaked towards this CD galaxy and ROSAT and Chandra observations have shown that radio sources can inflate bubbles in the intracluster medium. Radio plasma replacing hot ICM has been detected as cavities in the ICM X-ray surface brightness distribution. Fabian

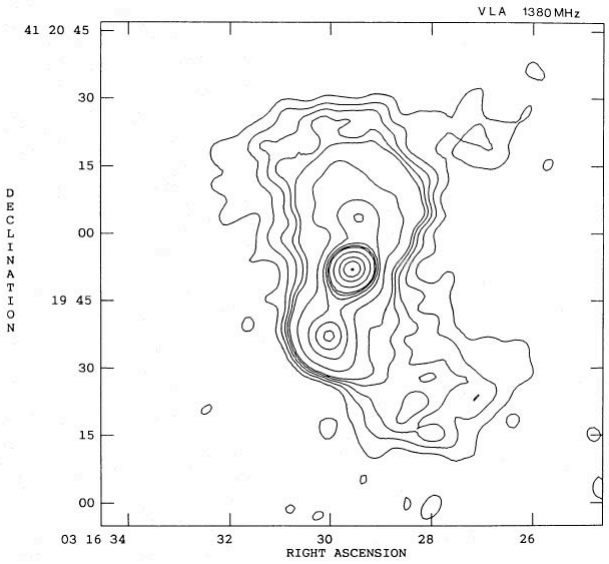

FIGURE 2.3: VLA contour map of the CD galaxy 3C 84 within the Perseus cluster of Galaxies at 90 cm. The contours are shown at 20, 40, 60, 80, 100, 200, 400, 600, 800, 1000, 2000, 4000, 6000 mJy beam^{-1} (from Pedlar et al. (1990)).

et al. (2006) have performed the most detailed study of bubbles in the Perseus cluster (900 ks of good exposure time) to date using the Chandra observatory. Fabian et al. (2006) suggests that the energy of the central radio source is dissipated by conduction and sound waves propagating through the isothermal ICM. They support this claim by showing ripples surrounding the cavities. Figure 2.4 details the results from this spectacular observation and shows the presence of large cavities where the central source has "blown" out the ICM.

One of the most pressing issues in the field of cluster astrophysics is the source of heating of the ICM at their cores. It can be seen from numerous cooling flow clusters that the gas is cooled toward the center via rapid radiative cooling but not as much as one would expect as evident from the lack of dense cool regions with ICM temperatures, $k_B T < 1$ keV (see Fabian (1994) or Gutierrez and Krawczynski (2005)). Bubbles formed by central Active Galactic Nuclei (AGN) might counteract the expected cooling towards the centers of these clusters (Böhringer et al., 2002;

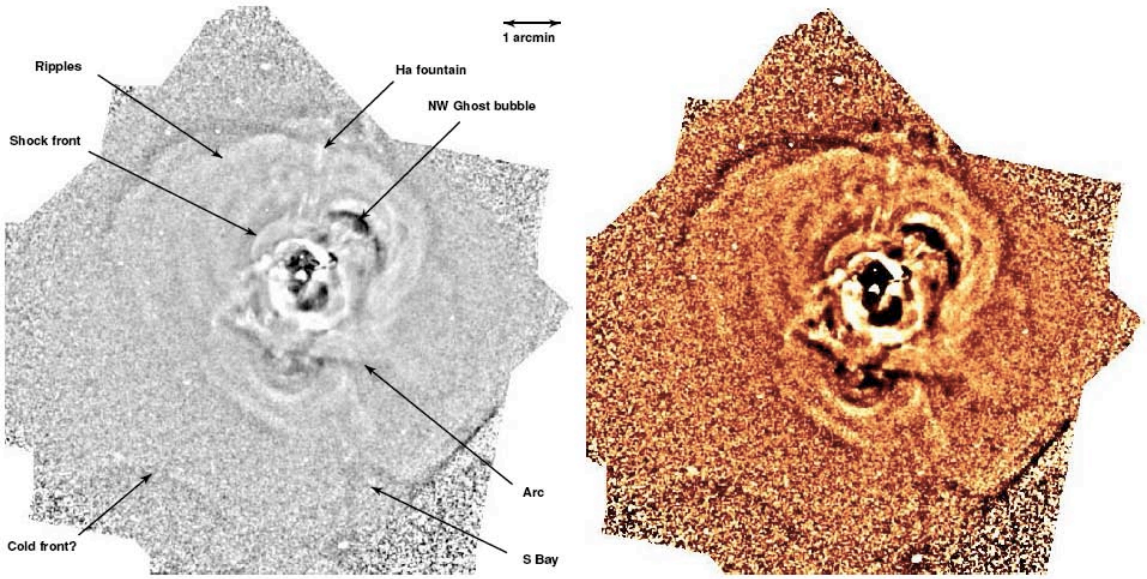

FIGURE 2.4: Chandra image (0.3-7 keV) of the Perseus cluster of galaxies from Fabian et al. (2006). The features labeled on the lower contrast image on the left incorporate some of the most diverse cluster physics including shock fronts, cold fronts, ripples, jets and bubbles.

Churazov et al., 2002). These bubbles might produce shocks, ripples, or the sound waves such as those seen in the Perseus cluster, and are possible sources for VHE emission. The bubbles might also heat the ICM through dissipation or PdV work on the ICM (see Donahue and Voit (2004) or Gutierrez and Krawczynski (2005) and the references therein).

2.1.2 Abell 2029

Abell 2029,[4] is at a distance of $z = 0.0775$, almost seven times farther away than Perseus. Although it is much smaller on the sky, its mass ($5{\times}10^{14}$ $M_{\odot}$) is actually

[4] RA: 05h 10m 58.7s Dec: 05d 45′ 42″

slightly higher than Perseus (Girardi et al., 1998). Abell 2029 is also a CD cluster and emits strongly in the X-ray band. Optical observations show that the central galaxy spans more than 600 kpc, making it one of the largest known galaxies in the Universe (Uson et al., 1991). They also show very few star forming regions in the central galaxy (McNamara and O'Connell, 1989).

Radio and X-ray

Abell 2029 has been studied well in X-rays and radio. Taylor et al. (1994) shows a compact radio core with two opposed jets which bend at right angles about 10″ from the core. There is some evidence that these bends occur in regions where the X-ray surface brightness is lower (see Figure 2.5). The ICM seems to be relaxed giving a cooling flow rate of $\dot{M} = 200 - 300 M_{\odot} \mathrm{yr}^{-1}$ (Clarke et al., 2004). Sarazin et al. (1992) performed higher resolution ROSAT HRI observations reveling several X-ray filaments which Taylor et al. (1994) adds are anti-correlated with the radio structure suggesting that the radio plasma is flowing through regions of low pressure. White et al. (1994) reanalyzed the same data and found contradictory results.

2.1.3 3C 129

3C 129[5] is at a distance of $z = 0.0223$ and has not been studied very extensively at optical wavelengths due to its low Galactic latitude. The central galaxy has been optically described as a weak elliptical galaxy (Colina and Perez-Fournon, 1990). X-ray observations have been numerous (Edge and Stewart, 1991; Leahy and Yin, 2000)

[5] RA: 04h 49m 09.0s Dec: 45d 00' 39"

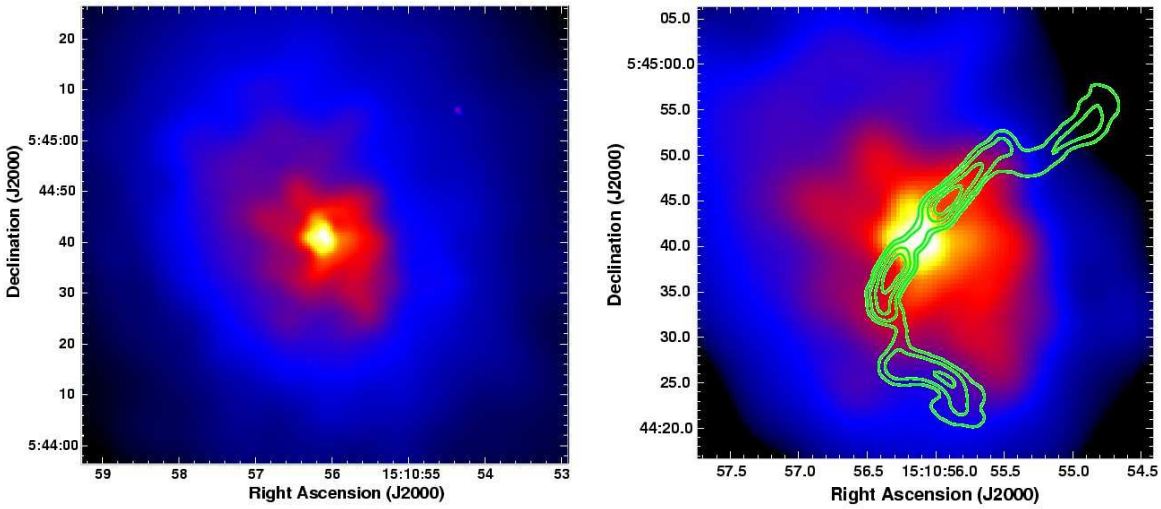

FIGURE 2.5: Chandra 0.3 - 10 keV X-ray image (adaptively smoothed) of Abell 2029. The left image is a wide angle 1.5' x 1.5' while the right one is zoomed in on the CD galaxy (50" x 50") from Clarke et al. (2004). The contours show the 1490 MHz radio emission from the CD galaxy from Taylor et al. (1994). The radio lobes seem to trace deficiencies in the X-ray surface brightness.

and have been interpreted as showing evidence for a cooling flow (Leahy and Yin, 2000), although Taylor et al. (2001) disputes this. The cluster contains two interesting radio galaxies, 3C 129 and 3C 129.1. The first is associated with the central galaxy while the second is the prototypical head-tailed galaxy with a strongly curved 15' long tail (Feretti et al., 1998). Harris et al. (2002) showed evidence for X-ray emission from the inner northern jet of 3C 129, and Krawczynski (2002) displayed evidence for an X-ray excess associated with 3C 129.1 probably produced by the CD galaxy.

Radio and X-Ray

The most interesting aspect of the galaxy cluster 3C 129 is that it harbors the prototypical tailed radio galaxy 3C 129.1. The combination of X-ray and radio observations may allow us to deduce the exact make up of the radio plasma as it propagates

through the ICM. Since the X-ray data informs us about the temperature, chemical composition, density and pressure of the ICM we can study the pressure balance between the radio plasma and the thermal gas in great detail. A pressure balance study based on various radio maps of the radio galaxy 3C 129 and on the Chandra observation of the cluster, indicates an apparent pressure mismatch between the pressure of the radio tail and the adjacent ICM. This mismatch is indicative for "dark" pressure components (like relativistic protons or magnetic field) that carry additional pressure of the radio plasma. The detection of a cavity associated with the radio tail would further constrain the composition of the radio tail plasma. This is one of the main objectives of the XMM-Newton observations described further below.

2.2 The X-Ray and Gamma-Ray Astrophysics of Galaxy Clusters

One of the most significant features of the ICM is that it emits mainly X-rays. This led to a late understanding of the ICM and clusters because the first high sensitivity X-ray observatories were launched in the late 1960s. As a whole object, clusters have a typical luminosity of 10^{44} erg/sec, which corresponds to a temperature of 10^{7} Kelvin (see Section 2.2.1).

The first cluster was detected in X-rays by Byram et al. (1966) using the Aerobee observatory. This caused much excitement in the astrophysics community and there was a rush of observing and developing of newer and more modern equipment

to better resolve clusters and consequently provide data to better explain the emission mechanism. In 1976, Iron lines were first resolved (Mitchell et al., 1976) and this placed the theory of thermal emission via bremsstrahlung on firm experimental ground. The most significant step forward in the resulting studies of clusters was the development of improved resolution observatories such as Chandra and ROSAT.

This section will focus on the general theoretical ideas explaining the X-ray emission from clusters. It will begin with thermal bremsstrahlung (the main emission mechanism in clusters) emission. From there, various VHE emission processes will be discussed that might be observable from clusters. Finally, the astrophysics specific to clusters will be presented.

2.2.1 Thermal Bremsstrahlung

When clusters were first observed in X-rays there were several different theories as to the origin of this radiation. Among those included where thermal bremsstrahlung emission, a population of individual sources and inverse Compton scattering. Of these three, thermal bremsstrahlung is the only valid model used to describe clusters today. There are several reasons to assume that the overall X-ray emission from clusters is thermal in nature and very few arguments for the other two theories. In reference to individual sources, one would expect a granularity of the cluster emission, which is not observed and would not expect to see line emissions, which is observed. As for inverse Compton emission, there should be a correlation between the radio emissions and the X-ray emissions; the spectra should behave like a power law and you would

not see line emissions. None of these conditions are met for clusters. Conversely, one would expect non-granularity, no x-ray/radio correlations, an exponential spectrum and line emissions if the cluster were emitting thermally (Sarazin, 1988).

Thermal bremsstrahlung is the radiation associated with accelerating electrons in the electrostatic fields of atoms and ions. The standard model involves a large ball of optically thin hot plasma consisting of atoms, ions and electrons populating the region between the galaxies in the cluster much like there is a plasma in the regions between stars in our own galaxy. Clusters emit thermally via bremsstrahlung emission and not black body emission because the ICM is optically thin.

The derivation of bremsstrahlung involves starting with the emission of braking/acceleration radiation of an electron as it interacts with the nucleus of an atom. This result can then be used to calculate the total emission from a plasma interacting with a gas of ions (for a detailed calculation see Longair (1992) or Jackson (1999)). The following outlines the derivation found in Longair, which indicates that the spectral emissivity of a plasma (the ICM) is

$$\kappa = \frac{1}{3\pi^2}\left(\frac{\pi}{6}\right)^{\frac{1}{2}} \frac{Z^2 e^6}{\epsilon_0^2 c^3 m_e^2}\left(\frac{m_e}{kT}\right)^{\frac{1}{2}} g(v,T) N N_e e^{-\frac{h\nu}{kT}} \tag{2.1}$$

where N and N_e are the densities of ions and electrons respectively and the *Gaunt factor* for X-rays is

$$g(v,T) = \frac{\sqrt{3}}{\pi} \ln \frac{kT}{h\nu} \tag{2.2}$$

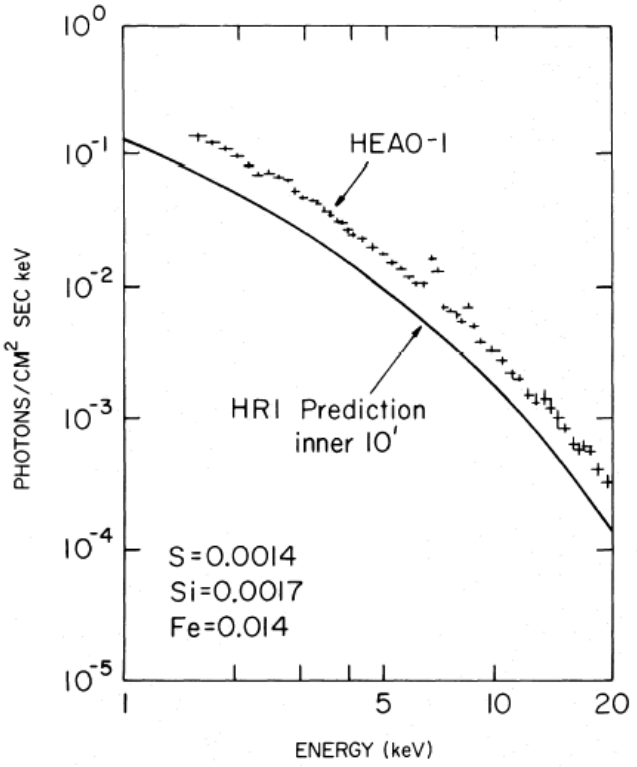

FIGURE 2.6: The total X-ray spectrum of the inner 10' of the Perseus cluster. The Iron lines are visible along with the line strengths in photons $cm^{-2}s^{-1}$. The data points are from the HEAO 1 A-2 instrument as reported by Mushotzky and Smith (1980) and the deprojected fit is from Fabian et al. (1981). The discovery of line emission was a direct indicator that the X-ray emission from clusters is thermal in nature (Figure from Fabian et al. (1981)).

At high frequencies ($h\nu \gg kT$), the *Gaunt factor* is $\propto \sqrt{(h\nu/kT)}$ and the emissivity as function of frequency drops like $\sqrt{\nu} \times \exp -h\nu/kT$. Observations of clusters have shown this to be true. Figure 2.6 demonstrates that the spectrum of the Perseus cluster follows is well described by the thermal Bremsstrahlung model. If you model this data using thermal Bremsstrahlung, the temperature of the cluster is about 10^7 K. In general, the X-ray emission from clusters can roughly be explained by single or multiple temperature Bremsstrahlung models. This result is consistent over the majority of clusters (Fabian, 1994).

Closer inspection of Figure 2.6 shows the presence of the 6.7 keV and 7.9 keV Iron lines. The presence of these lines gives the clearest evidence for the emission being thermal. These lines also support another estimate for temperature and allow for the

measuring of the ICM mass and the total mass of the cluster. There are also lines showing the presence of significant amounts of other elements with atomic number up to Iron. The similarity of the abundances (approximately solar) of these metals among multiple clusters suggests a similar evolutionary history for all clusters. In other words, clusters appear to have formed through the same type of evolutionary process independent of their present dynamical state. The nearly solar abundance of these metals in the ICM establishes that the ICM is at least partly processed matter from stars and cannot be wholly primordial matter, since primordial matter would be mainly composed of hydrogen and some helium.

2.2.2 Thermal and Non-Thermal Particles in Clusters

There are two distinct populations of particles within galaxy clusters: the thermal (ICM) and non-thermal (CRp, CRe and AGN jets). While the thermal particles interact with each other frequently and establish a thermal (Maxwellian) distribution of velocities, higher energy particles interact little with the thermal plasma. The reason for this behavior can be understood with the help of the Bethe-Bloch formula:

$$-\frac{dE}{dx} = \frac{z^2 e^4 N_e}{4\pi\epsilon_0^2 m_e v^2}\left[\ln\left(\frac{2\gamma^2 m_e v^2}{\bar{I}}\right) - \frac{v^2}{c^2}\right] \tag{2.3}$$

The formula in Equation 2.3 shows that the energy loss rate depends only upon the velocity and charge of the particles. At the lower energies (approximately non-relativistic) the ionization loss is proportional to v^{-2} or E^{-1}, but at higher energies the rate is only logarithmically dependent on E. The relative energy loss rate, $\frac{dE}{dt}/E$, is

TABLE 2.1: EGRET upper limits of the three Clusters of Galaxies presented here (Reimer et al., 2003). There have been no detections of clusters at MeV energies, and statistical interpretations of the data have been controversial.

Cluster Name	Redshift	Flux (> 100MeV) (10^{-8}cm^{-2}s^{-1})
Perseus	0.0184	< 3.72
Abell 2029	0.0768	< 7.49
3C 129	0.0223	< 5.29

very small for higher energy particles. This illustrates that the population of thermal non-relativistic particles (ICM) is dominated by interactions, while the non-thermal population suffers few interactions.

2.2.3 Possible MeV Gamma-Ray Emission

There is not a definite detection of clusters at MeV energies. There have however been statistical studies of clusters using EGRET (Energetic Gamma Ray Experiment Telescope) upper limits but these have yielded contradictory results. Each of the clusters presented in this dissertation have been observed with the EGRET observatory and the upper limits obtained from these observations are listed in Table 2.1.

Various groups have searched for cluster emission at MeV energies based on the data from the EGRET detector on board the Compton Gamma-Ray Observatory. Three studies revealed evidence at a significance level of approximately three standard deviations: Colafrancesco (2001) and Kawasaki and Totani (2002) reported an association between Abell clusters and unidentified gamma-ray point sources from

the third catalog of the EGRET experiment; Scharf and Mukherjee (2002) found gamma-ray emission from Abell clusters by stacking the EGRET data of 447 galaxy clusters. Reimer et al. (2003) analyzed data from 58 galaxy clusters and did not confirm a detection. The upper limit provided by Reimer is inconsistent with the mean flux reported by Scharf and Mukherjee (2002). In the TeV energy range, Fegan et al. (2005) reported marginal evidence for emission from Abell 1758 in the field of view of 3EG J1337 +5029.

2.2.4 VHE Gamma-Ray Emission Mechanisms

CRe lose their energy by emitting synchrotron, Bremsstrahlung, and inverse Compton emission on much shorter time scales. For ICM magnetic fields on the order of $B \simeq 1\mu$G, synchrotron and inverse Compton emission losses alone cool CRe of energy $E = 1$ TeV on a timescale

$$\tau_s = \left(\frac{4}{3} \sigma_T c \frac{B'^2}{8\pi m_e c^2} \gamma_e \right)^{-1} \tag{2.4}$$

where σ_T is the Thomson cross section, $B' = \sqrt{B^2 + B_{\rm CMB}^2}$ and $B_{\rm CMB} = 3.25(1+z)^2\mu$G; for the clusters considered here, $z \ll 1$ and $\tau_s \approx 10^6$ years. The short life-time of TeV electrons implies that they do not accumulate over the life time of the cluster. If we observed Inverse Compton TeV gamma rays from a cluster, it would come from electrons that were accelerated at most a few million years before they emitted the radiation.

There is good observational evidence for nonthermal electrons in galaxy clus-

ters. For a number of clusters, diffuse synchrotron radio halos and/or radio relic sources have been detected (Giovannini et al., 1993, 1999; Giovannini and Feretti, 2000; Kempner and Sarazin, 2001; Feretti, 2003). For some clusters, an excess of Extreme Ultra-Violet (EUV) and/or hard X-ray radiation over that expected from the thermal X-ray emitting ICM has been observed (Bowyer and Berghöfer, 1998; Lieu et al., 1999; Rephaeli et al., 1999; Fusco-Femiano et al., 2004). The excess radiation originates most likely as inverse Compton emission from CRe scattering cosmic microwave background photons (Lieu et al., 1996; Enßlin and Biermann, 1998; Blasi and Colafrancesco, 1999; Fusco-Femiano et al., 1999).

The detection of gamma-ray emission from galaxy clusters would make it possible to measure the energy density of non-thermal particles. The density and energy density of the thermal ICM can be derived from imaging-spectroscopy observations made with such satellites as Chandra and XMM-Newton (Markevitch et al., 1998; Krawczynski, 2002; Donahue et al., 2004). The density and energy spectra of the non-thermal protons could be computed from the detected gamma-ray emission once the density of the thermal ICM is known (Pfrommer and Enßlin, 2004). Gamma rays can originate as inverse Compton and Bremsstrahlung emission from CRe and as $\pi_0 \rightarrow \gamma\gamma$ emission from hadronic interactions of CRp with thermal target material. Successful measurements of the gamma-ray fluxes from several galaxy clusters would allow the correlation of the CRp luminosity with cluster mass, temperature, and redshift, and provide conclusions about how the clusters grew. Assuming CRp contribute noticeably to the pressure of the ICM, the measurements of the CRp energy density

would allow improvement on the estimates of the cluster mass based on X-ray data, and thus improve estimates of the universal baryon fraction. If CR provide pressure support to the ICM, they would inhibit star formation to some extent as they do not cool radiatively like the thermal X-ray emitting gas. However, if CRp give less pressure support than the ICM they might accelerate star formation. Furthermore, low energy cosmic ray ions might provide a source of heating the thermal gas (Rephaeli, 1977).

In addition to a CR origin, annihilating dark matter may also emit gamma rays. The intensity of the radiation depends on the nature of dark matter, the annihilation cross sections, and the dark matter density profile close to the core of the cluster (Bergström et al., 1998). While MeV observations are ideally suited for detecting the emission from the bulk of the non-thermal particles, TeV gamma-ray observations of cluster energy spectra and radial emission profiles would disentangle the various components that contribute to the emission.

The search for TeV emission from clusters described in Chapter 5 assumes that the high energy (HE) surface brightness mimics the X-ray surface brightness, and focuses on the detection of gamma rays from within 0.8 degrees from the cluster center. There are several possibilities connecting the thermal and non-thermal particles within clusters. From general considerations, Völk and Atoyan (1999) assume that the non-thermal particles carry a certain fraction of the energy density of the ICM. One of the aims of VHE astronomy is to constrain this fraction. The CRp energy density in the Interstellar Medium (ISM) of the Milky Way galaxy is comparable to

the energy density of the thermal ISM, the energy density of the interstellar magnetic field and the energy density of star light. If non-thermal particles in clusters indeed carry a certain fraction of the energy density of the ICM, the HE surface brightness would mimic that of the thermal X-ray emission. A differing argument is that powerful cluster members (i.e. radio sources) are the dominant source of non-thermal particles in the ICM. In this circumstance we would expect that CRp accumulate at the cluster cores where usually the most powerful radio galaxies are found (Pfrommer and Enßlin, 2004). Ryu et al. (2003) and Kang and Jones (2005) performed numerical calculations to estimate the energy density of CRp by large scale structure formation shocks. The simulations indicate that strong shocks form preferentially in the cluster periphery. Accordingly, most CRp would be accelerated in the outskirts of the clusters and would only slowly be transported to the cluster core by bulk plasma motion following cluster merger for example. In conclusion, the CRp distribution in galaxy clusters is uncertain as long as we have not mapped them in the light of HE photons. However, independent of the lateral profile of CRp acceleration, the emission profile is expected to be centrally peaked, as the HE emission stems from inelastic collisions of the CRps with the centrally peaked thermal target material.

2.2.5 Extragalactic Extinction

Unfortunately, the Universe is rather opaque at gamma-ray energies above 30 GeV. The primary process that removes high energy gamma rays of energy E from remote objects is absorption via $\gamma_E + \gamma_\epsilon \rightarrow e^+ + e^-$ as they move through the low

energy photons of the extragalactic background light (EBL). When the photons are in the VHE gamma-ray region they then interact as described with photons from the Infrared Background and arrive with a spectrum that has been modified by the EBL absorption. There have been notable advances in measuring the EBL and several attempts to estimate its effect on gamma-ray emission.

Figure 2.7 compares several different EBL models along with recent measurements of the EBL over a large energy range. None of the models are fully analytical. The Primack model (Primack et al., 2005) calculated the emission by using an evolving galaxy population model using semi-analytical procedures, taking into account the effects of dust which obscures the IR and re-radiates the absorption. The model by Malkan and Stecker (2001) (called Stecker here) assumed that the the dependence on galactic spectra is the same for all redshifts and added a simple luminosity evolution back to a redshift of 2. Kneiske et al. (2002) based their model directly on the observations and used a minimal set of assumptions to pinpoint the basic physics involved. Their model is very similar to the Stecker model (Malkan and Stecker, 2001), but specifically addressed the redshift evolution of the EBL as well as re-radiation. The P0.45 model from Aharonian et al. (2005) is a simple interpolation of the EBL data and is consistent with the recent detection of blazars with hard gamma-ray energy spectra at redshifts of 0.18 with the H.E.S.S. experiment.

Given a model for the EBL the optical depth can be computed as follows: the

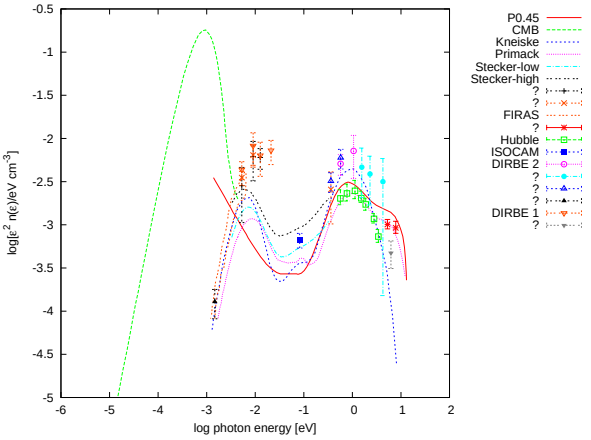

FIGURE 2.7: Extragalactic Background Light. Primack model along with data points are from Primack et al. (2005), Kneiske Z=0 model is from Kneiske et al. (2002) P0.45 is from Aharonian et al. (2005) and the Stecker models are from Malkan and Stecker (2001).

threshold energy for pair production is given by

$$\epsilon_{\rm th} = \frac{2(m_{\rm e}c^2)^2}{E(1-\mu)(1+z)^2}\,, \tag{2.5}$$

where $\mu = \cos\theta$ denotes the cosine of the scattering angle. The pair creation cross section is given by

$$\sigma_{\gamma\gamma} = \frac{3\sigma_{\rm T}}{16}(1-\beta^2)\left[2\beta(\beta^2-2) + (3-\beta^4)\ln\left(\frac{1+\beta}{1-\beta}\right)\right]{\rm cm}^2\,, \tag{2.6}$$

where $\beta = \sqrt{1-1/\gamma^2}$ with $\gamma^2 = \epsilon/\epsilon_{\rm th}$, and where $\sigma_{\rm T}$ denotes the Thomson cross section. Mannheim et al. (1996) derives the optical depth as

$$\begin{aligned}\tau_{\gamma\gamma}(E,z_\circ) &= \int_0^{z_\circ} dz \frac{dl}{dz}\int_{-1}^{+1} d\mu \frac{1-\mu}{2}\int_{\epsilon_{\rm th}}^{\infty} d\epsilon n_{\rm b}(\epsilon)(1+z)^3\sigma_{\gamma\gamma}(E,\epsilon,\mu,z) \\ &= \frac{c}{H_\circ}\int_0^{z_\circ} dz(1+z)^{1/2}\int_0^2 dx\frac{x}{2}\int_{\epsilon_{\rm th}}^{\infty} d\epsilon n_{\rm b}(\epsilon)\sigma_{\gamma\gamma}(E,\epsilon,x-1,z)\end{aligned} \tag{2.7}$$

for a non-evolving present-day background density $n_{\rm b}$, i.e., $n'_{\rm b}(z,\epsilon')d\epsilon' = (1+z)^3 n_{\rm b}(\epsilon)d\epsilon$, where the dash indicates co-moving frame quantities.

Following the procedure found in Mannheim et al. (1996) the absorption due to the EBL is computed by numerically integrating the optical depth function. Not

only does the EBL decrease the flux seen at earth but it also steepens the original spectrum. This is observed in Figure 2.8 by a greater absorption towards the high energy region of the plot. There is also a strong dependence on the redshift because these photons must travel through many more photons. The photon density evolution should be more shallow than $\propto (1+z)^3$ because the rate of star formation was higher which in turn generates more IR EBL. This is critical for the observation of clusters because the nearest ones are at a distance where this effect becomes noticeable an in selecting source candidates for GeV/TeV observations one has to target close clusters to minimize extragalactic absorption. As more massive clusters are expected to emit VHE emission more strongly, one has to balance the expected level of emission with the expected level of absorption.. Currently it is very difficult to distinguish features in the source spectrum from the EBL absorption features since the EBL is not well known in the Infrared region where the absorption of gamma rays is most pronounced and the source spectrum is also unknown. The predicted absorption is very sensitive to the model assumptions of density and luminosity evolution and redshift cutoff which can effect the output by an order of magnitude (Mannheim et al., 1996). From Figure 2.8 one can see that the effect of extragalactic extinction limits the redshift range out to which extragalactic objects can be observed at $>$ 100GeV energies to $z <\sim 0.5$.

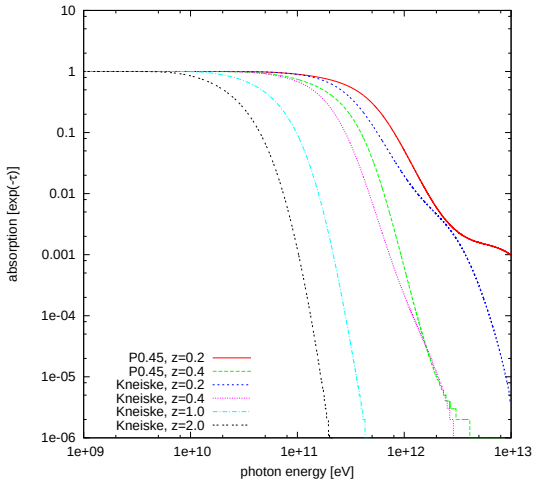

FIGURE 2.8: Absorption from the extragalactic background light based on the EBL models in Figure 2.7. Note the strong dependence on energy which appears as a sharpening of the source spectrum when convolved with the incoming photons and the redshift dependence which will determine how far out we can observe in VHE gamma rays.

2.2.6 Cooling Flows

As mentioned in Chapter 1, Cooling flows are a current topic in the study of clusters. The theory of cooling flows is an example of how our understanding of clusters has evolved from a simple model of a large ball of hot gas to one of a non-uniform dynamic system.

The cluster is held together by its own gravitational potential and thus, the density of the gas will be decreasing function of the radius. Over time, a hot gas will cool down and the radiative cooling time of a gas is dependent upon its density (a denser gas will cool faster). We can therefore assume that the cooling time is shortest in the core of a cluster and that the core of the cluster will cool the fastest (Fabian, 1994).

To understand how a cooling flow is arranged, look at a radius R from the core of the cluster. The pressure at this radius will only depend on the gas outside of R. This gas will not be as significantly affected by cooling as the gas within R as stated, so

there will be a temperature gradient across R. The pressure slightly above and below R will be practically the same and the volume will also remain roughly constant but the temperature will definitely be different due to the faster cooling inside of R. To maintain the pressure and volume at R, the density must rise to compensate for this decrease in temperature. The only way for this to happen is for matter to fall below R. This is the essence of a cooling flow, a flow of matter into the core of the cluster due to a temperature gradient within the cluster (Fabian, 1994).

An example of a cooling flow can be best displayed by comparing the surface brightness of a non-cooling flow cluster like Coma to a cooling flow cluster like Centaurus. The surface brightness of the non-cooling type will be rather flat with radius indicating a rather constant density throughout the ICM, while the cooling type will continue to rise inversely with radius all the way to the core (indicative of a dense core). The radial dependence of the temperature can be determined by examining the spectral data from the cluster. For cooling flow clusters the temperature should decrease as you travel towards the core and this has partially been observed.

Observing the luminosity within the cooling region (i.e. where the cooling rate is significantly small) and with the assumption that this luminosity is only due to the thermal energy of the gas and the PdV work done on the gas as it falls into the potential well of the cluster in the cooling flow, then $L = \frac{5\dot{M}}{2\mu m}kT$ where $\dot{M}$, μ and m are the mass deposition rate, the mean molecular mass, and the proton mass respectively. With the luminosity of the cooling region known the mass deposition rate can be determined from this equation. The mass deposition rate, measured in

solar masses per year, ranges from 0 to > 500 with 50 - 100 being typical values (Fabian, 1994).

As cool ICM is deposited into the center of the cluster, one would expect the formation of either cold clouds or gravitational collapse into star formation. However, observations with Chandra and XMM-Newton did not find cold gas with $k_B T < 1$keV (Peterson et al., 2004). The predicted star formation regions have also not been found. There are many models to explain the failure of the cooling flow model including the heating of the ICM by central AGN or a higher thermal conductivity of the ICM preventing the rapid cooling of the center (Donahue and Voit, 2004; Blanton, 2004). The search for evidence with respect to these theories is a continuing field of study.

Overall, there are numerous phenomenon available for study in clusters. The ICM radiates mainly in the X-ray via thermal Bremsstrahlung emission which allows for the measurement of composition and temperature of the cluster and the spatial distribution of dark matter. Based on the current understanding of clusters, one would expect to find evidence of cool, dense cores but the lack of this evidence of such features has led to the search for a type of heating at the core. There is evidence for non-thermal emission from clusters due to the observations of radio galaxies and AGN within clusters. Several studies have been made to look for MeV emission from clusters but the results remain inconclusive and more observations at higher energies are needed. At the highest of energies, extragalactic extinction becomes relevant and one can only observe the closest most massive clusters.

Chapter 3

X-Ray and Gamma-Ray Observatories

The data presented in this dissertation were collected with several different observatories including the orbiting observatories, XMM-Newton and Chandra, and the ground-based Whipple 10m Gamma-ray Telescope in Amado, Arizona. In this chapter I describe the instruments and techniques used to detect photons in each of these experiments.

3.1 X-Ray Observatories

In the high energy range of 100 eV to several keV, observations are best achieved in space. In this range, the atmosphere absorbs the radiation and reasonably-sized detectors can register a sufficient number of photons to warrant sensitive observa-

tions. Modern missions use solid state detectors to detect the photons and there are currently two major observatories, Chandra and XMM-Newton. These instruments, while using the same basic detector technique, are very different in terms of their angular resolution and effective area. Chandra has approximately forty times the angular resolution of XMM (X-ray Multi Mirror) while XMM has a much larger (6x) detection area.

3.1.1 Solid State Detectors

Both Chandra and XMM-Newton use Silicon-based Charged Coupled Devices (CCDs) to detect X-ray photons from astrophysical objects. A CCD is an array of MOS diodes, except in the case of the PN detectors on board the XMM-Newton detector (see Section 3.1.2). When a photon interacts with the substrate material (usually p-type Silicon), it creates a number of electron-hole pairs dependent on the energy of the original photon. The initial MOS diode is biased in such a way that the charge is contained within the single MOS detector. On readout, the charge is transferred along each individual array element (or pixel) towards a readout element where it is then digitized. The importance in terms of high energy astrophysics is that the response of the detector can be tuned to the energy region of interest. These types of detectors can be very compact with the FET amplifier built on the chips themselves. The technology has progressed to minimize the cost and provide very mature instruments.

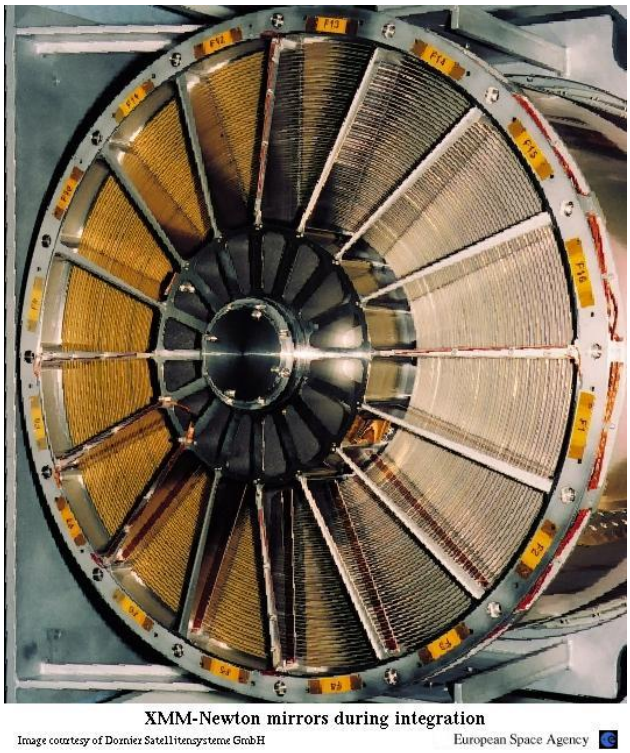

FIGURE 3.1: The grazing incidence mirrors on the XMM - Newton Observatory (image courtesy of Dornier Satellitensysteme GmbH and ESA).

3.1.2 XMM-Newton

The XMM-Newton satellite (see Figure 3.2) is the largest scientific observatory ever launched by the European Space Agency (ESA), weighing 4 tonnes and over 10 m long. It includes two Reflection Grating Spectrometers and EPIC (European Photon Imaging Camera) PN imaging CCD, two EPIC MOS imaging CCDs, as well as the three grazing incidence mirror modules necessary to focus X-rays onto these chips. The XMM observatory also includes an optical monitor. There are three focusing mirrors (one for each detector), consisting of 58 individual Wolter I mirrors nested in a coaxial and confocal configuration (Figure 3.1). The total focal length of the telescopes is 7.5 m. This configuration allows for a large collecting area (1500 cm^2) over a wide energy band (Jansen et al., 2001). In the focal plane of these mirrors lie

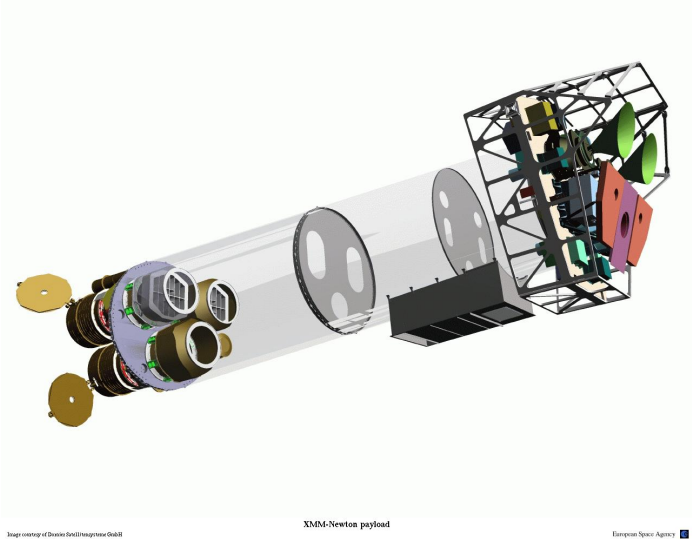

FIGURE 3.2: Transparent view of the XMM-Newton observatory. On the left are the three X-ray telescopes consisting of the X-ray focusing modules. On the right is the back end of the instrument with the CCDs and other electronics (image courtesy of Dornier Satellitensysteme GmbH and ESA).

the two MOS and single PN detectors.

MOS X-ray CCDs

Each MOS detector contains seven individual CCDs arranged with a single chip in the center surrounded by six others forming the total imaging area of $\sim 2.5 \times 2.5$ cm. The center chip is directly at the focal point of the telescope while the other 6 are shifted toward the mirror slightly to compensate for the curvature of the focal plane and to improve the point spread function (PSF) toward the edges of the detector. Each CCD is a three-phase frame transfer device on high resistivity epitaxial Silicon. The total detector has a total of 600 x 600, 40 micron square pixels each covering 1.1 x 1.1 arcseconds on the field of view. It is important to note that 15 pixels is approximately the PSF half energy width of 15". The useful energy range of these CCDs is about 0.2 to 10 keV but the energy response below $\sim$ 700 eV is poor (Turner et al., 2001). Figure 3.3 shows the quantum efficiency (QE) of the MOS CCDs.

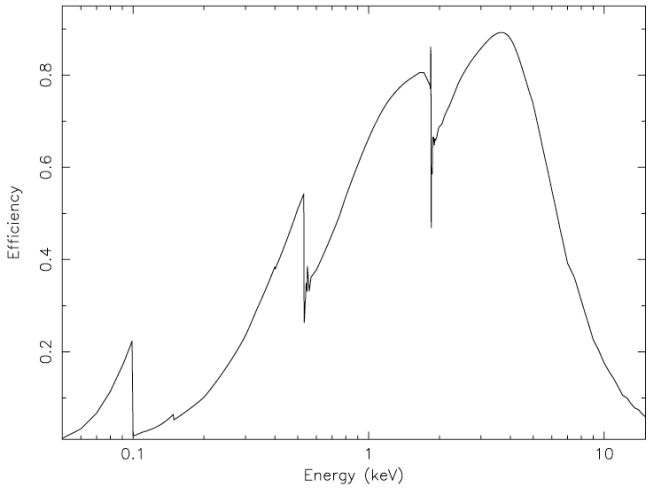

FIGURE 3.3: The X-ray quantum efficiency of the EPIC MOS CCDs based on ground based calibrations using the Orsay synchrotron (Pigot et al., 1999; Trifoglio et al., 1998) and celestrial source measurements since launch (Turner et al., 2001). These data are useful in determining the effective energy region in which to observe an object.

The MOS imagers are behind a filter wheel containing four possible choices of filtering (in addition to the light and UV blocking filters). Two of the filters are thin films made of 1600 Å poly-imide with 400 Å aluminum on one side. There is also a medium filter with the same substrate but 800 Å of aluminum and a thick filter with 3300 Å of Polypropylene with 1100 Å of aluminum and 450 Å of tin. The choice of filter is determined by the strength of the source. There are also open and closed filters available. The open mode is only used for very dim fields of view while the closed position is used during periods of high proton fluxes and is also useful for particle background measurements (Turner et al., 2001).

PN X-ray CCDs

The other CCD residing in the focal plane of the X-ray telescope is a type of Silicon drift detector. These are fully depleted CCDs with a thickness of 300μm which differs from the MOS detectors and the CCDs used on Chandra. The leading benefit from this type of detector is a high detection efficiency above 5 keV. The pixel

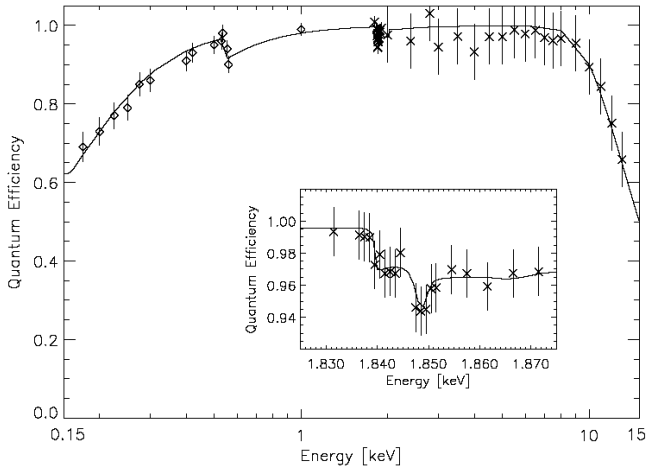

FIGURE 3.4: The X-ray quantum efficiency of the EPIC PN CCD based on ground based calibrations using the Orsay synchrotron (Pigot et al., 1999; Trifoglio et al., 1998) and celestrial source measurements since launch (Strüder et al., 2001). These data are useful in determining the effective energy region in which to observe an object. The QE of the PN is much flatter over the full energy range than the MOS detectors on board XMM, which decreases substantially above 5 keV.

size can be tailored to the X-ray optics and results in a combined angular resolution of 3.3 arcsecond. The full detector is made up of twelve individual chips arranged in a rectangular grid with a sensitive area of 36cm^2. The detector is cooled to $-90°C$ which provides a leakage current less than 0.1 electrons per pixel over a readout cycle of 73 ms. The quantum efficiency of the PN detector is flatter over the full energy range than the MOS detector and can be seen in Figure 3.4 (Strüder et al., 2001).

Optical

The addition of the optical and UV imagers on board the XMM-Newton observatory allows simultaneous observations of objects over a very broad energy range. The coverage extends the range of the observatory between 170 to 650 nm and is focused on the central 17 arcmin of the X-ray FOV. In addition to being able to image objects with great sensitivity due to low background using several on-board filters, the

instrument can also perform spectroscopy using a grism. At the focal plane of this instrument is a microchannelplate-intensified CCD (Mason et al., 2001).

3.1.3 Chandra

The Chandra X-Ray Observatory is one of NASA's "Great Observatories", which was put into orbit by the space shuttle Columbia and was then propelled into a very elliptical orbit by a second rocket system. This highly elliptical orbit (140,000 km apogee and 10,000 km perigee) provides very long observing times (up to two days) and low Earth occultion. The main on-board instrument is the X-Ray telescope focused on the ACIS CCDs (Weisskopf et al., 2002).

The Chandra X-ray Observatory Advanced CCD Imaging Spectrometer (ACIS) consists of ten individual CCDs, four of which are arranged in a square setting specifically for imaging purposes. The other six CCDs are used mainly for spectroscopy and are aligned in a linear array. The center four chips are front illuminated as are five of the chips in the spectroscopy array, except one which is back illuminated and useful for imaging soft objects. The primary advantage of this instrument is that it is possible to resolve an object to better than 0.5 arcsecond resolution (or three times better than XMM) (Garmire et al., 2003). The field of view of Chandra, however, is 17 arcminutes compared to over 28 arcminutes for XMM. The Quantum Efficiency (QE, seen in Figure 3.5) is similar to the QE of the MOS detector on board the XMM observatory.

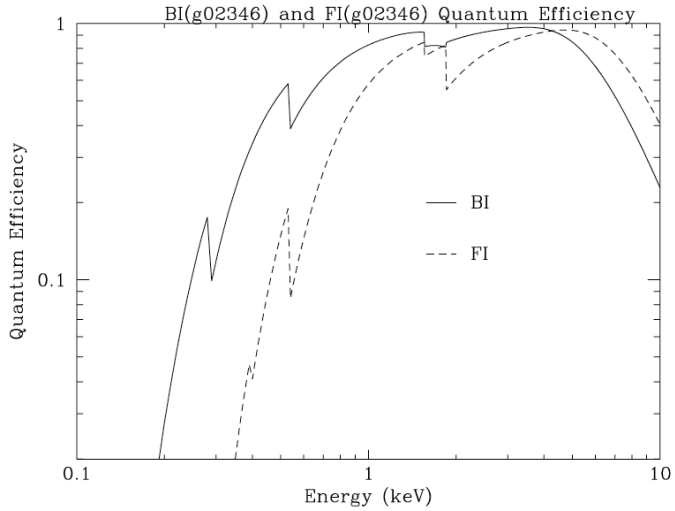

FIGURE 3.5: The X-ray quantum efficiency of the ASIC CCDs on the Chandra X-Ray observatory. Nine of the detectors are front illuminated (FI) and one is back illuminated (BI), useful for imaging soft objects (Garmire et al., 2003).

3.2 The Whipple Gamma-Ray Observatory

Above 10 eV our atmosphere is opaque, and to detect radiation from astronomical sources at energies above this we must either use space-based platforms or develop alternate techniques. Due to the low number of photons at TeV energies, the size of space based observatories would be prohibitively large in this energy range. Over the past forty years, scientists from Ireland, the U.K., the U.S.A., and Germany developed the atmospheric Cherenkov technique to detect the highest energy photons from the ground using the atmosphere as a detector medium. Astrophysicists continued to refine this method leading to the definite detection (20 sigma) of the Crab Nebula in 1986 by the Whipple 10m Imaging Atmospheric Cherenkov Telescope (IACT) (Weekes et al., 1989) (see Figure 3.6).

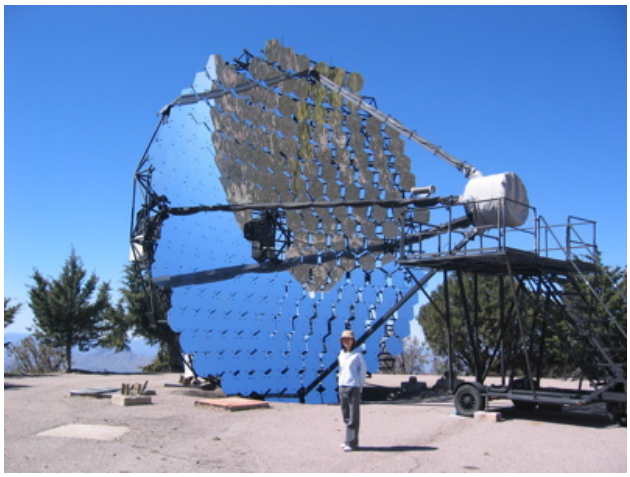

FIGURE 3.6: The Whipple 10m Imaging Atmospheric Cherenkov Telescope located on Mt. Hopkins near Amado, AZ. This instrument was the first to solidly detect VHE gamma rays from the Crab nebula in 1986 (Weekes et al., 1989). Even though it is over twenty years old, it is still a viable scientific instrument.

3.2.1 The Imaging Atmospheric Cherenkov Technique

Even though the atmosphere is opaque to photons above a certain energy, it is possible to observe objects at the highest energies by collecting the light associated with the interaction of this radiation with the atmosphere. When a high-energy photon enters the earth's atmosphere, it interacts with the atoms and molecules found there by pair-production, creating an electron and a positron. The extra energy imparted to this pair (anything belonging to the original photon above the minimum energy) is usually enough to propel these charged particles beyond the speed of light in the current medium, thus producing Cherenkov radiation. Once these primary particles have traveled approximately one radiation length, they interact with the surrounding air molecules and emit secondary gamma-rays via bremsstrahlung emission. These secondary gamma-rays then pair-produce and the process continues until the ionization losses and radiation losses equilibriate and the shower gradually diminishes (see Figure 3.7 for a diagram of the process). The remarkable part of this process in terms of IACTs is that the Cherenkov radiation is coherent and strongly beamed forward.

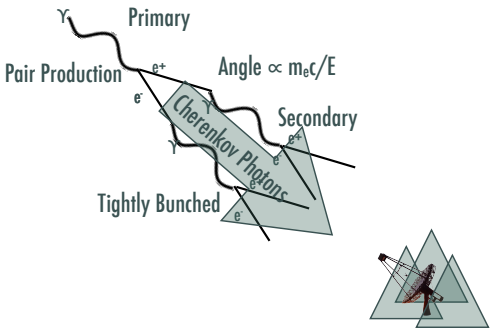

]

FIGURE 3.7: The primary components of a gamma-ray shower. The primary photon interacts via pair-production with the atmosphere. These secondary particles then emit bremsstrahlung radiation which in turn pair-produces creating a cascade of particles. The charged particles produced within the shower are traveling faster than the speed of light in air and emit Cherenkov radiation which is then detected by a ground based IACT.

This secondary radiation is what is detected in IACTs.

Pair production occurs when an incident gamma-ray interacts within the ambient electric field of a nucleus (in order to conserve energy and momentum) and is completely annihilated producing an electron pair $\gamma \rightarrow e^+ + e^-$. The energy of the original photon must be above the rest energy of the products (1.02 MeV) and any additional energy is converted into the kinetic energy of the pair. Thus, the pair is strongly beamed forward and if the total energy of the product is known, the initial energy of the incident photon can be determined which is important in determining the spectra of sources.

Cherenkov radiation occurs when a charged particle moves faster than light in a given dialectric medium. This is analogous to a supersonic shock in air for objects traveling faster than the local speed of sound. The leading properties of this phenomenon in terms of IACTs is that it is macroscopic, the medium rather than the

particle is emitting, and it is low energy. Figure 3.8 demonstrates what happens when a charged particle moves through a dialectric medium, interacting with the molecules in the immediate vicinity, polarizing them. When the particle is non-relativistic, the disturbance is symmetrical around the particle and there is no detectable radiation. The situation is different when the particle is moving at a relativistic speed (i.e. when the velocity exceeds c/n where n is the refractive index). The material cannot maintain and there is a resultant dipole field in the medium which produces detectable radiation. Although there is a general canceling of the radiation due to the cylindrical symmetry, there is coherent radiation in the forward direction (see Figure 3.9). Which is detectable from the ground.

To observers on the ground, Cherenkov radiation from an electromagnetic cascade is a glowing column of light that is dim but coherent, thus, a simple light detector should suffice for the determination of the main quantities to be determined. From an observational point of view, the point of origin, the energy, and the time of arrival of the initial photon needs to be established. The point of origin can be determined because showers are highly collimated, the energy is derived from the shower brightness, and the initial photon arrival is easily concluded because the shower durations are on the order of one nanosecond. Since the atmosphere is part of the detecting technique, everything from temperature, pressure, and humidity will confound the telescope yet determining these effects can be difficult or impossible. However, these effects have been proven to be nominal by the fact that this technique works. For example, observations of the Crab Nebula, the standard candle of TeV gamma-ray

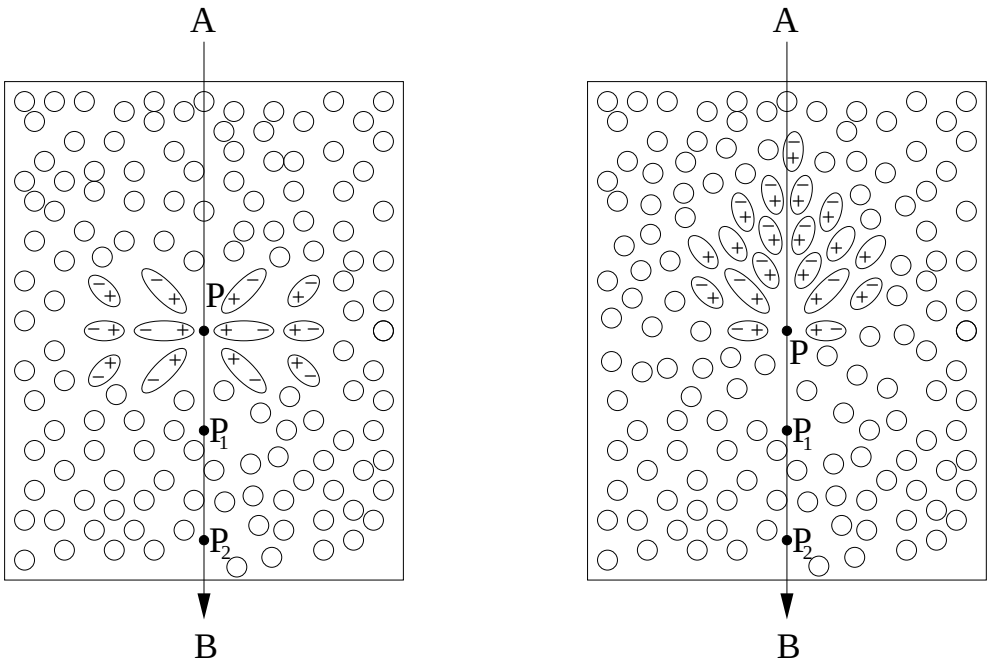

FIGURE 3.8: The effects of a charged particle moving through a dialectric medium. The figure on the left is for a non-relativistic particle while the one on the right is for a relativistic one (figure courtesy of D. Horan adapted from Jelley (1958)).

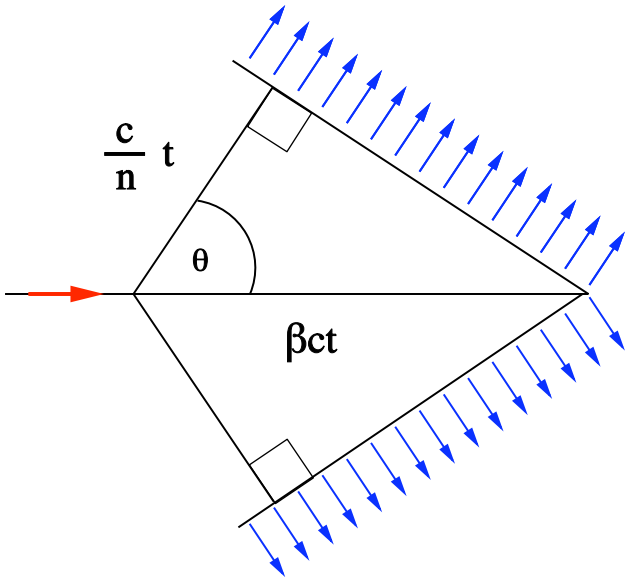

FIGURE 3.9: Diagram of the coherent Cherenkov emission by a charged particle moving faster than light in a dialectric medium. In this figure, v is the velocity of the particle (indicated by the red arrow), $\beta = v/c$ and n is the refractive index of the medium. From the geometry of the figure, one can see that $\cos\theta = 1/n\beta$ with θ being the emission angle of the photons (blue arrows) (figure from `http://wikipedia.org`).

astronomy, with different telescopes yield consistent flux levels and energy spectra. Inclement weather is another matter and observations are only done on clear nights which is why most telescopes are placed in dry areas with little pollution. The light collectors needed for ACTs do not need to be precise because the size of the shower is approximately 1.5° to 2.0° and the smallest structures are a few arcminutes in size; assuming a resolution of a few arcminutes and a field of view of a few degrees, we can image the shower. One of the most beneficial properties of IACTs is that the detection area is determined by the size of the light pool, approximately $5 \times 10^4 \mathrm{m}^2$, and not by the size of the telescope itself.

The Imaging Atmospheric Cherenkov Technique is background dominated and there are several phenomena that contribute to the background. The first is the sky brightness which can affect the energy threshold by prohibiting the detection of the dimmest (low energy) showers. There are several ways to accommodate this; the first is to choose light collectors (usually photo-multiplier tubes) that are most responsive in the wavelengths where the Cherenkov emission is the brightest and where the background light happens to be the lowest. The background lights also appear as a constant current in the PMTs, and by setting the trigger threshold above this most of the background can be ignored (although this still affects the energy threshold). The second, and more troubling source of background, are charged cosmic rays which can also produce an electromagnetic shower. There are 10^3 to 10^4 times more cosmic ray showers than gamma-ray and while they are superficially similar there are differences that can be used to differentiate them. Cosmic ray showers are 'messy' in shape and

contain hadronic interactions while gamma-ray induced air showers are 'clean' and contain only electrons, positrons, and photons. Cosmic ray showers are incoherent, wide, and long while gamma-ray showers are coherent, narrow, and short. Figure 3.10 displays a diagram of a cosmic ray shower compared to gamma-ray shower illustrating the differences between the two. Aside from the night sky background and cosmic ray showers, electrons also produce background but only at the lowest energies. The main task during the analysis process is to determine which events are gammas and which are hadrons.

The first generation of Atmospheric Cherenkov telescopes were non-imaging, and could only differentiate the night sky background from shower like events. It was not until the advent of the imaging technique that gamma hadron separation was achieved. Instead of using a single light detector in the focal plane of the dish, a 'camera' (see Figure 3.12) made up multiple PMTs is used to roughly image the shower. From the geometry of the shower, we can determine whether the shower event was initiated by gammas or by hadrons. From simulations, we can determine that the physics of the shower is directly responsible for the geometry of the shower, and from these determine the cuts used to differentiate gammas and hadrons (See Section 5.1.2. Figure 3.11 illustrates some examples of different showers look like in the camera. As gamma-ray induced air showers are detected in many pixels of the camera, and Cherenkov telescopes can achieve angular resolutions which are better than both the pixel size and the optical quality of the mirrors. The energy of the primary ray can be determined from the Cherenkov light intensity. For single telescopes, the

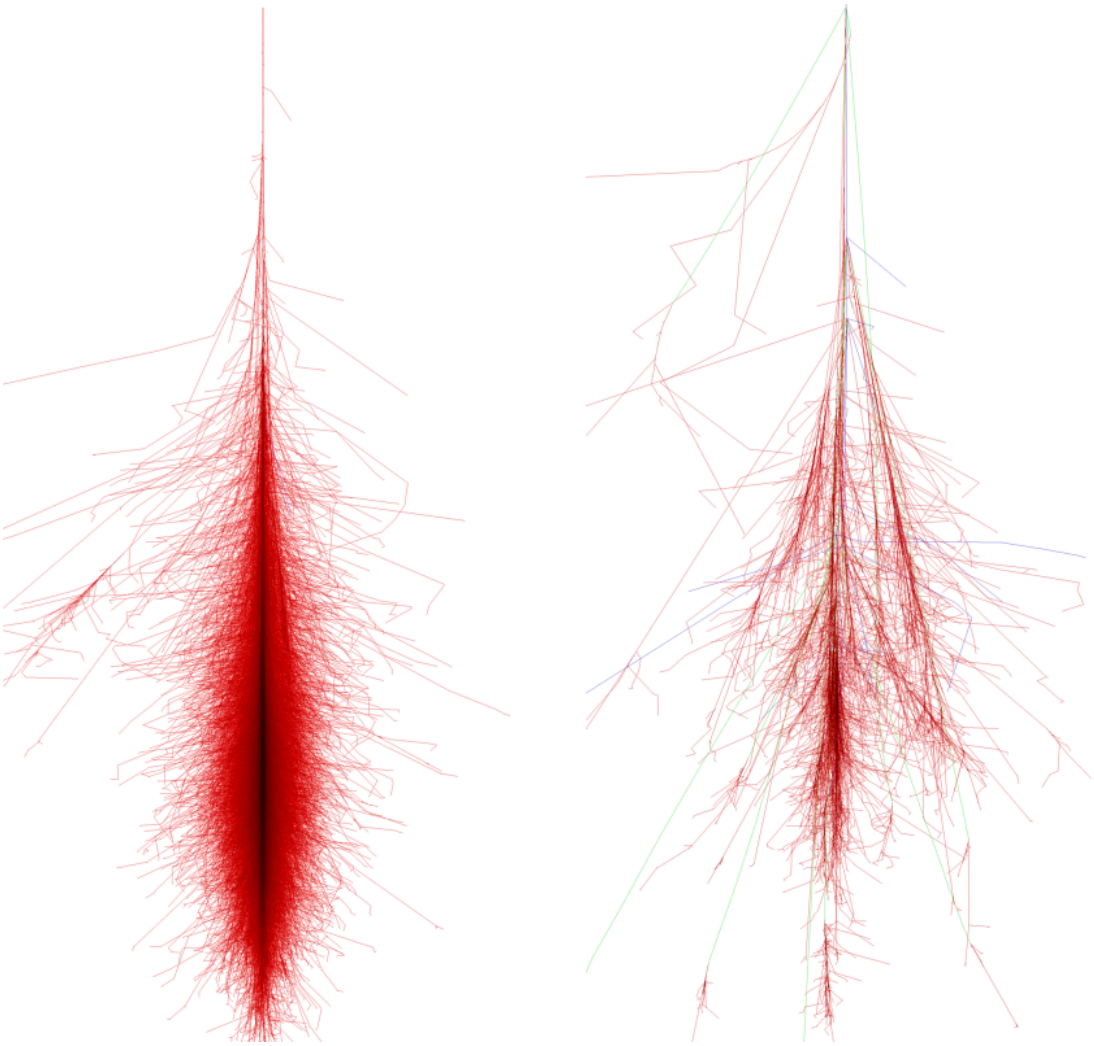

FIGURE 3.10: On the left is a gamma-ray-induced air shower and the right is a hadron-induced shower (the progenitors of both had energy of 100 GeV). In these images, red lines are electrons, positrons, and gammas, while green are muons and blue are hadrons. The color scale is logarithmic with darker colors corresponding to higher track density (images courtesy of F. Schmidt "CORSIKA Shower Images", http://www.ast.leeds.ac.uk/fs/showerimages.html).

energy resolution is about 30%-40%. At low energies, the resolution is limited by statistical fluctuations of detected photons. At high energies, it is limited by the reduced accuracy of determining the distance to the shower axis, as the Cherenkov light intensity drops as this distance increases.

3.2.2 The Whipple 10 m Telescope

The Whipple 10m IACT consists of many mirror facets (73 cm in diameter), arranged in a Davies-Cotton configuration, where the radius of curvature of the optical support structure is equal to the focal-length of the telescope (7.3 m) and one half the radius of curvature of the individual mirror facets (Davies and Cotton, 1957). This allows any light hitting an individual facet to be focused towards a central location, namely the focal point of the optical support structure. The Imaging Atmospheric Cherenkov Technique only necessitates an angular resolution on the order of a few arc-minutes, and this design meets those requirements by providing a resolution of a few tenths of a degree.

The camera (see Figure 3.12) consists of an inner camera of 2.6° diameter made of 379 13mm radius Photo-Multiplier Tubes (PMTs). Filling out the full 4.0° is an additional ring of 111 28 mm radius PMTs (Finley et al., 2001). Since the PMTs are round, overlapping light concentrators (also called light cones) are used to reduce the amount of dead space between the individual PMTs. These are machined from solid polycarbonate into truncated cones that are flame polished and aluminized by vacuum evaporation. The light cones provide an increase of 38% to the amount of

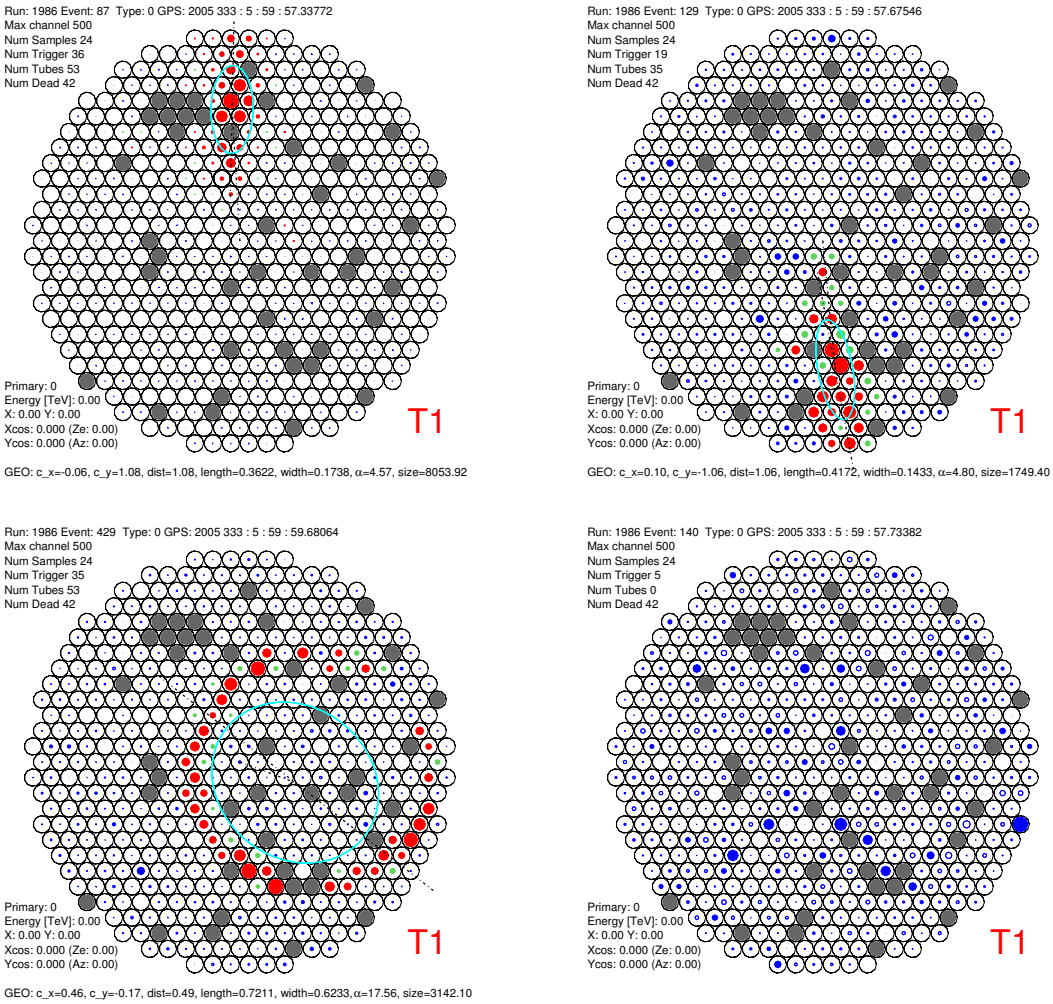

FIGURE 3.11: Camera images (from the VERITAS Telescope 1) of different types of showers. Clockwise from top left: gamma-ray induced, cosmic ray induced, muon and sky noise. Each circle is an individual PMT in the camera (grayed out pixels are not functioning). At the bottom of each image are the shower parameters for that specific shower (dist, length, width, α, and size) as computed by the analysis software.

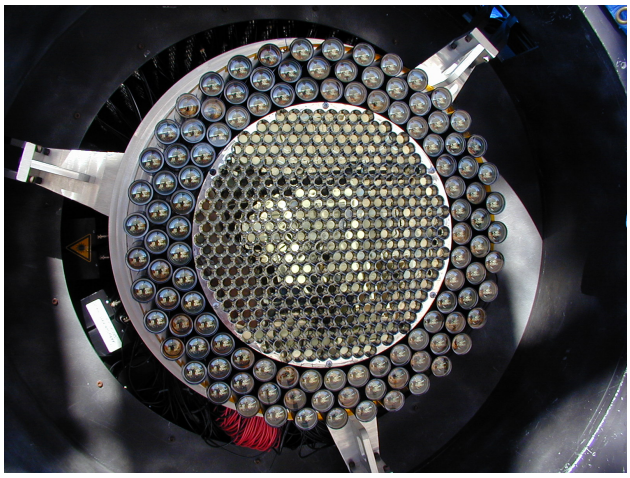

FIGURE 3.12: The 10 m Whipple IACT's 379 pixel camera, showing the focal plane and light-cones. The field of view of the center region is $\sim 2.6°$ with the total field of view including the outer ring is $4.0°$ (image from Kosack (2005)).

light collected by the camera (Finley et al., 2001). The angular size of the camera pixels ($\sim 0.2°$) matches the resolution needed to resolve a gamma-ray induced air shower.

To reduce the total data rate while keeping the signal to noise level high, the Whipple telescope operates in triggered mode only storing "shower-like" events for later off-line analysis. The trigger system consists of two separate levels: the "pixel trigger", where a constant fraction discriminator (CFD) determines whether a single pixel is triggered which is then digitized using a gated *charge analog-to-digital converter* (QADC), and the "pattern trigger", which requires that three (two and four have also been used but not in this work) adjacent pixels fire.

Chapter 4

XMM-Newton X-ray Observations of 3C 129

Some galaxy clusters are home to tailed radio galaxies and have drawn intensive theoretical and observational astrophysical study for several decades. By observing these enormous object with both Radio and X-ray instruments, one can produce high resolution images of the extended synchrotron emission from the radio galaxy that provides information on the energy density of the radio emitting plasma, magnetic field and use the X-ray data to extract maps of the temperature, chemical composition, density and pressure of the ICM. The X-ray observations allow us to infer the ICM properties and the jet propagates into a well-defined medium. Since the exact composition of the ICM is known, one can study the pressure balance between the radio-plasma and the ICM. Features such as cavities in the ICM where the plasma from the radio source has displaced the ICM would show up as deficits in the X-ray

surface brightness. Boehringer et al. (1993) observed such cavities in the Perseus cluster and Carilli et al. (1994) in Cygnus A. Recently there have been several more observations in clusters Hydra A, Abell 2597, Abell 2052 and Abell 4059 (McNamara et al., 2000, 2001; Blanton et al., 2001; Heinz et al., 2002; McNamara et al., 2005). The galaxy cluster 3C 129, named for the prototypical head-tail radio galaxy it contains, is one of the best clusters in which to observe such effects because it is one of the largest (approximately 16' long) radio jets known. Krawczynski et al. (2003) previously observed this cluster with Chandra providing some very interesting results (See Figure 4.1). Based on various radio data sets and the Chandra data they studied the balance of the pressure in the radio tail and the ICM. Using the radio observations of the radio galaxy, the pressure (and energy density) in the radio tail can be constrained. Given the observed radio (synchrotron) luminosities in several frequency bands $L_{\mathrm{s,i}}$, the magnetic field that minimizes the energy density of the radio synchrotron plasma (Pacholczyk, 1970) can be calculated:

$$B_{\mathrm{min}} = \sum_i (6\,\pi)^{2/7}\,(1+k)^{2/7}\,\phi^{-2/7}\,V^{-2/7}\,\left(\sum_i c_{12,\mathrm{i}}\;L_{\mathrm{s,i}}\right)^{2/7} \tag{4.1}$$

where k describes the contribution to the non-thermal pressure from relativistic protons, V is the emitting volume, ϕ, is the volume filling factor, and $c_{12,\mathrm{i}}$ are constants that depend on the frequency band over which the luminosity $L_{\mathrm{s,i}}$ has been measured. Thus, by looking at the radio emission from the jet, we can make estimates on the energy density of the non-thermal radio plasma and from this, compute the minimum pressure. Figure 4.2 shows the results of the pressure balance study. The tail seems

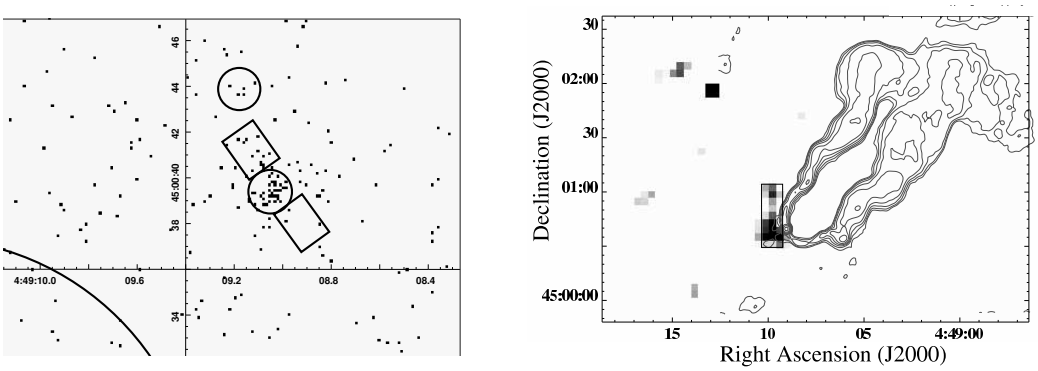

FIGURE 4.1: The Figure on the left is from Harris et al. (2002) showing the regions near the head of the radio jet in which they found emission. In addition to these highly significant features, the figure on the right shows a diffuse region in front of the jet reported by Krawczynski et al. (2003) that is marginally significant.

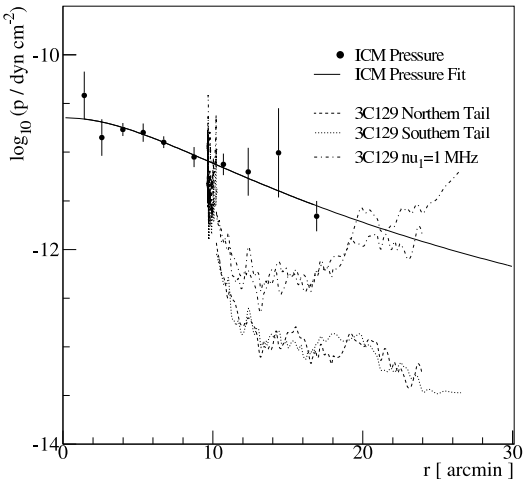

FIGURE 4.2: The thermal and non-thermal radio plasma pressures for 3C 129 as a function of distance to the core. The minimum pressure is shown as dashed and dotted lines for the northern and southern radio tails, respectively (at 330 MHz). The computed pressures are an order of magnitude below the observed pressure.

to be under-pressured by a factor of $\sim 10-40$. This pressure mismatch suggests that a major fraction of the pressure is carried by thermal or relativistic protons and/or electrons, the volume filling factor ϕ is much smaller than one, the B field is much larger than equipartition or that the radio tail does not lie in the plane of the cluster. The XMM observations (which are more sensitive to extended features than Chandra) could decide between the explanations if a cavity is discovered, meaning that the source is at the center of the cluster and $\phi = 1$.

They also showed that there is a very localized core and jet emission as well as possible diffuse emission directly in front of the jet (see Figure 4.1). For Chandra, the core and jet emission are highly significant while the diffuse emission only showed marginal significance. The diffuse emission has a greater excess than the core and jet but its extended nature makes it more difficult to detect. Since XMM has worse angular resolution than Chandra, we cannot hope to separate the emission from the core from any diffuse emission in front of the jet because, even if the diffuse emission exists, it will appear as part of the emission from the core (smeared into a single point source). If there is some type of diffuse emission we would see it as a shift in the center of gravity of the total emission and the addition of the two fluxes would be greater than that seen from either of the separate sources seen with Chandra. In the following chapter I first describe the search for cavities in the ICM of 3C 129 due to the radio plasma using a procedure of background subtraction developed by Read and Ponman (2003). Following this, I look for an excess in emission before the radio core and compare this with the Chandra results presented in Krawczynski et al. (2003). Finally, I present the results of the optical monitor data. In the following chapter, upper limits are presented at the two sigma level.

4.1 Data Sets and Analysis

The data consists of one pointing on February 18, 2003, with the MOS-1 and MOS-2 chips along with the PN detector for a 50 ksec exposure proposed by H. Krawczynski

et. al. in 2001. See Appendix A for more details on the observation. The analysis uses the standard XMM-Newton Science Analysis System (XMM-SAS) software version 6.5.0.[1] To begin, I reprocessed the data using the standard processing pipeline (emproc) with the most recent calibration data. This generates a single event file for each detector (MOS 1, MOS 2, and PN, see Section 3.1.2 for details on these detectors).

The event files were then filtered for major background flares as well as standard filters applied to remove bad events due to pile up and faulty pixels. Following this, the event file was divided into seven different energy bins (Table 4.1), the first six standard XMM energy bins while the last (bin 6) chosen to fit the energy range in which the MOS detectors are most sensitive (see Figure 3.3). Figure 4.3 shows the results of the filtering and binning for the six basic energy bins. These images have been smoothed and are a mosaic of the two MOS images. The non-background subtracted images were used for spectral analysis. The left image in Figure 4.4 shows the optimal bin that was used for profile analysis. Considering Figure 4.3, one notices that the two middle bins (2 and 3) are the cleanest in terms of cluster detail and statistics. This information, along with the quantum efficiency curve (Figure 3.3), influenced the choice of energy bin 6.

Following this, background subtraction was performed following the procedure and data sets found in Read and Ponman (2003). The background files were constructed from a superposition of 72 pointed observations with the point sources removed and

[1] http://xmm.vilspa.esa.es/sas/

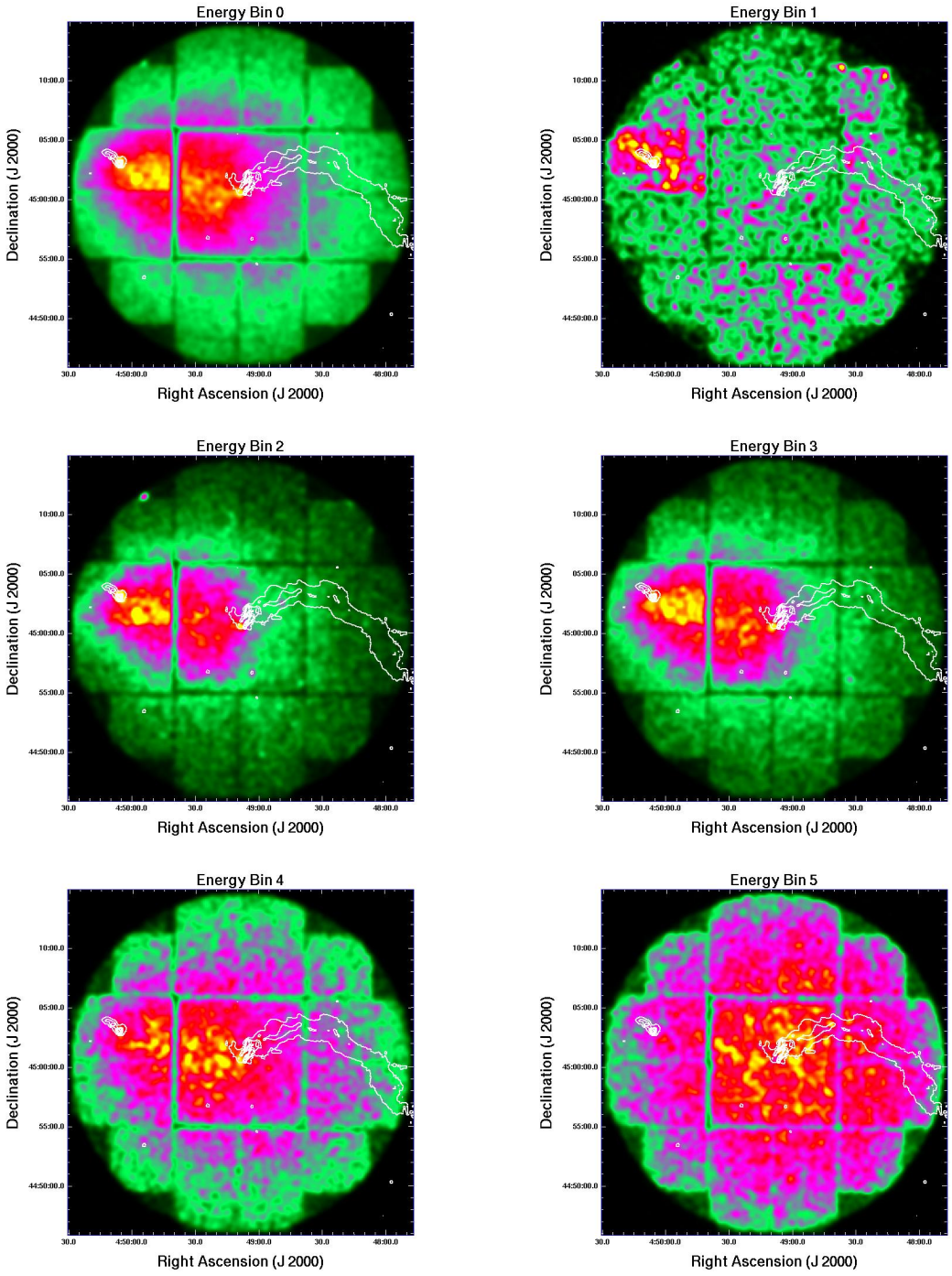

FIGURE 4.3: Adaptively smoothed XMM X-ray image of 3C 129 after all processing and filtering (but before background subtraction). The cluster center is to the left of the image while the head of the radio galaxy is at the center of the image. The image has been divided into six standard energy bins. Overlaid in white are the radio contours described in Figure 4.5.

TABLE 4.1: The energy bins used in this analysis. Bin 0 is the full range which is subsequently used for spectral analysis. Bins 0-5 are the standard XMM bins while bin 6 is a bin chosen to best represent the capabilities of the MOS instrument.

Bin Number	Energy Range (keV)
0	0.2 - 12
1	0.2 - 0.5
2	0.5 - 2
3	2 - 4.5
4	4.5 - 7.5
5	7.5 - 12
6	0.7 - 4.5

are specific to an instrument and filter. These background files were "skycasted" to match the sky coordinates of the 3C 129 observation. The event files were divided into small energy bins of 100 eV before background subtraction and then rebuilt to form the large energy bins afterwords. This was done to counteract an over-correcting for exposure that can still be seen in the lowest energy bin (bin 1) and the two highest bins (4 and 5), even with this correction. Thus, the final choice of energy bin used in the extended analysis is bin 6, which can be seen as the energy range that is least affected by this.

The subtraction process begins with an image created from the original (100 keV wide) energy file. A background file and particle image is created from the blank-sky background and a closed event file. The out of field of view events are used to scale these images to correct any discrepancies in observation time. An exposure map and exposure mask are also created (the exposure depends on the energy range desired and this is where the small 100 keV energy bands are desirable: the exposure creation uses

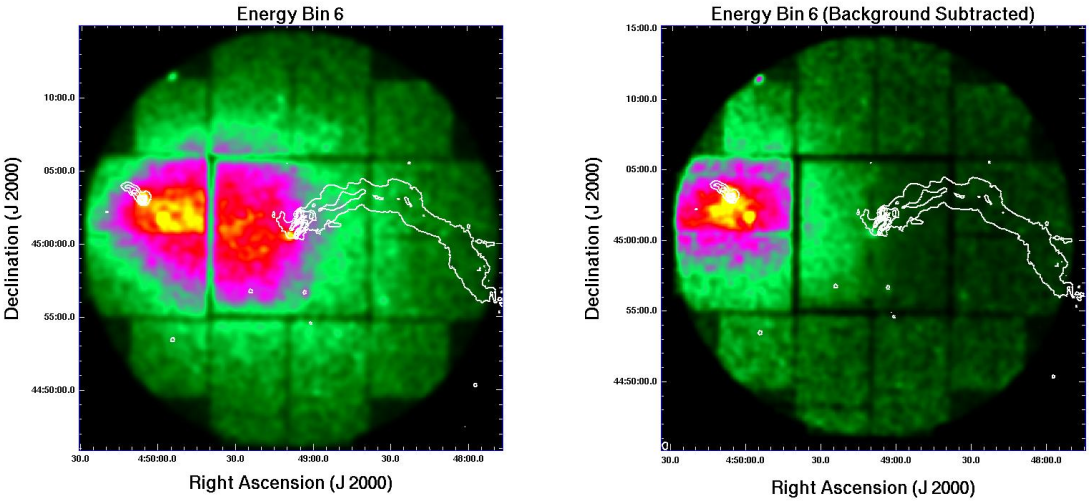

FIGURE 4.4: The image on the left is energy range 6 before background subtraction and the image on the right is after background subtraction. Both images have been smoothed with a gaussian of width 3.3″. Overlaid in white are the radio contours described in Figure 4.5. The lines seen in these figures are from the chip boundaries in the detector.

the average of the energy range to determine the exposure map and if large energy bins are used, there is a large error introduced in the exposure map creation). From here, background exposure corrected masked images are created. Figure 4.4 shows the observation after the background subtraction for the optimal bin.

Figure 4.4 illustrates the extent of the cluster ICM. The radio tail emanates from the center of the image (but not the center of the cluster) at the radio galaxy 3C 129 towards the west of the image. The center of the cluster is located to the east of 3C 129 at the location of the radio source 3C 129.1. There are three distinct X-ray sources, 3C 129, 3C 129.1 and 3C 129.1SW (located to the southwest of the cluster center). Note that the lines seen in the image are due to chip boundaries in the XMM detectors.

Some of the features seen in the X-ray image have only modest statistical significance. To determine the statistical significance of any excess seen at a point in the FoV, I use the number of counts in the ON region, N_{ON}, and compare this to the number of counts found in a reasonable comparison OFF region, N_{OFF}. I compute the statistical significance based on Poisson probability distribution that accounts for the statistical uncertainty in both the source and comparison region following the method of Li and Ma (1983). The statistical significance of an excess is given in standard deviations by:

$$S(N_{\rm ON}, N_{\rm OFF}; \xi) \; = \; \sqrt{-2 \, \ln(\lambda)} \tag{4.2}$$

where

$$\lambda \; = \; \left[\frac{\xi}{\xi + 1} \left(\frac{N_{\rm ON} + N_{\rm OFF}}{N_{\rm ON}} \right) \right]^{N_{\rm ON}} \times \left[\frac{1}{\xi + 1} \left(\frac{N_{\rm ON} + N_{\rm OFF}}{N_{\rm OFF}} \right) \right]^{N_{\rm OFF}} \tag{4.3}$$

and ξ given by:

$$\xi \; = \; \frac{\int_{\Delta\Omega_{\rm ON}} A(\Omega) \, d\Omega}{\int_{\Delta\Omega_{\rm OFF}} A(\Omega) \, d\Omega} \tag{4.4}$$

where $\Delta\Omega_{\rm ON}$ and $\Delta\Omega_{\rm OFF}$ are the solid angle areas of the source and background regions, respectively, and $A(\Omega)$ is the the effective area of the detector. I use the exposure map produced for the optimal energy range as $A(\Omega)$ and integrate over this map with the CIAO[2] tool `dmstat`. Although the method is based on Poisson probability distributions, the expression for the statistical significance is only valid for $N_{\rm ON} > 10$ and $N_{\rm OFF} > 10$ (Alexandreas et al., 1993).

[2] Chandra Interactive Analysis of Observations, http://cxc.harvard.edu/ciao/

4.2 Radio Tail Results

The X-ray emission near 3C 129 is shown in Figures 4.5 and 4.6 along with the radio contours. I searched for deficits in the ICM surface brightness along the radio tails of the galaxy 3C 129. Figure 4.5 shows a zoomed in picture of the X-ray flux from the cluster overlaid with a low resolution radio contours. This jet is over 17' long with a width of between 13′, making it one of the largest of its kind. Figure 4.6 shows a high resolution radio contour image of the head of the jet detailing this highly complicated region. The radio contours used here were all obtained using the Very Large Array (VLA)[3] and have been previously reported by Krawczynski et al. (2003) in an analysis of this cluster with the Chandra observatory. The low resolution contours are at a frequency of 1400 MHz while the high resolution images of the head of the radio jet are at 5 GHz. Additionally, a high resolution 8 GHz map of 3C 129.1 has been used. Figure 4.7 is a profile of the X-ray flux along the line of the jet. The first two bins cover the high resolution radio jets seen in Figure 4.6 and there is no significant change in this region. There is a large decrease in flux showing some type of change in the jet as it moves from the 5 GHz radio region and into the 1.4 GHz region.

To search for deficits, I first optimized a search bin size for both the high resolution and low resolution areas. For a rectangular jet of width 2′ and length $\sim 17'$, I get an optimal bin size of 3.33′, or slightly larger than the width of the jet. For a smaller

[3] The National Radio Astronomy Observatory is a facility of the National Science Foundation operated under cooperative agreement by Associated Universities, Inc.

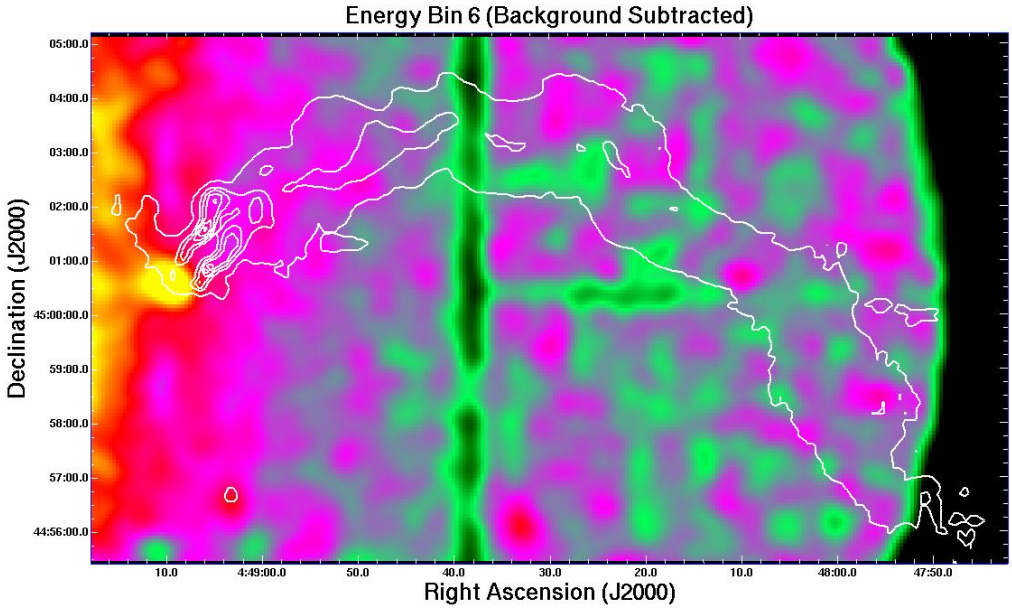

FIGURE 4.5: The colors (scaled linearly) show the background subtracted flat fielded XMM 0.7 - 4.5 keV data (MOS 1 and MOS 2) smoothed with a Gaussian of width 5″. The 1400 MHz radio contours detail the radio tail spanning over 17′ in length and 3′ at its largest width. The contours are drawn at 0.0025, 0.035, 0.08, 0.12, 0.15, and 0.20 beam^{-1} with a beam-width of 8″ FWHM.

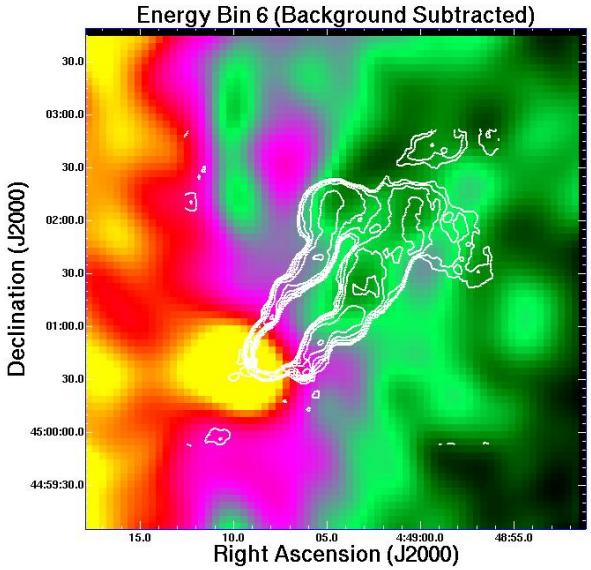

FIGURE 4.6: The colors (scaled linearly) show the background subtracted flat fielded XMM 0.7 - 4.5 keV data (MOS1 and MOS 2) smoothed with a gaussian of width 5". The radio contours are from 5 GHz VLA data with a 1.8" FWHM beam-width and a logarithmically spaced from 1 to 32 mJy beam^{-1}.

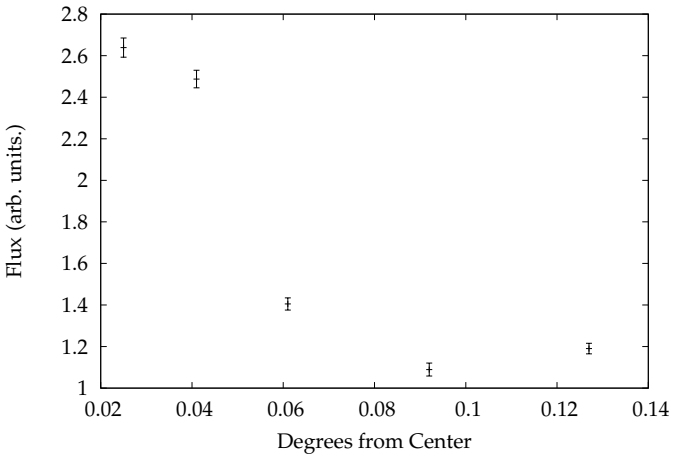

FIGURE 4.7: X-ray flux profile along the jet showing a sharp decrease at the end of the high resolution part of the jet. The first two bins cover the high resolution radio jets seen in Figure 4.6 and there is no significant change in this region. There is a large decrease in flux showing some type of change in the jet as it moves from the 5 GHz radio region and into the 1.4 GHz region.

rectangular jet of width 16″ and length 200″, the optimal bin size is almost as large as the jet, or 2.8′. This search incorporates the FWHM of the optics (approximately 15″), which smears any features of the small jet to an almost imperceptibility, making it optimal to search over the whole region with one large bin. The results of a search for any deficit (calculated as a percent change) is shown in Table 4.2, using one bin for the high resolution jet and 4 bins covering the low resolution image. I also computed a total upper limit for the whole radio tail. The total upper limit on the percent change along the 5 GHz radio tail is 6.0% and for the full tail it is 1.5%. Table 4.2 shows neither evidence for a significant deficit or excess.

I computed the maximum expected deficit due to a radio tail replacing the ICM modeled by a king profile which takes the following form:

$$\Sigma(r) = \frac{\Sigma_0}{[1 + (r/r_c)^2]^{3\beta - \frac{1}{2}}} \tag{4.5}$$

I modeled the King profile using the fit found in Krawczynski et al. (2003), which gives $r_c = 7.3'$ and $\beta = 0.68$. I integrated the King profile for slices along the tail (for

TABLE 4.2: Upper limits on the fractional X-ray flux deficits for each bin. The jet shown by the high resolution radio contours was covered by a single bin while the low resolution jet with 4. The total of the 4 bins is also reported. Note that a negative change means that there is a deficit in the radio jet compared to the background region.

Jet	Bin	% Change	Statistical Error	Fractional Deficit Upper Limits
5 GHz VLA	0	1.6	3.1	6.0
1.4 GHz VLA	0	4.8	1.8	1.9
1.4 GHz VLA	1	3.5	2.3	3.4
1.4 GHz VLA	2	1.6	2.1	3.8
1.4 GHz VLA	3	-3.8	2.1	8.1
1.4 GHz VLA	total	1.5	1.0	1.5

distances of 10′, 12′, 14′, and 16′ from the cluster core). Table 4.3 shows the results of this calculation. The average change is 10%, which represents the maximum expected change and our actual upper limits are all below this. This shows that the deficit is smaller than expected. We can tentatively conclude that the radio tail does not only consist of non-thermal plasma, but that it is mixed with the thermal ICM along the tail. If the tail, however, does not lie in the central plane of the cluster (which is an assumption of the above calculation), then the expected deficit may be small even if it fully consists of non-thermal plasma.

4.3 Spectra

There are three regions of interest for spectral analysis, the two hot spots at the core of the cluster and the head of the radio jet. In the following section I will report on the spectral fitting of these three regions. I used the XMM full images from 0.2

TABLE 4.3: Estimates of the expected X-ray emission deficit due to the radio jet propagating through the ICM. *Distance* is the perpendicular distance from the cluster core and *Width* is the width of the jet at that distance.

Distance	Width	Expected Deficit [%]
12'	1.2'	5.3
14'	2.5'	11
16'	2.0'	7.7
18'	2.0'	7.5
20'	2.8'	13

keV to 12 keV, ignoring all of the event outside this usable range. The XMM-SAS tool xmmselect was used to generate the spectral products needed for the analysis. This involved selecting a circular source region along with an annulus around this region to use as background. This tool calls the source region optimization task as well as the meta task especget which generates all of the files needed for XSPEC. I used the power law model with XSPEC to fit to the data from the three regions. The results of the search can be found in Table 4.4. The fits for the two sources within the cluster center, 3C 129.1 and 3C 129.1SW, were computed with all parameters free. I used the nH value found in Krawczynski et al. (2003) for the fit to the source at the head of the radio jet (3C 129) to allow for a comparison with the Chandra data. This shows that the final flux for the XMM region (which includes the point source plus the possible extended emission) is 62% greater than that of the Chandra point source, suggesting that there is some type of extended feature around the head of the radio jet. Harris et al. (2002) and Krawczynski et al. (2003) reported 46 counts from the core of 3C 129 and 131 on source counts from the region in front of the jet. If

TABLE 4.4: 3C 129 spectral results. If the error is exactly 0.00 then that specific quantity was fixed for that fit. The fit to the Chandra data is poor due to low statistics and and fixing two of the parameters.

Source	nH (10^{22})	Index	norm (10^{-5})	χ^2	Null
3C 129.1	1.5 ± 1.1	5.1 ± 3.0	36 ± 170	0.85	0.85
3C 129.1SW	1.0 ± 0.31	3.9 ± 0.87	25 ± 35	0.99	0.51
3C 129 (XMM)	0.82 ± 0.00	2.33 ± 0.52	1.9 ± 1.3	1.07	0.32
3C 129 (Chandra)	0.82 ± 0.00	2.33 ± 0.00	1.17 ± 1.00	0.050	1.00

the excess from the region in front of the jet would have been real, the XMM flux (which includes the core and jet emission plus the extended feature, see Figure 4.1) should have exceeded the Chandra flux by a factor of 3.85. Here we observe only an excess by 62%. Unfortunatly, we cannot say with XMM where the 62% excess flux originates.

4.4 Optical Monitor Analysis and Results

As mentioned in Chapter 3, the XMM-Newton satellite includes an optical monitor. In this section I present the results obtained with the standard analysis chain using this instrument. There were several exposures taken with the optical monitor (see Appendix A for a summary of the exposures). The images presented here are full frame and user frame image mosaics of the different exposures. These images are the standard pipeline processed results. Figure 4.8 shows a full frame image (the central $17' \times 17'$ of the field of view of the X-ray telescope) taken with the V filter in place (510 - 580 nm). Overlaid are the low resolution radio contours. The large doughnut

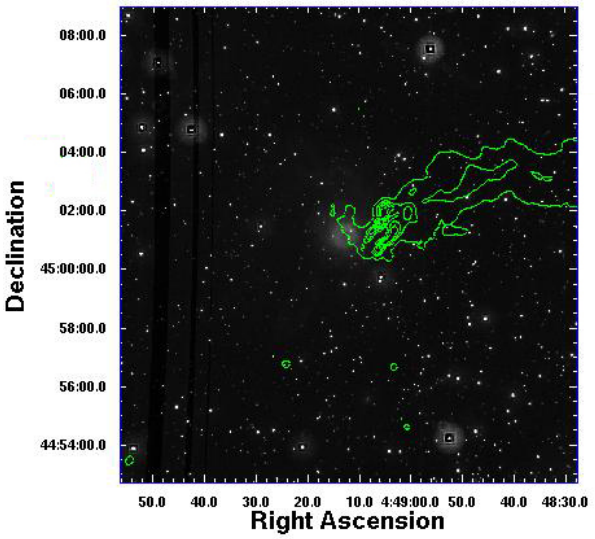

FIGURE 4.8: Full frame optical image of 3C 129 taken with the V filter in place (510 - 580 nm). The low resolution radio contours are shown in green. Coordinates are given in J2000. The large doughnut shaped feature near the head of the radio jet is an artifact of the detector and is not seen in the digital sky survey instrument (Figure 4.9).

feature north of the radio jet is an artifact of the instrument which is not seen in the digital sky survey (DSS) image (Figure 4.9). Figure 4.9 also shows a user window image along with the high resolution head of the radio tail. This image was taken with the B filter in place (380 - 490 nm). Both the DSS image and the XMM image clearly show the faint elliptical host galaxy of the radio source 3C 129. I conclude that the XMM optical image does not improve over the archival DSS image.

4.5 Discussion

The XMM observations of the radio galaxy 3C 129, in the galaxy cluster 3C 129, show evidence for emission at the head of the radio jet as well as in the core of the radio galaxy 3C 129.1. This emission fits to a power law which would indicate that the emission originates as non-thermal emission from the jet or a as a superposition of thermal accretion disc emission at different temperatures. I did not find a deficit

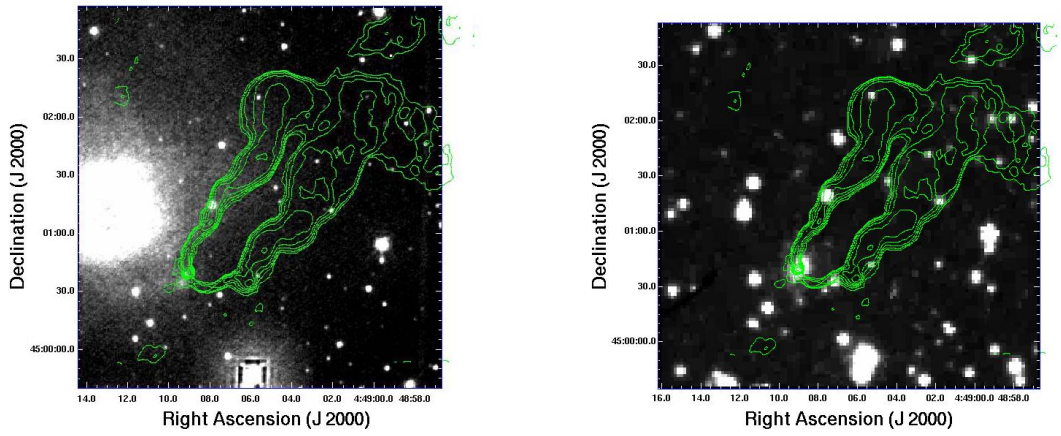

FIGURE 4.9: On the left is a zoomed in optical image of 3C 129 taken with the B filter in place (390 - 490 nm). On the right is an archival digital sky survey image of the same region clearly showing the faint elliptical host galaxy as well as confirming the large doughnut region in the XMM images is an artifact of the instrument. The high resolution VLA contours are shown in green. Coordinates are given in J2000.

in the ICM emissivity associated with the the radio tail which would indicate that the tail replaced ICM. Here I computed upper limits on the fractional deficit and find that it is 6% for the portion nearest the head and 1.5% for the full radio tail although segments of the tail have upper limits as high as 8%. Further analysis, based on spectral fitting of the core, shows that there is 62% more emission in the XMM data than in the Chandra observation, suggesting that there is some extended emission in addition to the core and jet emission seen by Chandra. The optical monitor shows the existence of a faint elliptical galaxy hosting the head of the radio jet.

Chapter 5

TeV Observations of the Perseus and A2029 Clusters with the Whipple 10 m Telescope

5.1 Data and Analysis

The following chapter describes a search for TeV emission from the Perseus and Abell 2029 galaxy clusters using the Whipple 10 m Cherenkov telescope (see Chapter 3). The chapter is organized as follows: I describe the observations, data cleaning procedures, and the data analysis methods in Section 5.1. The main results of this study are a search for point source emission from localized sources in the clusters and a search for diffuse emission from the ICM. I present these results in Section 5.2 and discuss them in Section 5.3. Reported uncertainties are one standard deviation and

upper limits are given at the 90% confidence level, unless otherwise stated.

There are limitations to observing extended sources with a single Cherenkov telescope like the Whipple 10 m. First, the sensitivity of the telescope falls for angular distances greater than 0.8 degrees from the center of the field of view. Churazov et al. (2003) shows a high temperature region in the Perseus cluster, at about 0.25 degrees from the cluster center, that might be associated with shocks and possibly emit VHE emission. Even though we theoretically could study such shocks, we do not perform a specialized search for merger related emission. In the case of the more distant cluster A2029, our search region of 0.8 degree radius covers a physical region of 4.2 Mpc radius. Thus, our search includes all the cluster emission, independent of where in the cluster it originates.

5.1.1 Instrumentation and Data Sets

We observed the Perseus cluster between August 16, 2004, and February 5, 2005 (UT). Data were taken as pairs of 28 minute runs. An ON run pointed at the source was followed by an OFF run at the same azimuth and elevation but offset 7.50° (30 minutes) in right ascension for background subtraction. Even though care was taken to observe during the clearest of nights, some runs had low rates and were removed. There were also situations in which the sky conditions differed between the ON/OFF pairs, and these were also removed, resulting in a total of 29 ON/OFF pairs for analysis. Performing the same selection on the Abell 2029, observations (observed between March 7, 2003, and May 5, 2003 (UT)) resulted in 14 ON/OFF pairs. In

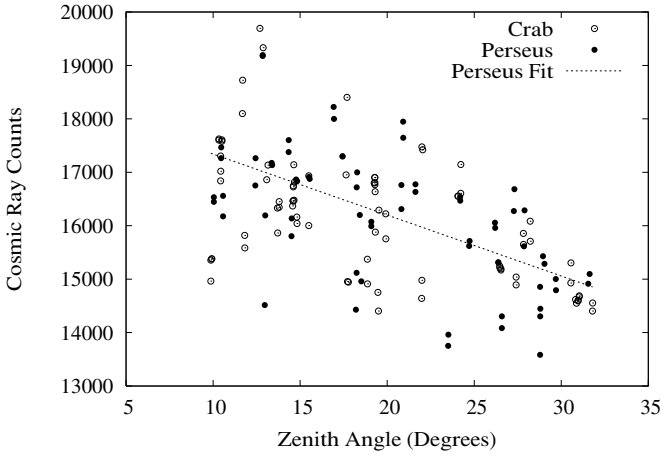

FIGURE 5.1: Cosmic Ray counts on a run by run basis versus zenith angle. Shown are data from the Crab Nebula (open circles) and the Perseus Cluster (closed circles). We fitted each group of data (see the Perseus Fit line for an example) to show the dependence of the rate on the zenith angle and rejected any runs that deviated by more than 10%.

TABLE 5.1: Description of the various data sets used in this analysis. The Crab sets titled "Crab-0.5" and "Crab-0.8" are observations performed with the telescope offset from the location of the Crab nebula by 0.5° and 0.8°, respectively.

Source	Season (MJD)	Number (Pairs)	ON (min)	OFF (min)
Perseus	2004-2005	29	810.4	810.4
Abell 2029	2003-2004	13	363.3	363.3
Crab	2003-2004	29	810.4	810.4
Crab	2004-2005	24	670.7	670.4
Crab-0.5	2003-2005	6	167.7	167.6
Crab-0.8	2003-2005	8	223.6	223.6

addition to the cluster observations, a number of observations of the Crab Nebula (a "Standard Candle" in TeV gamma-ray astronomy) were taken to determine the detection efficiency and angular resolution for various points on the camera. The cosmic ray rates of each run versus the zenith angle are shown in Figure 5.1 to illustrate how the pair selection is done (by rejecting those runs that deviate more than 10% from the expected rate). Table 5.1 details the duration and observing season of the various data sets and Appendix B thoroughly lists the details for each run.

5.1.2 Standard Analysis

After determining which runs to include, the data were analyzed using the standard 2^{nd}-moment-parametrization technique (Hillas, 1985). We identify gamma-ray events and suppress background cosmic ray events by applying gamma-ray selection criteria (EZCuts2004, see (Kosack, 2005)), designed to be independent of zenith angle and energy and well suited for the analysis of extended sources. The 2D arrival direction of each gamma-ray event was calculated from the orientation and elongation of the Cherenkov light distribution in the camera (Buckley et al., 1998). We estimate that the mean energy threshold for the Whipple 10 m to be approximately 400 GeV (Finley et al., 2001). More detailed descriptions of Whipple observing modes and analysis procedures have been given by (Weekes, 1996), (Punch and Fegan, 1991), and (Reynolds et al., 1993).

5.1.3 Cluster Specific Analysis

In this section we describe the specific analysis techniques applied to the clusters, including the method used to search for point sources within each cluster. Based on the expected lateral emission profiles, we then discuss the examination of the cluster for diffuse emission.

The initial analysis of the clusters involves a search for point sources before the analysis of any extended emission. It is a result in itself if point sources exist but then they must be excluded from the extended emission analysis. The atmospheric

Cherenkov technique was originally designed for the observation of point sources at the center of the field-of-view. Thus, the resolution and detection efficiency is not optimal off center but to search for point sources at any point in the field of view, we need to determine better these factors at all camera locations. Using data from the Crab Nebula that were taken during the same time frame as the cluster observations, we used an empirical method to determine the telescope properties. The background-subtracted Crab data were binned by the square of the distance of the reconstructed shower direction from the location of the Crab Nebula (so as to eliminate any solid angle dependence) and fitted with an exponential. These fits gave us a direct measurement of the angular resolution of the camera for a point source at different locations within the field-of-view. From these same data, we determined an optimal angular cut based on the integral number of excess and background counts as a function of angular distance from the source location. By calculating the gamma-ray rate at the different offsets, we also determined how the efficiency of the camera falls off towards the edges.

This empirical method was compared to Monte Carlo simulations of centered and offset data. The Monte Carlo code[1] simulates atmospheric Cherenkov showers and calculates the response of the Whipple detector. The simulated data have the same format as the experimental data and were analyzed using the same methods as those applied to the real data. We produced a simulated shower set with a differential spectral index of -2.5 and fed this through the detector simulations for different source

[1] http://www.physics.utah.edu/gammaray/GrISU/

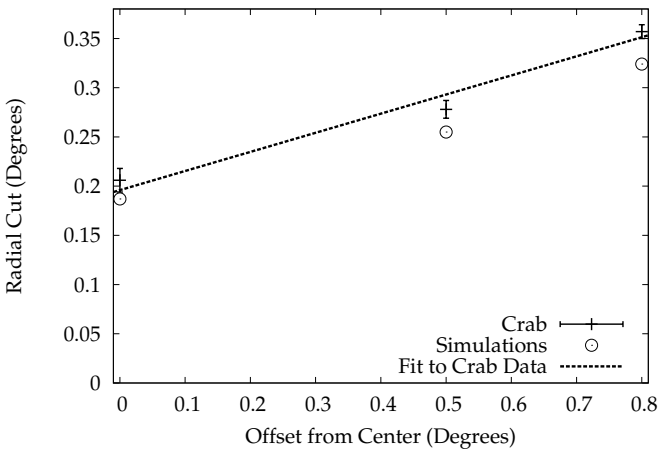

FIGURE 5.2: Optimal angular cut for different source locations on the camera. All the cuts accept $\sim$ 50% of all the triggered Crab events. Shown are the results from the Crab observations in 2004 (crosses) and from Monte Carlo simulations (circles). The cut increases further from the center due to the loss in resolution. The fit to the Crab data (dashed line) was used to search for point sources in the field-of-view.

offsets and compared this with observations. Figure 5.2 shows the optimal angular cut at the three different offsets. The optimal cut was used to determine the total number of events originating from a specific point in the field-of-view. This cut increases from 0.2° at the camera center to 0.35° at a 0.8° source offset due to the poorer angular resolution towards the camera edge. Figure 5.3 shows the normalized gamma-ray rate for the source located at the various offsets using the cut from Figure 5.2. Compared to the center of the field-of-view, the rate decreases by 40% at 0.8° from the center due to the loss in detection efficiency. The simulated data rates and optimized cuts agree well with the experimental results. Since the efficiency of the detector falls off above a radius of 0.8°, we only use the central 1.6° diameter region. If TeV emission mimics the thermal surface brightness, we would see almost all of the emission expected. Unfortunately, our search has only very limited sensitivity beyond the central 0.8° from the center of the field of view.

Once the camera properties were determined, we performed a search over the

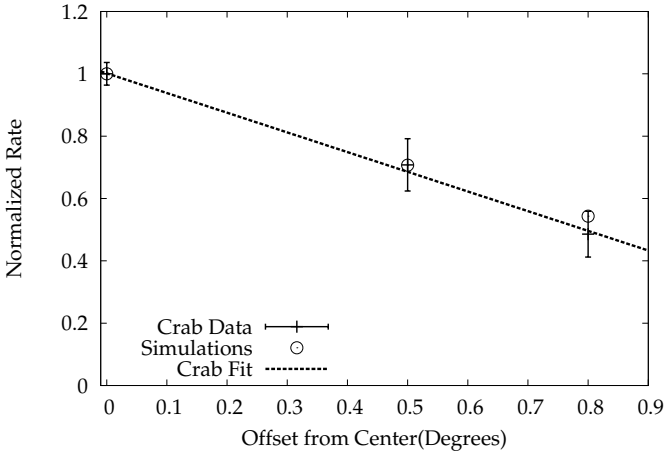

FIGURE 5.3: Crab gamma-ray rate normalized to 1.0 at zero offset (crosses) versus offset from the center of the camera using the optimized cut found in Figure 5.2. The fit to these data (dashed line) was used to calculate the upper limit for point sources within the field-of-view. Also shown are the results from Monte Carlo simulations (circles) that match the observational data very well. At the center of the field-of-view, the detection rate is 1.9 events per minute.

central 0.8° radius region of the field-of-view of the camera for point sources within the clusters. We applied the optimal cut determined above at every point in the field-of-view and calculated the excess or deficit of candidate gamma rays from the data. This excess or deficit was then normalized to the actual Crab rates from the same observing season to compute an absolute flux. This was then used to calculate a Bayesian upper limit on the flux (Helene, 1983), taking into account the statistical error for the Crab event rate.

The search for extended emission is not as straight forward as the point source search. We must assume an expected emission profile before we can determine if such a profile exists. In this case, we assume that the TeV gamma-ray surface brightness mimics that of the thermal X-ray emission seen by Chandra (Sanders et al., 2005) and BeppoSAX (Nevalainen et al., 2004), which arises from interactions of the thermal protons in the cluster. The X-ray surface brightness can be modeled as a double-β

TABLE 5.2: Values of the double-β model parameters for the Perseus cluster of galaxies from (Pfrommer and Enßlin, 2004) and based on data from (Churazov et al., 2003) and (Struble and Rood, 1999). The values shown for Abell 2029 are for a King profile based on data from (Jones and Forman, 1984).

Cluster	a_1	a_2	r_1 (kpc)	r_2 (kpc)	β_1	β_2
Perseus	1.0	0.104	57	200	1.2	0.58
Abell 2029	1.0	N/A	212	N/A	0.83	N/A

profile:

$$\Sigma(r) \propto \left(\sum_{i=1}^{2} a_i (1 + \frac{r^2}{r_i^2})^{-3\beta_i/2} \right)^2 \tag{5.1}$$

where $\Sigma(r)$ is the surface brightness and a_i, r_i and β_i are isobaric model parameters (Pfrommer and Enßlin, 2004). The values of these parameters, based on results from (Churazov et al., 2003) and (Struble and Rood, 1999), can be found in Table 5.2. The emission will continue out to the accretion shock which is expected to occur at $\sim$2.2° from the cluster center. Assuming the double-β profile, we estimate that our angular cut of 0.3° from the cluster center optimizes the sensitivity of the search for cluster emission. A fraction of 95% of the total cluster emission comes from within 0.3° from the cluster. Figure 5.4 shows the ON and OFF data after analysis and cleaning plotted versus the distance from the center of the field-of-view squared. There is an excellent match between the ON and OFF data and no obvious excess out to the edge of the field-of-view.

Abell 2029 could almost be treated as a point source but there is some extension to the cluster and in this case the X-ray surface brightness is better modeled in the

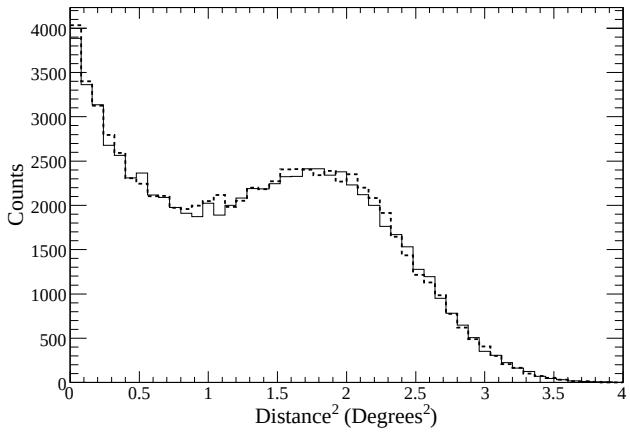

FIGURE 5.4: Number of Whipple 10 m Perseus observation events versus the distance of the estimated arrival direction from the center of the field-of-view squared. The dashed line shows the OFF counts and the solid line the ON counts. There is a good match between the ON and the OFF data out to the edge of the camera, and no excess from the cluster is detected.

case of Abell 2029 by a single-β King profile (King, 1972) given by

$$\Sigma(r) \propto a_i(1 + \frac{r^2}{r_1^2})^{-3\beta_1+1/2}. \tag{5.2}$$

The model parameters are found in Table 5.2 and are from (Jones and Forman, 1984), based upon observations made with the Einstein observatory. We chose the Einstein observations over more recent observations by Chandra due to the larger field-of-view of Einstein. For this cluster, the X-ray emission continues out to $\sim$1.0° from the center of the cluster, and 96% of the emission comes from the central 0.3°.

We then determined quantitative upper limits by normalizing these profiles over the field-of-view of the camera. This was then convolved with the point spread function of the Whipple telescope (which widens the profile even more) and multiplied by the offset-dependent Crab detection rate. The method generates a map of the expected detection rate, assuming that the entire cluster produces the same TeV flux as the Crab Nebula (using this we can determine a flux normalized to the Crab for the full cluster). Figure 5.5 shows the expected emission based on the double-β profile for

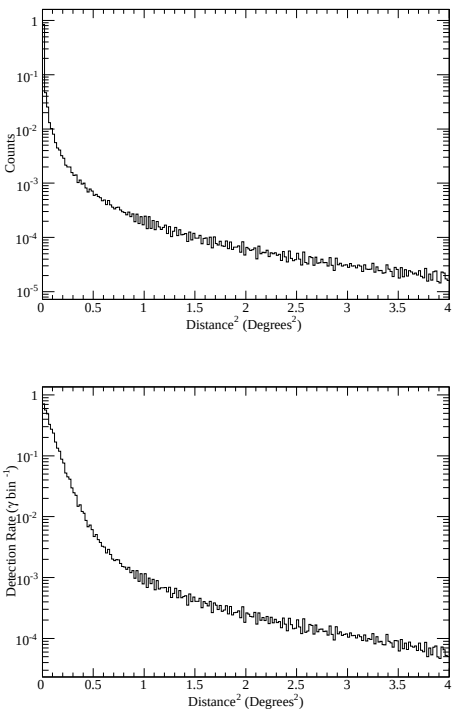

FIGURE 5.5: The upper figure shows the expected count distribution for the Whipple telescope based upon the double-β profile for the Perseus cluster (Equation 5.1) normalized so that the area under the curve is 1.0. The lower figure is this count distribution convolved with the angular resolution and the Crab detection rate of the Whipple 10 m telescope. The lower plot can be integrated to give the total expected signal from the Perseus cluster if it shines with the flux of the Crab Nebula. A fact to note is that almost all the expected emission arises from within 0.3° of the cluster core.

the Perseus cluster at various stages in the analysis process. We then took the actual observed data to determine the integral excess over the inner 0.3° and compared this number with the expected integral emission for the same region. We then determined an upper limit on the diffuse TeV flux in units of the Crab flux. We also computed upper limits by integrating counts over the most sensitive 0.8° region of the camera.

5.2 Results

There is no excess detected in the field-of-view for the Perseus cluster (see Figure 5.4). We compute a significance of -2.1 standard deviations and an upper limit on the diffuse emission of 13% of the Crab flux (7.4×10^{-12} ergs cm^{-2} s^{-1}) using a radial cut of 0.3°. Figure 5.6 is a map of upper limits on the point source emission showing

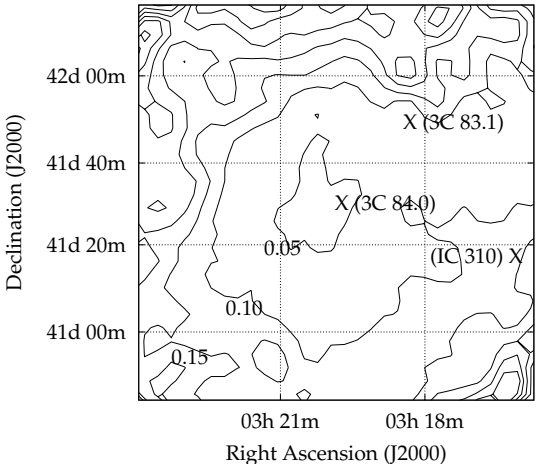

FIGURE 5.6: Gamma-ray flux upper limit map (90% confidence level) from point sources of the inner 1 degree of the Perseus cluster of galaxies. The scale is in units of the flux from Crab Nebula with each contour step equal to 0.05 times the Crab flux. The approximate location of the radio sources found in Table 5.3 are shown.

that all of the upper limits are below 0.45 Crab, and most (80%) are below 0.05 Crab. We specifically computed the upper limits at the locations of the three radio galaxies associated with spectroscopically identified cluster galaxies (Table 5.3). The upper limit on the TeV emission from the central galaxy, NGC 1275, is 4.0% of the Crab flux (2.7×10^{-12} ergs cm^{-2} s^{-1}).

Abell 2029 does not show any evidence for point source or extended emission. Figure 5.7 shows a map of upper limits on the point source emission. All of the upper limits are below 1.1 Crab with the majority (80%) below 0.1 Crab. Table 5.3 lists an upper limit of 13% of the Crab flux (14×10^{-12} ergs cm^{-2} s^{-1}) for the central radio galaxy. Within 0.3° from the camera center, we find a deficit of 13 counts with a statistical significance of -0.15 standard deviations. Assuming the emission profile of Abell 2029 follows Equation (5.2), we compute an upper limit on the diffuse emission of 14% of the Crab flux (16×10^{-12} ergs cm^{-2} s^{-1}) . Table 5.4 gives a summary of the various upper limits for each cluster. All upper limits discussed in this chapter have been computed for the gamma-ray emission from within 0.2°, 0.3°, and 0.8° angular

	Perseus			Abell 2029
Source	3C 84.0 (NGC 1275)	3C 83.1 (NGC 1265)	IC 310	IC 11
RA (J2000)	03 19 48	03 18 16	03 16 43	15 10 56
DEC (J2000)	+41 30 42	+41 51 27	+41 19 29	+05 44 42
20 cm Flux (mJy)	2829.2	1305.5	168.1	527.8
400 GeV Upper Limit (Crab)	0.047	0.086	0.13	0.13
400 GeV Upper Limit (10^{-11}ergs cm^{-2} s^{-1})	0.29	0.53	0.80	1.1

TABLE 5.3: Gamma-ray flux 90% upper limits on spectroscopically resolved radio galaxies associated with members of the Perseus and Abell 2029 clusters of galaxies. The 20 cm flux data are from The NRAO VLA Sky Survey (Condon et al., 1998).

distance from the cluster core. Flux upper limits have been scaled based upon the assumed spectral shape after absorption.

5.3 Interpretation and Discussion

The final result of our search for TeV emission from the Perseus and Abell 2029 clusters of galaxies is shown in Figure 5.8 compared with previous upper limits from EGRET (Reimer et al., 2003), and the results of model calculations. The lines show models of the CRp induced gamma-ray emission normalized to the EGRET upper limits, assuming a CRp spectrum with differential spectral index of -2.1 (Pfrommer and Enßlin, 2004). This index is a reasonable choice of the source spectrum because galaxy clusters are not "leaky" and retain all CRp, unlike our Galaxy where leakage

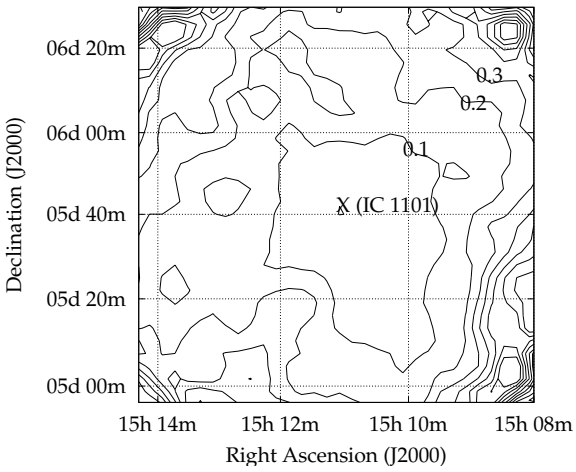

FIGURE 5.7: Gamma-ray flux upper limit map (90% confidence level) from point sources of the inner 1 degree of the Abell 2029 cluster of galaxies. The scale is in units of the flux from Crab Nebula with each contour step equal to 0.1 times the Crab flux. Select contours are labeled. The location of the central brightest radio galaxy is shown.

TABLE 5.4: Upper limits for the diffuse CRp emission from Perseus and Abell 2029 using various angular cuts. The 0.2° cut is relevant for point source and dark matter emission. The 0.3° cut is the optimal cut for the extended emission while the 0.8° one contains the emission from a large fraction of the field-of-view. The scaling factor is used to convert upper limits from Crab units to differential fluxes, taking into account the expected spectral shape.

Cluster	Angular Cut (Degrees)	Significance (Sigma)	400 GeV Flux Upper Limit (Crab)	400 GeV Flux Upper Limit (10^{-11}ergs cm^{-2} s^{-1})	Scaling Factor
Perseus	0.2	-2.3	0.047	0.29	0.80
Perseus	0.3	-2.1	0.13	0.80	0.80
Perseus	0.8	-0.91	0.12	0.74	0.80
Abell 2029	0.2	-1.2	0.10	0.87	1.1
Abell 2029	0.3	-0.15	0.14	1.2	1.1
Abell 2029	0.8	-0.79	0.25	2.2	1.1

of high energy CRp is thought to steepen the source spectrum of -2.1 to the observed value of -2.7. If we assume a spectral index of -2.3, the Whipple and EGRET upper limits are equivalent. Also shown on this plot (as a thinner extension to the main lines) is a prediction of the emission modified by extragalactic extinction owing to pair production processes of TeV photons with photons of the cosmic infrared background ($\gamma_{TeV} + \gamma_{CIB} \rightarrow e^+ + e^-$). The extinction calculation assumes the phenomenological background model ("P0.45") of (Aharonian et al., 2005) (see Chapter 2). Extragalactic extinction has only a minor impact on the flux predictions for Perseus owing to its low redshift. Abell 2029, however, is significantly farther away and extinction does influence the observed spectrum which we take into consideration when calculating upper limits. The Whipple upper limits (this publication) lie by factors of 4.6 (Perseus) and 4.2 (Abell 2029) below the model extrapolations. If the CRp spectrum indeed follows a power law distribution with differential spectral index of -2.1 up to multi-TeV energies, the calculations of (Pfrommer and Enßlin, 2004) together with our results imply that the non-thermal CRp energy density is less than 7.9% of the thermal energy density for the Perseus cluster.

If we optimistically assume that the TeV emission from the galactic center (Aharonian et al., 2004; Kosack et al., 2004; Tsuchiya et al., 2004; Horns, 2005) originates entirely from dark matter annihilations, we can compute the expected dark matter annihilation spectra from the clusters by scaling the gamma-ray flux from the galactic center (shown as the lower lines in Figure 5.8). This was done by computing the expected Galactic Center annihilation signal from a Navarro, Frenk and White (NFW)

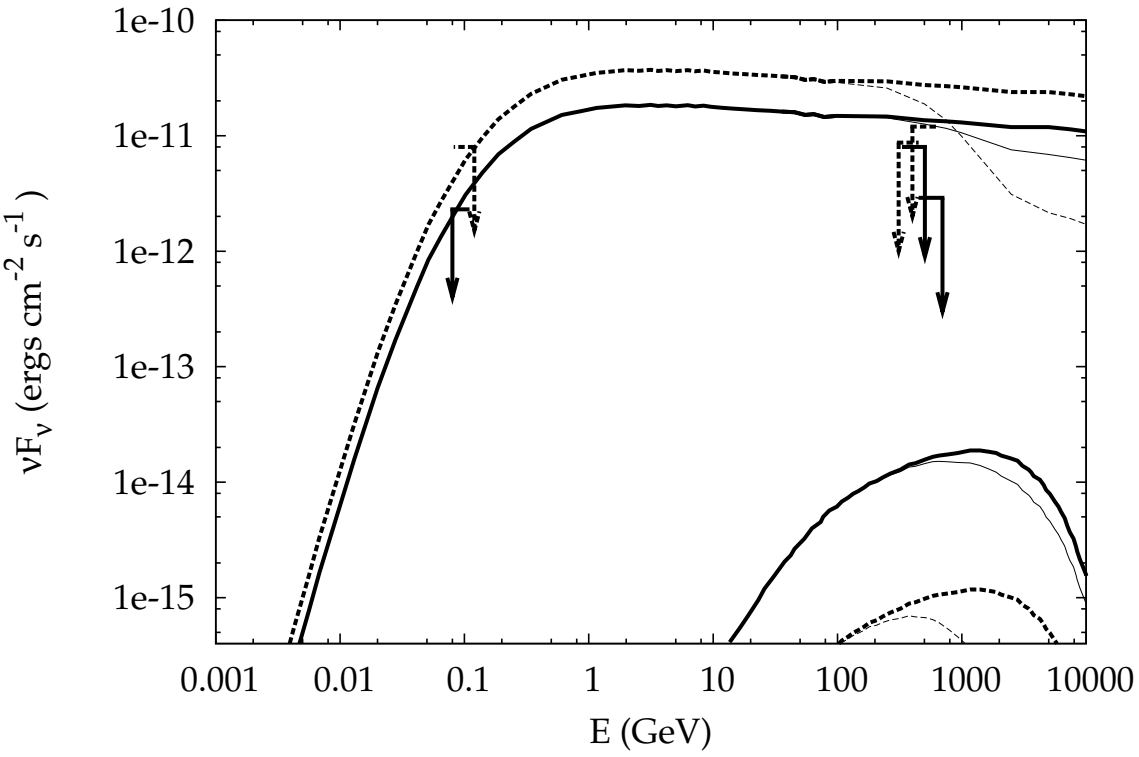

FIGURE 5.8: In this plot, the solid lines correspond to the Perseus cluster and the dashed to Abell 2029. The Whipple 90% upper limits on the emission from the clusters are plotted at 400 GeV (offset to improve readability) with the higher values in each case corresponding to an angular cut of 0.3° (optimized for the search for diffuse CRp emission) and the lower to a cut of 0.2° (optimized for the search for point sources and dark matter). The upper solid and dashed lines show the CRp induced pion decay gamma-ray emission (Pfrommer and Enßlin, 2004) normalized to the EGRET 100 MeV upper limit (shown at 100MeV). Also plotted (the lower flux emission at the bottom right) is the dark matter emission derived under the assumption that the TeV gamma-ray signal from the galactic center originates from the annihilation of an 18 TeV neutralino (Horns, 2005) which should be compared to the point source upper limits (0.2° cut). The thin lines emanating from the pion and dark matter spectra show the effect of extragalactic extinction owing to pair production processes.

halo (Bergström et al., 1998) with $\rho \propto (r/r_s(1+r/r_s)^2)^{-1}$, virial radius $r_s \simeq 290$ kpc, a halo mass of 4×10^{14}, a distance of 75 Mpc and an NFW concentration parameter of $c \simeq 4$. It turns out that the best sensitivity (signal to background noise ratio) is obtained if we use the same radial cut, $\theta = 0.3°$, as for the search for point sources (reducing background from misidentified CR air showers) with the result being that the expected dark matter signal lies two orders of magnitude or more below our upper limits. We will not see dark matter emission even if all of the TeV galactic center emission is dark matter in origin. Thus, we do not provide any new constraints on TeV galactic center emission. Secondly, our calculations show that the most promising region to observe dark matter is the galactic center.

Though we did not detect significant TeV gamma rays from these two clusters of galaxies, we are able to determine two different types of upper limits on the emission: from point sources within the cluster and upper limits on the extended emission. Long duration observations with the more sensitive TeV telescopes VERITAS, H.E.S.S., MAGIC, and CANGAROO III and the GeV telescope GLAST will be critical for determining whether cluster are emitters of high energy gamma rays (See Chapter 7).

Chapter 6

Detector Development

Cadmium Zinc Telluride (CZT) has emerged as the detector material of choice for X-rays in the energy range from 10 keV to $\sim$ 1 MeV. CZT is a high Z semiconductor which can be produced in thick ($\sim 1\,''$) crystals that provide good stopping power and energy resolution without the need for cryogenic cooling. Compared to scintillator detectors, CZT detectors achieve a somewhat better energy resolution (1-2% FWHM at 662 keV, compared to 10% for CsI and 3% for $LaBr_3$) and *at the same time* much better spatial resolutions (sub-mm compared to mm-cm for scintillators). CZT has the advantage of higher Z over Si (the mean Z of CZT is 50 while Si is 14) and does not have to be cooled like Ge. This provides a tremendous possibility to observe the universe in the $>$ 10keV energy range that has not been studied in depth.

6.1 EXIST

EXIST is a proposed hard X-ray sky-survey mission. In its current iteration, the Energetic X-ray Imaging Survey Telescope (EXIST) mission will survey the sky in hard X-rays (5-600 keV) every 95 minutes using a coded masked detector. It consists of two large area detector arrays: a High Energy Telescope (HET), made of CZT to observe 10-600 keV, and a Low Energy Telescope (LET), made of Si to detect photons from 5-30 keV. The HET is an array of coded aperture telescopes covering $131^\circ \times 65^\circ$, with a total detector area of 5.6m^2 CZT, while the LET is 4 arrays of coded aperture telescopes, with a similar FoV but a total area of 1.1m^2 (Grindlay, 2005). See Figure 6.1 for an overview of the instrument. Above the energy levels used in Chandra and XMM, photons can no long be focused using traditional means; other methods must be employed. The plan for EXIST is to use Coded Masked Apertures as used on Integral and SWIFT. A coded mask is placed above the main detector array (in this case, CZT or Si) which is transparent or opaque in a predetermined pattern. The flux from an object at any point in the sky will project a shadow on the detector and by deconvolving this shadow with the coded mask, the observer can determine the brightness distribution with high accuracy (See Figure 6.2).

The main science goals of EXIST (following Grindlay (2005)) are to reveal obscured super massive Black Holes as well as to measure the birth of the first Black Holes in gamma-ray burst explosions. EXIST will also study Black Holes in the galaxy and AGN as probes on the high energy universe. EXIST will excel as a survey

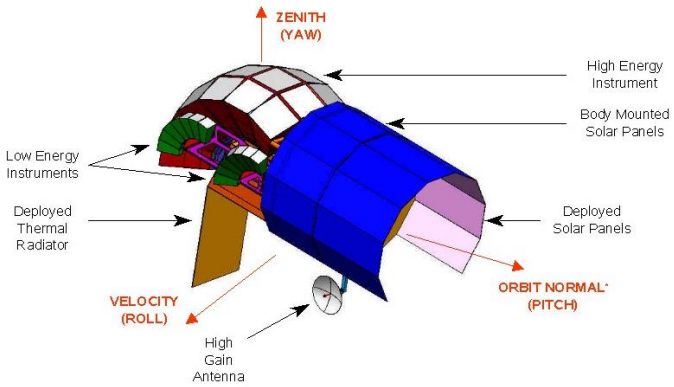

FIGURE 6.1: Schematic drawing of EXIST. The HET will detect photons from 10-600 keV and the LET will be sensitive in the range 5-30 keV (Figure from `http://exist.gsfc.nasa.gov`)

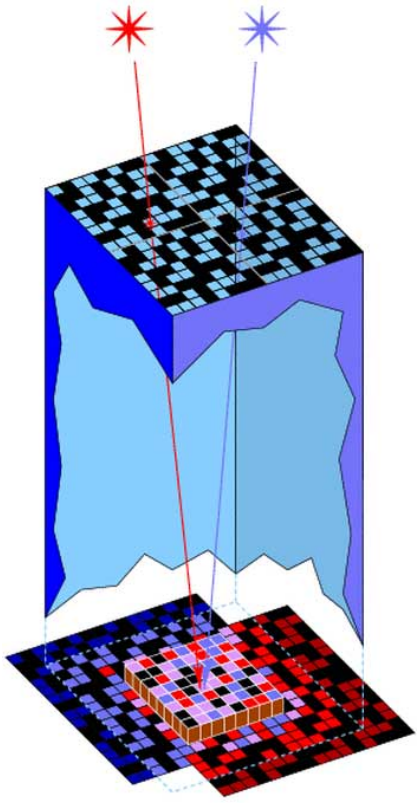

FIGURE 6.2: Schematic of a coded mask imager. The figure shows the case of two distinct sources with the superposed shadows on the CZT detector at the bottom. Deconvolving the shadow image, the sky brightness distribution can be inferred (Figure adapted from `http://isdc.unige.ch`).

instrument but will need a detector area of $6m^2$ of CZT whose properties are well known.

The chapter details results from testing standard IMARAD detectors similar to those which might be used on EXIST with a time resolved readout (Sections 6.2 and 6.3), which allowed me to investigate various ways to correct the anode signals for the depth of the primary interaction. I developed a simplified detector model to compare the measured signals with simulations (Section 6.5).

6.2 Equipment

The CZT crystals used here were produced by IMARAD[1] using the modified high-pressure Bridgeman growth technique. The 2 cm x 2 cm x 0.5 cm detectors were contacted with a single Indium cathode and 8×8 1.6 mm square Indium pixels at a 2.5 mm pitch at the production facility. Li et al. (2001), Hong et al. (2004) and Narita et al. (2000, 1999) previously studied detectors from IMARAD. The cathode channel plus three centrally located anode pixels were connected through electronics with an analog bandwidth of 100 MHz, similar to that described by Matteson et al. (2003), which measures the drift time of electrons in the detector to a resolution of 10 ns. Sixteen other pixels were attached to a pulse-height measuring ASIC.[2] All of the electronics were designed for low noise, making use of batteries for power and

[1] IMARAD Imaging Systems, Ltd., RabinPark, 10 Plaut Street, Rehovot, ISRAEL

[2] eVProducts, 373 Saxonburg Boulevard, Saxonburg, PA, 16056

high-voltage, as well as cooled external FETS and ground isolation. The signals from the 100 MHz and ASIC electronics were digitized by a 500 MHz oscilloscope and Pulse Height Analysis PC board respectively. See Appendix D for more information on the digital acquisition system.

6.3 Measurements

Cs^{137} produces an X-ray line at 662 keV and was used to produce interactions such as those seen in Figure 6.3 within the detector by irradiating the CZT from the cathode side. Since this is such a high energy source, most of the photons produced do not interact with the CZT, but those that do are to first order homogeneously distributed within the detector. When a photon interacts with the detector it produces an electron-hole cloud. Since the detector is biased at -500 V on the cathode side with the pixels held at ground, the electrons will drift towards the pixels with an almost constant velocity according to

$$\vec{V}(\vec{x}) = \mu\vec{E}(\vec{x}) \tag{6.1}$$

where μ is the electron mobility. The holes are trapped quickly and contribute little to the induced signal. To determine the signal on any particular contact within the detector, one must compute the weighting potential for that contact. This is done by setting the voltage contact under consideration to one while holding all of the other contacts at ground and computing the electric potential throughout the detector. Once this is known, the induced current due to an electric charge moving within the

detector is given by

$$I = ev\phi(\vec{x}) \tag{6.2}$$

where e is the charge. The holes do not contribute to this signal and the weighting potential has a steep gradient directly in front of the pixels causing the greatest signal to be induced shortly before they reach the pixels. This "small pixel effect" (Barret et al., 1995) is seen in Figure 6.3 by a peak in the anode current toward the end of the pulse. The small pixel effect is beneficial because we can accurately measure the drift time of the electrons as well as neglect the influence of the holes. During their drift, some electrons are trapped which can be seen in this figure by an exponential decrease in the cathode current (quantified by the trapping time τ).

6.4 Cs^{137} Spectra

From data as shown in Figure 6.3, we determined the drift time of the electron cloud in the detector by measuring the pulse time and the amplitudes of the anode and cathode pulses. The drift time is directly correlated with the depth of interaction in the detector (Kalemci and Matteson, 2002; He et al., 1999). We used the Cs^{137} source to produce several thousand events in the detector and read them with a PC.

There are numerous ways to look at the data. The first is a basic plot of the cathode charge versus the charge induced on an anode pixel (Figure 6.4). The 662 keV photo-effect events produce a clearly recognizable arc. These data can also be histogrammed to directly see the photo-peak (Figure 6.5). The photo-peak has a

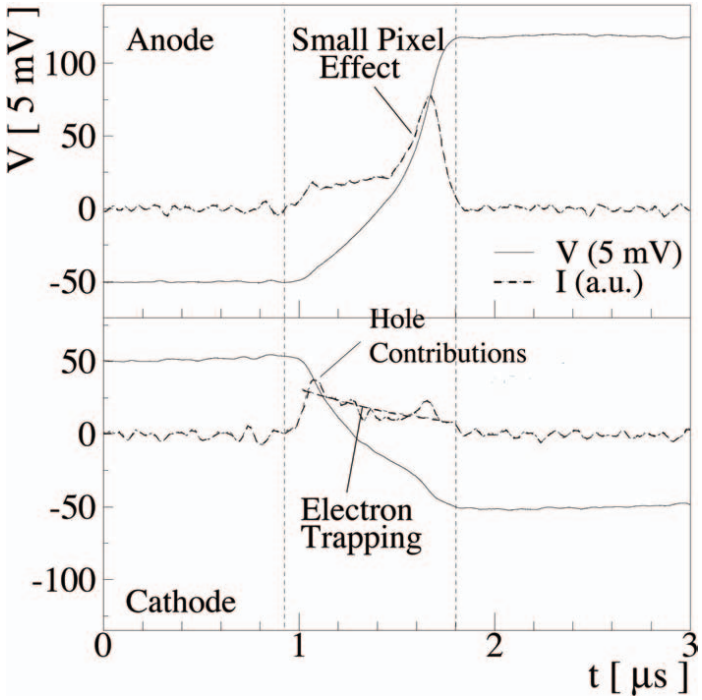

FIGURE 6.3: This figure shows an electronic pulse produced when an X-ray photon interacts with the detector. The upper panel shows the signal on the anode pixel while the bottom shows the cathode. In both plots the solid line is proportional to the charge induced while the dashed line is the time derivative of that charge (current). By demarking the beginning and end of the anode pulse (the solid lines), one can determine the drift time of the electron cloud within the detector. The sharp increase in current toward the end of the pulse is indicative of the small pixel effect, while the slow decrease in the current on the cathode shows some electron trapping.

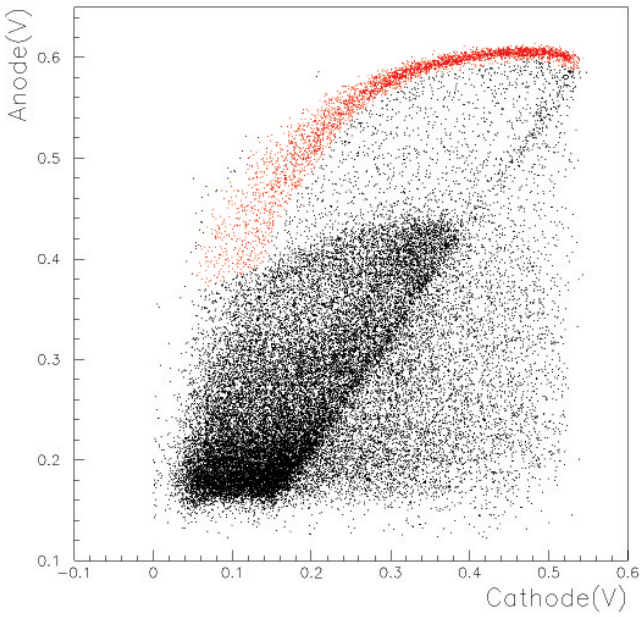

FIGURE 6.4: Spectrum obtained from the CZT detector using a Cs^{137} source. This plot shows the anode charge versus cathode charge. The curved line is the 662 keV line without correction. The Compton continuum is also apparent.

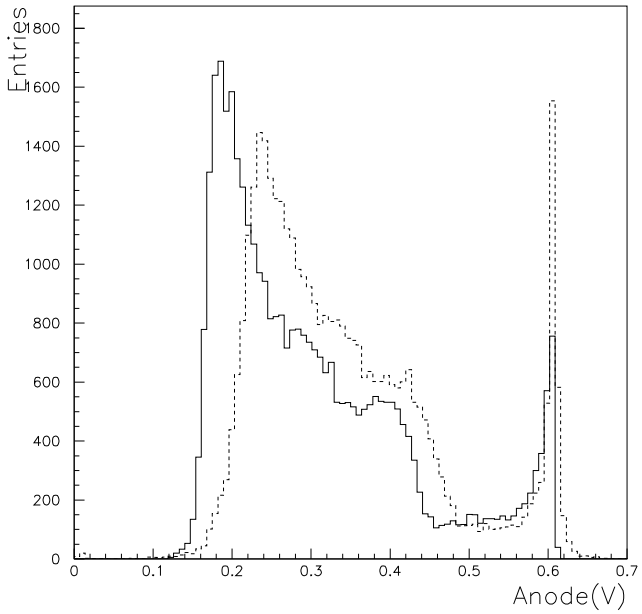

FIGURE 6.5: This plot is an histogram of the data in Figure 6.4. The solid line is the uncorrected (raw) spectrum and the dashed line is the spectrum corrected for the charge curvature. This corrections improves the FWHM from 2.33% to 2.15% while increasing the photopeak efficiency by 57%.

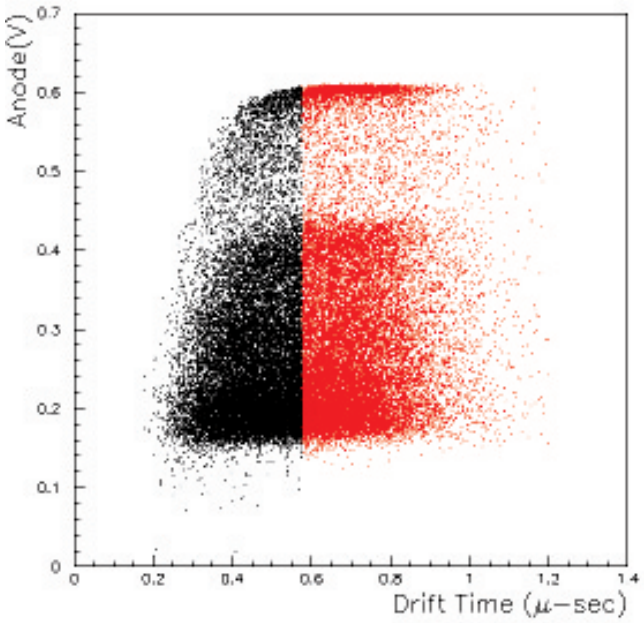

FIGURE 6.6: This figure shows the same data as before plotted as anode charge versus Drift Time. The 662 keV line and Compton continuum are apparent. The plot shows that the photo-effect line widens for smaller drift times. The events shown in red are those selected as "good" events (time $> 0.57\mu - \text{sec}$) in Figure 6.7

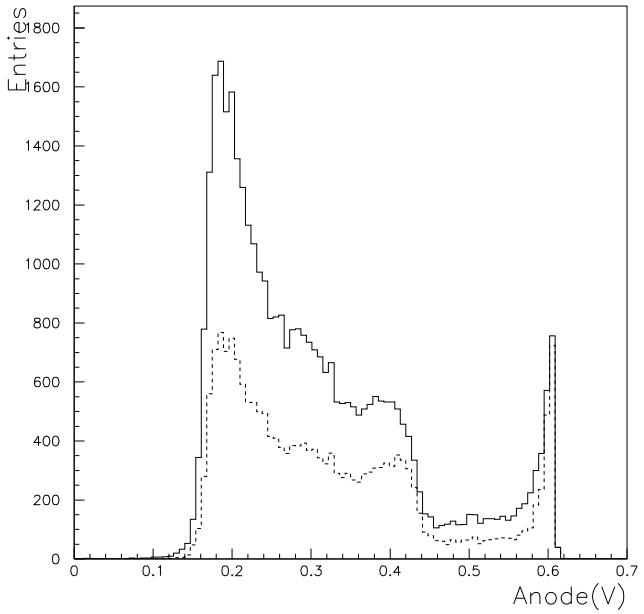

FIGURE 6.7: Cs^{137} spectrum. The solid line is the uncorrected spectrum and the dashed line is the spectrum after selecting events with drift times longer than 0.57 μ-sec from Figure 6.6

FWHM of 2.33% before any type of correction. Correcting for the curvature or depth of interaction in Figure 6.4 improves the energy resolution to 2.15% and increases the photo-peak efficiency by 57%, which is apparent by looking at the dashed line in Figure 6.5. Hong et al. (2004) reported similar improvements. We estimate that the actual energy resolution is 1.8% (1.6% after correction) by subtracting the electronic resolution in quadrature.

These same data are plotted in Figure 6.6 as the anode amplitude versus the drift time. The photo-peak is still obvious, but there is no clear correlation correction. One can see that the photo-peak becomes more spread out for short drift times. Thus, only using events with drift times larger than $0.57\mu-$sec improves the energy resolution from 2.33% to 2.12% (1.5% after subtracting electronic noise), but the photo-peak efficiency decreases by 14% (see Figure 6.7).

6.5 Simulations and Comparison to Experimental Results

I created a simulation based on a two-dimensional model to better understand the underlying processes. I tuned the model to match the standard IMARAD detector by setting the pixel widths to be the same but allowing for a larger pixel pitch to mimic the 3-D geometry. I used a commercial semiconductor device simulator package called ATLAS[3] to determine the weighting potential for each pixel and the electric field

[3] SILVACO International, Inc., 4701 Patrick Henry Drive, Building 2, Santa Clara, CA95054

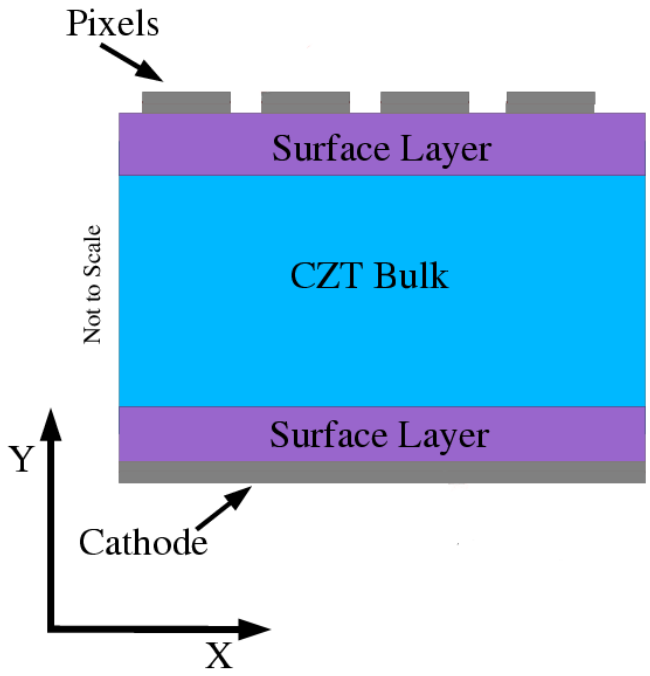

FIGURE 6.8: Graphical representation of the simulation model. There are contact electrodes and a cathode on top of a layer that simulated contact resistance. There are also two surface layers and a CZT bulk layer.

within the detector. The CZT was modeled with a bulk region and several different layers to mimic surface conductivity and contact resistance. The bulk is doped with 1.5×10^6 electrons/cm^3. We used surface layers with a higher electron concentration than the bulk to simulate the surface conductivity (Bolotnikov et al., 2002). We also included significant contact resistance based on pixel-cathode and pixel-pixel I-V measurements. Figure 6.8 shows a diagram of the model. Using the weighting potential and electric field provided by the ATLAS model, I tracked electrons through the detector using my own code by determining their velocity by the electric field and assumed mobility. This produces events similar to the actual ones seen in CZT.

Using the above model to produce several thousand events, one can compare a simulated spectrum to the actual data (see Figure 6.9). By tuning the mobility and trapping parameters of the simulations, we can fit the two data sets to each other so as

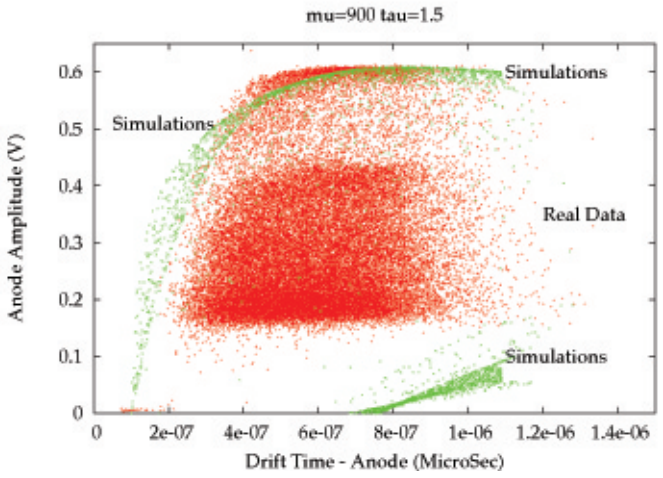

FIGURE 6.9: Comparison of simulated and experimental data. Events at long-drift times are simulated well while events at short-drift times are not. We suspect that some of these events are occurring between pixels and that holes are playing an important part. While there are only photo-effect events in the simulations, the real data shows also the Compton continuum.

to optimize the agreement between the simulation and the data. The electron mobility is directly shown by the longest drift times, where the trapping is constrained by the slope of the photo-peak because longer drift time events will produce less charge due to the charge loss. We find that the simulation deviates from the data in the region of short drift times which is most likely due to only modeling two dimension and by the neglecting of holes (see Figure 6.10). This indicates that the electric field as well as the weighting potential are not simulated correctly between pixels. According to Jung et al. (2005) the holes become important at short drift times. There are also model deficiencies in the contact properties and surface regions. Based on these simulations μ equals 900 $cm^2V^{-1}s^{-1}$ and τ equals 1.9 μ-sec. Previous studies of IMARAD detectors have shown similar results (Li et al., 2001) but depend strongly on the assumed contact resistance.

A very powerful tool with the simulations is that you know exactly where in the detector an interaction occurs. Figure 6.10 presents the charge induced on the anode

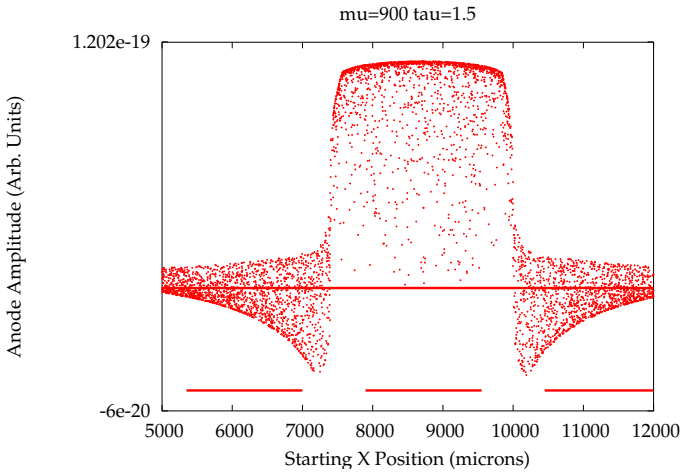

FIGURE 6.10: Charge induced versus starting position. The horizontal lines at the bottom represent pixel locations. The most charge is induced on the center pixel when events occur directly above the pixel while less or even negative charge is induced for off pixel events. See Figure 6.8 for a description of the orientation of the axis.

versus the initial interaction position (only the horizontal interaction position and not the depth of interaction). The pixels are shown as horizontal lines along the bottom with the pixel under observation being the middle line. The most charge is induced when an event occurs directly above a pixel while off-pixel events are less energetic. This indicates there is charge sharing between neighboring pixels which has been seen in other CZT detectors (Bolotnikov et al., 1999). There are also events occurring above other pixels that induce negative charge on the observed pixel. In the real data, events with low anode charges are masked by the Compton events and are not observed.

6.6 Summary and Outlook

In summary we have made measurements of the photo-peak of a 662 keV Cs^{137} line using standard Indium contacted IMARAD detectors giving a FWHM of 2.15% (1.6% after subtracting the electronic contribution). We can realize such FWHM by

correcting for the depth of interaction with the help of the anode to cathode charge ratio. One of the limiting factors to resolution is the presence of leakage current at high voltages and the determination of this effect is very important (see Appendix C.These detectors are substantially less expensive than standard high-pressure Bridgman CZT and are thus extremely promising for experiments requiring large detector areas such as EXIST or other such instruments (see Chapter 7).

Chapter 7

Conclusions

Galaxy clusters are the largest and most massive gravitationally bound systems in the universe. In this thesis, I reported on observations of three clusters; 3C 129, Perseus and Abell 2029. The observations of the three clusters can be divided into two distinct classes: X-ray observations of 3C 129 and TeV observations of the Perseus and Abell 2029 clusters. Galaxy clusters are bright X-ray sources due to the thermal emission of the hot ICM and may be emitters of TeV gamma rays from non-thermal hadrons accelerated by shocks, galactic winds or AGN. The observations presented here had two different goals. In the case of 3C 129 it was to verify and expand on the Chandra results reported on by Krawczynski et al. (2003), specifically to look for deficits in the X-ray surface brightness along the radio tail and to search for a possible diffuse excess in the region in front of the radio tail. The TeV observations had a different task in that VHE gamma rays had previously not yet been seen from clusters and our goal was to search for such emission. The detection of TeV gamma rays from

clusters would allow us to constrain the energy density of non-thermal particles in clusters.

Using the XMM-Newton X-ray observatory, we observed the prototypical head-tail radio galaxy 3C 129, first searching for deficits due to the non-thermal radio plasma displacing the thermal ICM. We report an upper limit of 1.5% on the fractional deficit within the radio jet which is much smaller than the expected 10% change. This suggests that there is some mixing of the thermal and non-thermal plasmas. If the deficit was on the order of what we suspect, we could have computed the plasma volume filling factor and further constrain the magnetic energy density of the plasma. Krawczynski et al. (2003) saw marginal evidence for extended emission in front of the radio galaxy at the head of the jet which would indicate the presence of a compressed higher density plasma. Since the angular resolution of XMM is not good enough to resolve a feature of this size, I fit a power-law to a larger region that includes both the core and the extended feature. This shows that there is 62% more flux from the larger XMM region than the Chandra point source, indicating that there is some type of extended emission. However, the XMM excess is smaller than expected from the tentative Chandra detection. Unfortunately, we cannot further localize the excess with XMM.

Using the Whipple 10 m Cherenkov telescope, we searched for TeV gamma-ray emission from the Perseus and Abell 2029 clusters. The first task was a point source search using the standard parameterization technique which resulted in the production of an upper limit map (Figures 5.6 and 5.7). There were no discernible VHE

point sources within either of the clusters. We reported upper limits at the locations of several point sources within the clusters, including the CD galaxies (see Table 5.3). Finally, several authors have suggested that there would be diffuse VHE emission from clusters of galaxies due to a population of non-thermal particles. We assumed that the non-thermal particles mimic the distribution of the thermal ICM. Based on this assumption, we looked for extended emission at several radial distances for Perseus and Abell 2029 and compared these with model calculations. For the Perseus cluster, our results imply that the cosmic ray proton energy density is less than 7.9% of the thermal energy density if the CRp spectrum follows a power-law with spectral index of -2.1 all the way to TeV energies. TeV gamma-rays might also originate from dark matter, so we compared our result to a possible dark matter annihilation spectrum. Unfortunately, due to the distance and mass of these objects, it lies several orders of magnitude below the sensitivity of the Whipple telescope. A paper describing these results is in press in the Astrophysical Journal (Perkins et al., 2006).

7.1 Future Cluster Observations

Chandra and XMM reached the best performance that can be achieved with a Wolter mirror design and Si CCDs. Chandra, with its < 0.5 arcsecond resolution and XMM with its large detector area are arguably the best that the field of Wolter mirrors and silicon CCDs has to offer. Designing observatories that can give complementary information to that obtained with Chandra and XMM with an equal or

smaller amount of resources requires different technology. In the following I will describe proposed and under construction experiments that are expected to have an impact on the study of non-thermal emission from galaxy clusters.

7.1.1 NuSTAR and GLAST

The satellite-borne Nuclear Spectroscopic Telescope Array (NuSTAR, and later the Constellation-X mission, see Hornschemeier et al. (2005)) would extend the capabilities of Chandra into the hard X-ray band (6 keV up to 80 keV) by using grazing incidence mirrors to focus photons with a focal length of ten meters together with 2 mm thick CZT detectors (Harrison et. al., 2004). This would be very useful for cluster research. Figure 7.1 compares the effective area of NuSTAR with current observatories. The main science objectives of NuSTAR are similar to EXIST and include a Black Hole survey (looking for obscured black holes). It will also be very useful for pointed observations of clusters, Super Nova Remnants, and AGN. Using the RXTE satellite, Gruber and Rephaeli (2002) reported tentative evidence of non-thermal emission from Abell 2319 at the very end of the thermal bremsstrahlung emission above 10 keV. If there is such emission, then NuSTAR, with a sensitivity that is one order of magnitude higher than that of RXTE and extends all the way to 80 keV, would definitely detect it. NuSTAR might probe the region between the thermal and the non-thermal.

GLAST is another satellite-borne instrument with a viable detection range between the ground based IACTs and the current X-ray missions (Ritz et al., 2005).

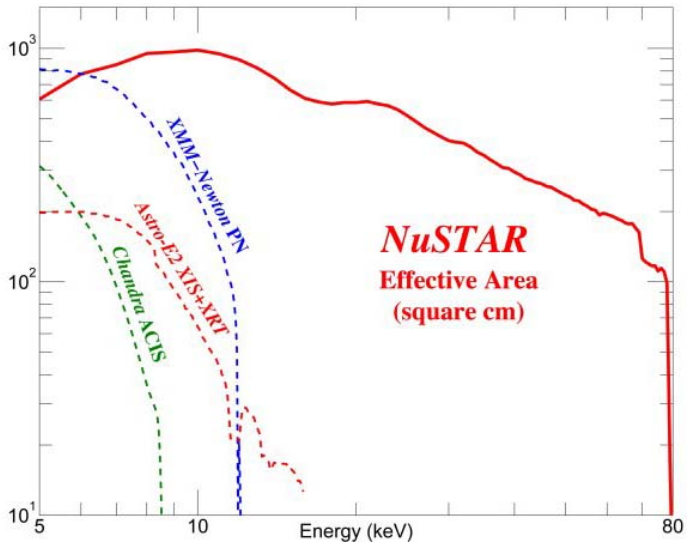

FIGURE 7.1: The effective area of the proposed NuSTAR mission using CZT detectors. NuSTAR would be ideal for detecting non-thermal tails in the ICM X-ray energy spectra (Figure from http://www.nustar.caltech.edu).

GLAST is a Silicon pair tracker experiment that will have an energy range from 30 MeV to 300 GeV and will be able to locate sources with an accuracy of 30 arcseconds for the very strongest sources to tens of arcminutes for weak sources. GLAST, being a wide field of view instrument, would take one to two years to achieve the sensitivity needed for these clusters (see Figure 7.2).

7.2 VERITAS and H.E.S.S.

The Very Energetic Radiation Imaging Telescope Array System (VERITAS) is an array of four IACTs currently in construction in Amado, Arizona, near the current site of the Whipple 10 m system (Falcone et al., 2005). Two of the four telescopes are in operation as of the writing of this while the final two are scheduled to be completed in December 2006. The H.E.S.S. (High Energy Stereoscopic System) collaboration has been operating an array of four telescopes in Namibia since December of 2003 (Benbow et. al., 2005). There are several benefits to an array of IACTs over a

single telescope. The better flux sensitivity allows for the detection of faint sources which is vital for the observations of clusters. There is also a reduction in the energy threshold and H.E.S.S has a large FoV. All of these capabilities improve the detection possibilities of clusters. Figure 7.2 is a reproduction of Figure 5.8 with the addition of the flux sensitivity of the VERITAS and H.E.S.S. arrays and the GLAST detector. Observing these clusters (or another such as the Coma cluster) with an array of IACTs will improve our chances of detecting the VHE emission from very energetic non-thermal particles in clusters. The H.E.S.S. collaboration has already shown the power of these types of instruments (see Aharonian (2005) for an overview of their results).

The next generation of instruments promises to shed new light on the field of cluster astrophysics in the high energy and very high energy range. The increased sensitivity of VERITAS and H.E.S.S. will allow us to probe faint emission from nearby galaxy clusters to search for non-thermal particles. The addition of space based platforms such as GLAST and, if approved, NuSTAR will open a new window on cluster observations. It is important to note that the time between the first three generations of X-ray satellite instruments was only nine years. Chandra and XMM were launched within a few months of each other in 1999. NuSTAR and EXIST were scheduled to launch at the end of the decade but have been delayed repeatedly. The future looks bright for high energy cluster research but only if current schedules are kept.

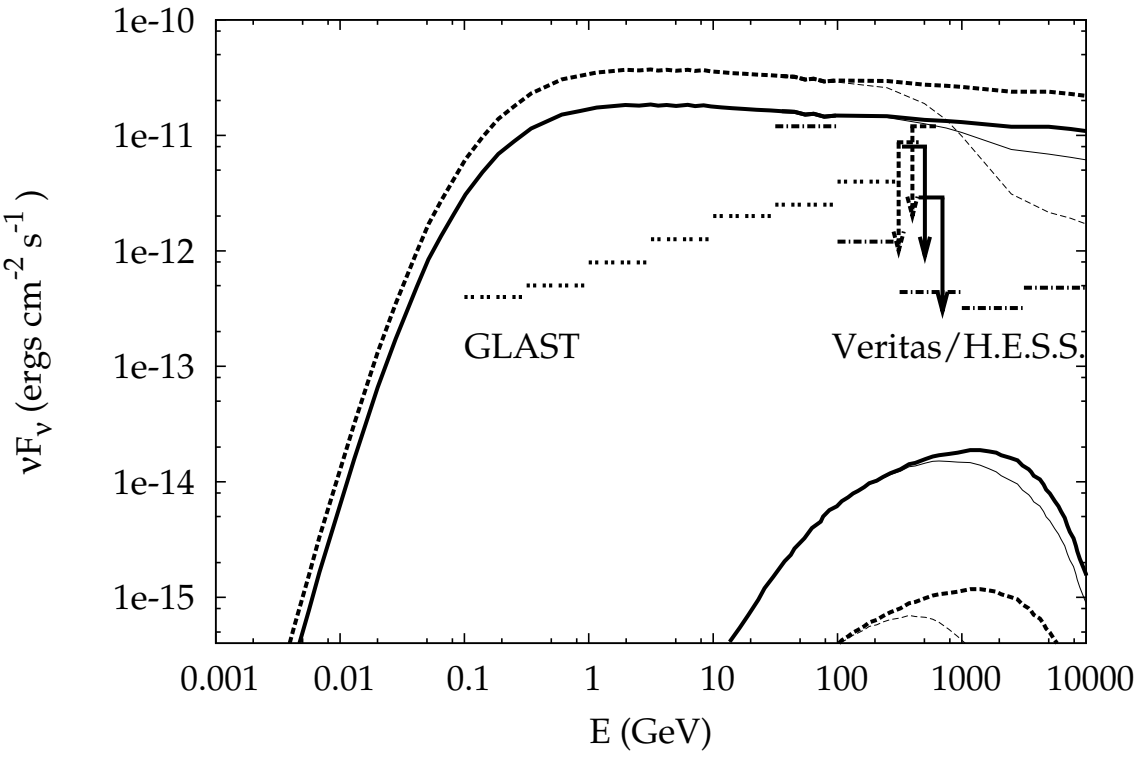

FIGURE 7.2: This plot is a duplicate of Figure 5.8 with the addition of the predicted sensitivity of the VERITAS or H.E.S.S. arrays (for a 50 hr observation) shown as the dashed-dotted lines and the sensitivity of GLAST (for a 2 year observation) as the double dotted lines. As a reminder, the solid lines correspond to the Perseus cluster and the dashed to Abell 2029. See Figure 5.8 for more details on the upper limits and models.

Appendix A

3C 129 Observation Summary

The following tables detail the observations of 3C 129 by the XMM-Newton Observatory. The first few tables provide information on the duration and type of observation requested while the final table is a detailed list of the data runs.

Table A.1: 0146490101 Observation Data File Summary

Revolution	Target	Scheduled Length	Observer
0585	3C 129	38918	Dr Henric Krawczynski

Table A.2: Proposal Target Information

Target :	3C 129
RA :	04h49m9.10 s (4.8192 hours)
Dec :	45D00m39.00s (45.0108 deg)
Prop Duration :	40000 seconds
Alt Names :	N/A
Boresight RA :	04h49m9.10 s (4.8192 hours)
Boresight Dec :	45D00m39.40s (45.0109 deg)
Lower Pos Ang :	0
Upper Pos Ang :	360
SC Pos Ang :	N
AO Number :	2
Science Type :	G

Table A.3: Observation Record

Observation ID :	0146490101
Revolution :	0585
Scheduled Start:	2003-02-18T07:24:41.000
Scheduled Stop :	2003-02-18T18:13:19.000

Table A.4: Instrument Information

Instrument	Active	Exposures	Priority
MOS 1	Y	1	0
MOS 2	Y	1	0
OM	Y	7	0
PN	Y	13	0
RGS 1	Y	27	0
RGS 2	Y	27	0

TABLE A.5: Exposure and Configuration Information

Inst	ExpID	Sched?	Mode	Data Mode	Filter	Position	Actual Start	Actual Stop
M1	S001	Y	PrimeFullWindow	Imaging	Medium	FILTER C	2003-02-18T07:25:26	2003-02-18T18:09:58
M2	S004	Y	PrimeFullWindow	Imaging	Medium	FILTER C	2003-02-18T07:25:27	2003-02-18T18:09:57
OM	S009	Y	Image	Imaging	V		2003-02-18T07:33:47	2003-02-18T08:49:06
OM	S010	Y	Image	Imaging	V		2003-02-18T08:54:14	2003-02-18T10:09:34
OM	S012	Y	Image	Imaging	V		2003-02-18T10:15:05	2003-02-18T11:08:49
OM	S013	Y	Image	Imaging	V		2003-02-18T11:57:20	2003-02-18T12:51:04
OM	S014	Y	Image	Imaging	B		2003-02-18T13:39:11	2003-02-18T14:54:30
OM	S015	Y	Image	Imaging	B		2003-02-18T14:59:39	2003-02-18T16:14:58
OM	S016	Y	Image	Imaging	B		2003-02-18T16:20:29	2003-02-18T17:14:15
PN	U002	N	PrimeFullWindow	Imaging	Medium		2003-02-18T08:27:25	2003-02-18T18:05:02
PN	U003	N	UNDEFINED	DiscardedLinesData			2003-02-18T18:08:34	2003-02-18T18:08:35
PN	U004	N	UNDEFINED	DiscardedLinesData			2003-02-18T18:08:53	2003-02-18T18:08:54
PN	U005	N	UNDEFINED	DiscardedLinesData			2003-02-18T18:09:13	2003-02-18T18:09:14
PN	U006	N	UNDEFINED	DiscardedLinesData			2003-02-18T18:09:39	2003-02-18T18:09:40
PN	U007	N	UNDEFINED	DiscardedLinesData			2003-02-18T18:10:00	2003-02-18T18:10:01
PN	U008	N	UNDEFINED	DiscardedLinesData			2003-02-18T18:10:18	2003-02-18T18:10:19
PN	U009	N	UNDEFINED	DiscardedLinesData			2003-02-18T18:10:44	2003-02-18T18:10:45
PN	U010	N	UNDEFINED	DiscardedLinesData			2003-02-18T18:11:04	2003-02-18T18:11:05
PN	U011	N	UNDEFINED	DiscardedLinesData			2003-02-18T18:11:23	2003-02-18T18:11:24
PN	U012	N	UNDEFINED	DiscardedLinesData			2003-02-18T18:11:51	2003-02-18T18:11:52
PN	U013	N	UNDEFINED	DiscardedLinesData			2003-02-18T18:12:09	2003-02-18T18:12:10
PN	U014	N	UNDEFINED	DiscardedLinesData			2003-02-18T18:12:28	2003-02-18T18:12:29
R1	S007	Y	HighEventRateWithSES	Spectroscopy			2003-02-18T07:24:41	2003-02-18T18:13:19
R1	S900	Y	UNDEFINED	Diagnostic			2003-02-18T07:24:41	2003-02-18T07:24:42
R1	S901	Y	UNDEFINED	Diagnostic			2003-02-18T07:24:41	2003-02-18T07:24:42

Continued on next page.

Inst	ExpID	Sched?	Mode	Data Mode	Filter	Position	Actual Start	Actual Stop
R1	S902	Y	UNDEFINED	Diagnostic			2003-02-18T07:24:41	2003-02-18T07:24:42
R1	S903	Y	UNDEFINED	Diagnostic			2003-02-18T07:24:41	2003-02-18T07:24:42
R1	S904	Y	UNDEFINED	Diagnostic			2003-02-18T07:24:41	2003-02-18T07:24:42
R1	S905	Y	UNDEFINED	Diagnostic			2003-02-18T07:24:41	2003-02-18T07:24:42
R1	S906	Y	UNDEFINED	Diagnostic			2003-02-18T07:24:41	2003-02-18T07:24:42
R1	S907	Y	UNDEFINED	Diagnostic			2003-02-18T07:24:41	2003-02-18T07:24:42
R1	S908	Y	UNDEFINED	Diagnostic			2003-02-18T07:24:41	2003-02-18T07:24:42
R1	S909	Y	UNDEFINED	Diagnostic			2003-02-18T07:24:41	2003-02-18T07:24:42
R1	S910	Y	UNDEFINED	Diagnostic			2003-02-18T07:24:41	2003-02-18T07:24:42
R1	S911	Y	UNDEFINED	Diagnostic			2003-02-18T07:24:41	2003-02-18T07:24:42
R1	S912	Y	UNDEFINED	Diagnostic			2003-02-18T07:24:41	2003-02-18T07:24:42
R1	S913	Y	UNDEFINED	Diagnostic			2003-02-18T07:24:41	2003-02-18T07:24:42
R1	S914	Y	UNDEFINED	Diagnostic			2003-02-18T07:24:41	2003-02-18T07:24:42
R1	S915	Y	UNDEFINED	Diagnostic			2003-02-18T07:24:41	2003-02-18T07:24:42
R1	S916	Y	UNDEFINED	Diagnostic			2003-02-18T07:24:41	2003-02-18T07:24:42
R1	S917	Y	UNDEFINED	Diagnostic			2003-02-18T07:24:41	2003-02-18T07:24:42
R1	S918	Y	UNDEFINED	Diagnostic			2003-02-18T07:24:41	2003-02-18T07:24:42
R1	S919	Y	UNDEFINED	Diagnostic			2003-02-18T07:24:41	2003-02-18T07:24:42
R1	S920	Y	UNDEFINED	Diagnostic			2003-02-18T07:24:41	2003-02-18T07:24:42
R1	S921	Y	UNDEFINED	Diagnostic			2003-02-18T07:24:41	2003-02-18T07:24:42
R1	S922	Y	UNDEFINED	Diagnostic			2003-02-18T07:24:41	2003-02-18T07:24:42
R1	S923	Y	UNDEFINED	Diagnostic			2003-02-18T07:24:41	2003-02-18T07:24:42
R1	S924	Y	UNDEFINED	Diagnostic			2003-02-18T07:24:41	2003-02-18T07:24:42
R1	S925	Y	UNDEFINED	Diagnostic			2003-02-18T07:24:41	2003-02-18T07:24:42
R2	S008	Y	HighEventRateWithSES	Spectroscopy			2003-02-18T07:24:41	2003-02-18T18:13:15
R2	S900	Y	UNDEFINED	Diagnostic			2003-02-18T07:24:41	2003-02-18T07:24:42
R2	S901	Y	UNDEFINED	Diagnostic			2003-02-18T07:24:41	2003-02-18T07:24:42
R2	S902	Y	UNDEFINED	Diagnostic			2003-02-18T07:24:41	2003-02-18T07:24:42

Continued on next page.

Inst	ExpID	Sched?	Mode	Data Mode	Filter	Position	Actual Start	Actual Stop
R2	S903	Y	UNDEFINED	Diagnostic			2003-02-18T07:24:41	2003-02-18T07:24:42
R2	S904	Y	UNDEFINED	Diagnostic			2003-02-18T07:24:41	2003-02-18T07:24:42
R2	S905	Y	UNDEFINED	Diagnostic			2003-02-18T07:24:41	2003-02-18T07:24:42
R2	S906	Y	UNDEFINED	Diagnostic			2003-02-18T07:24:41	2003-02-18T07:24:42
R2	S907	Y	UNDEFINED	Diagnostic			2003-02-18T07:24:41	2003-02-18T07:24:42
R2	S908	Y	UNDEFINED	Diagnostic			2003-02-18T07:24:41	2003-02-18T07:24:42
R2	S909	Y	UNDEFINED	Diagnostic			2003-02-18T07:24:41	2003-02-18T07:24:42
R2	S910	Y	UNDEFINED	Diagnostic			2003-02-18T07:24:41	2003-02-18T07:24:42
R2	S911	Y	UNDEFINED	Diagnostic			2003-02-18T07:24:41	2003-02-18T07:24:42
R2	S912	Y	UNDEFINED	Diagnostic			2003-02-18T07:24:41	2003-02-18T07:24:42
R2	S913	Y	UNDEFINED	Diagnostic			2003-02-18T07:24:41	2003-02-18T07:24:42
R2	S914	Y	UNDEFINED	Diagnostic			2003-02-18T07:24:41	2003-02-18T07:24:42
R2	S915	Y	UNDEFINED	Diagnostic			2003-02-18T07:24:41	2003-02-18T07:24:42
R2	S916	Y	UNDEFINED	Diagnostic			2003-02-18T07:24:41	2003-02-18T07:24:42
R2	S917	Y	UNDEFINED	Diagnostic			2003-02-18T07:24:41	2003-02-18T07:24:42
R2	S918	Y	UNDEFINED	Diagnostic			2003-02-18T07:24:41	2003-02-18T07:24:42
R2	S919	Y	UNDEFINED	Diagnostic			2003-02-18T07:24:41	2003-02-18T07:24:42
R2	S920	Y	UNDEFINED	Diagnostic			2003-02-18T07:24:41	2003-02-18T07:24:42
R2	S921	Y	UNDEFINED	Diagnostic			2003-02-18T07:24:41	2003-02-18T07:24:42
R2	S922	Y	UNDEFINED	Diagnostic			2003-02-18T07:24:41	2003-02-18T07:24:42
R2	S923	Y	UNDEFINED	Diagnostic			2003-02-18T07:24:41	2003-02-18T07:24:42
R2	S924	Y	UNDEFINED	Diagnostic			2003-02-18T07:24:41	2003-02-18T07:24:42
R2	S925	Y	UNDEFINED	Diagnostic			2003-02-18T07:24:41	2003-02-18T07:24:42

Appendix B

Whipple 10m Run Summary

The following tables show the ON and OFF runs used in the analysis of the Perseus and Abell 2029 clusters as well as the N2 runs (used for calibration). The elevation of the source as well as the date is also given.

Table B.1: Summary of the runs used in the Perseus Cluster analysis

ON	OFF	N2	Elevation	UT Date
gt027494	gt027495	gt027484	64	2004-09-16
gt027612	gt027613	gt027602	61	2004-10-09
gt027645	gt027646	gt027635	51	2004-10-11
gt027697	gt027698	gt027684	73	2004-10-14
gt027699	gt027700	gt027684	80	2004-10-14
gt027715	gt027716	gt027707	58	2004-10-15
gt027763	gt027764	gt027753	80	2004-10-18
gt027789	gt027790	gt027787	77	2004-10-23
gt027791	gt027792	gt027787	68	2004-10-23
gt027856	gt027857	gt027841	73	2004-11-10
gt027858	gt027859	gt027841	63	2004-11-10
gt027876	gt027877	gt027863	77	2004-11-11
gt027878	gt027879	gt027863	68	2004-11-11
gt027916	gt027917	gt027904	75	2004-11-13
gt027918	gt027919	gt027904	65	2004-11-13
gt028002	gt028003	gt027995	59	2004-12-03
gt028117	gt028118	gt028110	78	2004-12-13
gt028119	gt028120	gt028110	78	2004-12-13
gt028122	gt028123	gt028110	66	2004-12-13
gt028143	gt028144	gt028134	71	2004-12-14
gt028145	gt028146	gt028134	61	2004-12-14
gt028165	gt028166	gt028157	66	2004-12-15
gt028180	gt028181	gt028177	75	2004-12-16

Continued on next page.

ON	OFF	N2	Elevation	UT Date
gt028235	gt028236	gt028233	79	2005-01-13
gt028327	gt028328	gt028325	79	2005-01-31
gt028329	gt028330	gt028325	70	2005-01-31
gt028337	gt028338	gt028333	71	2005-02-01
gt028348	gt028349	gt028344	64	2005-02-02
gt028360	gt028361	gt028358	76	2005-02-05

TABLE B.2: Summary of the runs used in the Abell 2029 Cluster analysis

ON	OFF	N2	Elevation	UT Date
gt024026	gt024027	gt024015	60	2003-03-07
gt024244	gt024245	gt024229	60	2003-03-31
gt024270	gt024271	gt024253	63	2003-04-01
gt024442	gt024443	gt024432	56	2003-04-22
gt024452	gt024451	gt024444	64	2003-04-23
gt024464	gt024463	gt024455	61	2003-04-24
gt024479	gt024478	gt024469	57	2003-04-25
gt024482	gt024481	gt024469	64	2003-04-25
gt024495	gt024494	gt024485	59	2003-04-26
gt024529	gt024530	gt024519	62	2003-04-28
gt024579	gt024578	gt024570	63	2003-05-01
gt024615	gt024614	gt024607	62	2003-05-03
gt024644	gt024643	gt024638	64	2003-05-05

Appendix C

I-V Measurements

C.1 Standard Measurements

The goal of the standard I-V measurements is to measure the bulk leakage current through CZT detectors. This setup allows for the automated measurement of several pixels (currently four but could be expanded to eight or more) while ramping up the voltage to a user specified amount. There are several safeguards in place to limit the amount of current flowing through the detector. An example of the possible results are given in Figure C.1. The data acquisition program has been written in LabView.[1]

C.1.1 Apparatus

The goal is to determine the current through the CZT (I_d). See Figure C.2 for a schematic of the setup.

$$V_{HV} - V_t = I_d R_d \text{ and } \mathrm{V_t} = \mathrm{I_t}\left(\frac{1}{\mathrm{R_e}} + \frac{1}{\mathrm{R_t}}\right)^{-1} \tag{C.1}$$

[1] National Instruments Corporation, 11500 N Mopac Expwy, Austin, TX 78759-3504

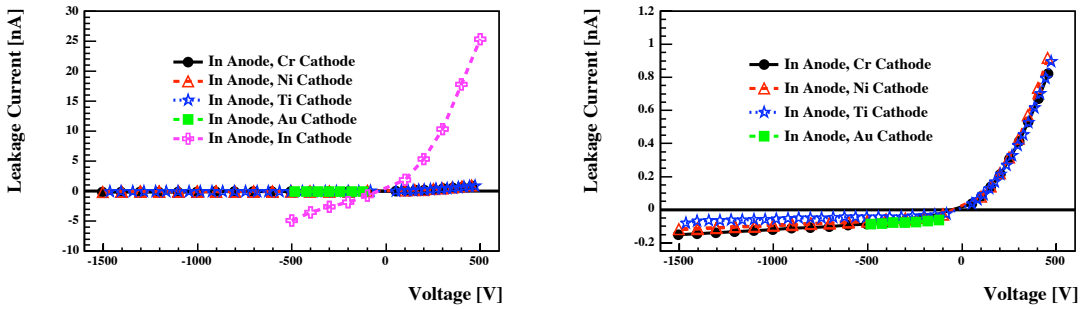

FIGURE C.1: I-V curves taken with the apparatus described in this appendix for two Orbotech CZT detectors with pixellated In anodes and different cathode materials. All contact materials show a diode like curve. The graph on the right is a zoomed in portion of the left showing the finer details of the I-V curves without the In-In contacted detector (Figure from Jung et al. (2005)).

Where V_{HV} is the high voltage, V_t is the voltage across the test resistor, R_d is the detector resistance, I_t is the current across the test resistor, and R_e is the electrometer resistance. We also know that the current flowing through the pixel is the same as that flowing through the test resistance $I_d = I_t$. So if we measure V_t and V_{HV} and know R_t and R_e then

$$R_d = \frac{V_{HV} - V_t}{I_t} \text{ and } \mathrm{I_t} = \mathrm{V_t}\left(\frac{1}{\mathrm{R_e}} + \frac{1}{\mathrm{R_t}}\right) \tag{C.2}$$

This setup depends on $R_e \gg R_t$ (so that very little current flows through the mixer/electrometer path) and in practice $R_e \sim 100^{12}$ and $R_t \sim 100 \times 10^6$ so that

$$I_t = \frac{V_t}{I_t} \tag{C.3}$$

TABLE C.1: I-V Equipment.

Part	Model
Mixer	Maxim DG408
Electrometer	Keithley 614
DAQ	NI PCI-6024E
HV	Bertan 205A-03R
R_t	100 $M\Omega$ 1%

thus,

$$R_d = \frac{V_{HV} - V_t}{V_t} R_t \tag{C.4}$$

which are all measurable or known. Table C.1 gives the models of the equipment used and Table C.2 gives the pin out and ins for all the equipment.

C.1.2 LabView Program

Figure C.3 shows an image of the front panel of the LabView program. Figures C.4,C.5 and C.6 show block diagrams of the LabView program (the block diagram is the main program of the graphical programming language, LabView). All of the possible diagrams are not shown here but the main logic of the data acquisition system can be understood from these diagrams. The full program can be accessed by looking at the full block diagram within the program itself on the PC attached to the I-V setup.

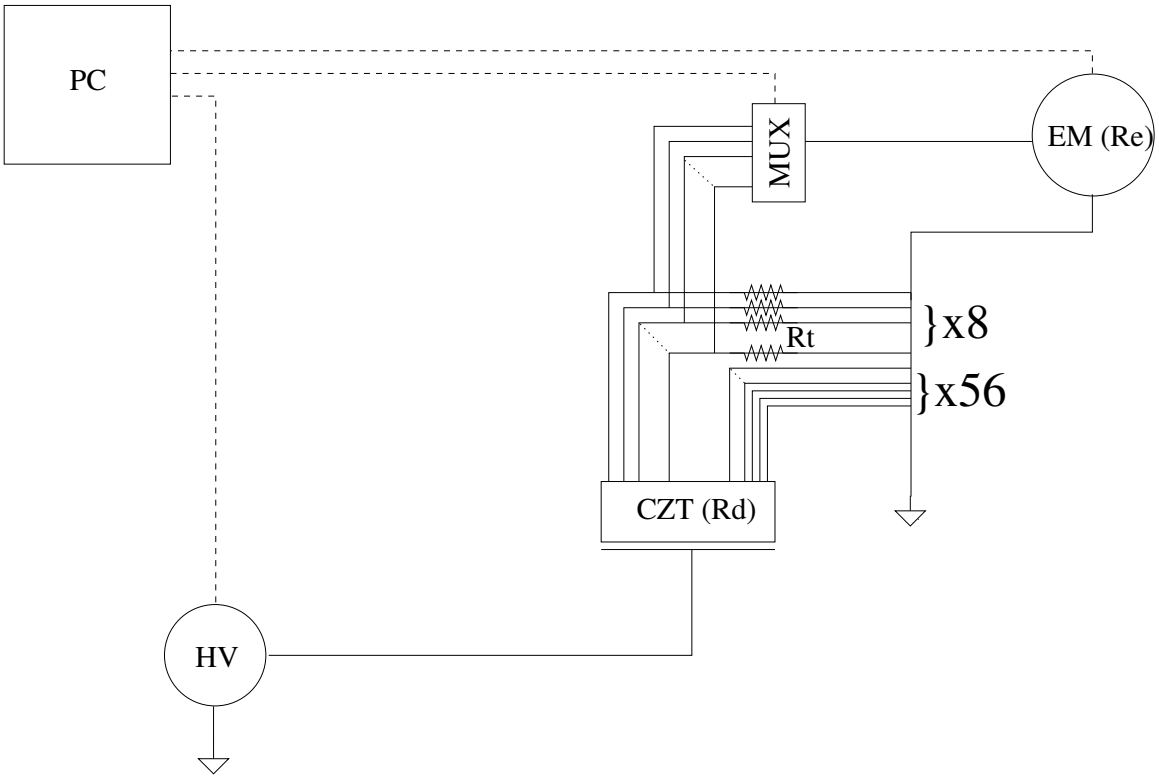

FIGURE C.2: Schematic of the I-V measurement. High Voltage (HV) is applied to the CZT (with a bulk resistance R_d) on the cathode side. Eight of the pixels are grounded through a test resistance (R_t) and attached through a mixer (MUX) to an electrometer (EM, with impedance R_e). The other 56 pixels are directly grounded. The mixer, electrometer and high voltage source are all connected to a PC through a NI DAQ card (NI6024). This setup allows the PC to control which (of the eight connected through the mixer) pixel is connected to the electrometer which measures the voltage drop across the test resistor to determine the current flowing through that pixel.

Table C.2: I-V Connections.

DAQ Pin	DAQ Name	Equipment Pin	Equipment Name
52	P0.0	MUX A0	Mixer Logic 0
17	P0.1	MUX A1	Mixer Logic 1
49	P0.2	MUX A2	Mixer Logic 2
47	P0.3	MUX EN	Mixer Logic EN
68	AI 0	HV-E	0-5V Monitoring
34	AI 8	HV-C	Ground
22	AO 0	HV-B	0-5V Programming
33	AI 1	E-	Electrometer Negative Monitoring
66	AI 9	E+	Electrometer Positive Monitoring

To perform a standard measurement follow the instructions below:

- Load a detector into the current measurement apparatus being careful about how much force you apply.
- Turn on the Electrometer, HV (must be set to rear control) and all power supplies.
- Run the LabView program from the PC
- Visually inspect the values found on the Front Panel (C.3). Do they make sense?
- Set the HV to a significant but low value ($\sim 100V$) and inspect the values again. Do they still make sense?
- Set the HV to 0 and switch to a different channel and raise the voltage again and again visually inspect the values.
- If any of these tests fail, something is wrong and we need to troubleshoot a bit.
- Now, run a constant voltage test to see what the settling time is. Once you do this, set the settling time for the standard run.
- Do a standard run - if you set the top voltage too high, the current might go beyond the set-point and the run will cancel. If this happens, just set it lower and run it again.

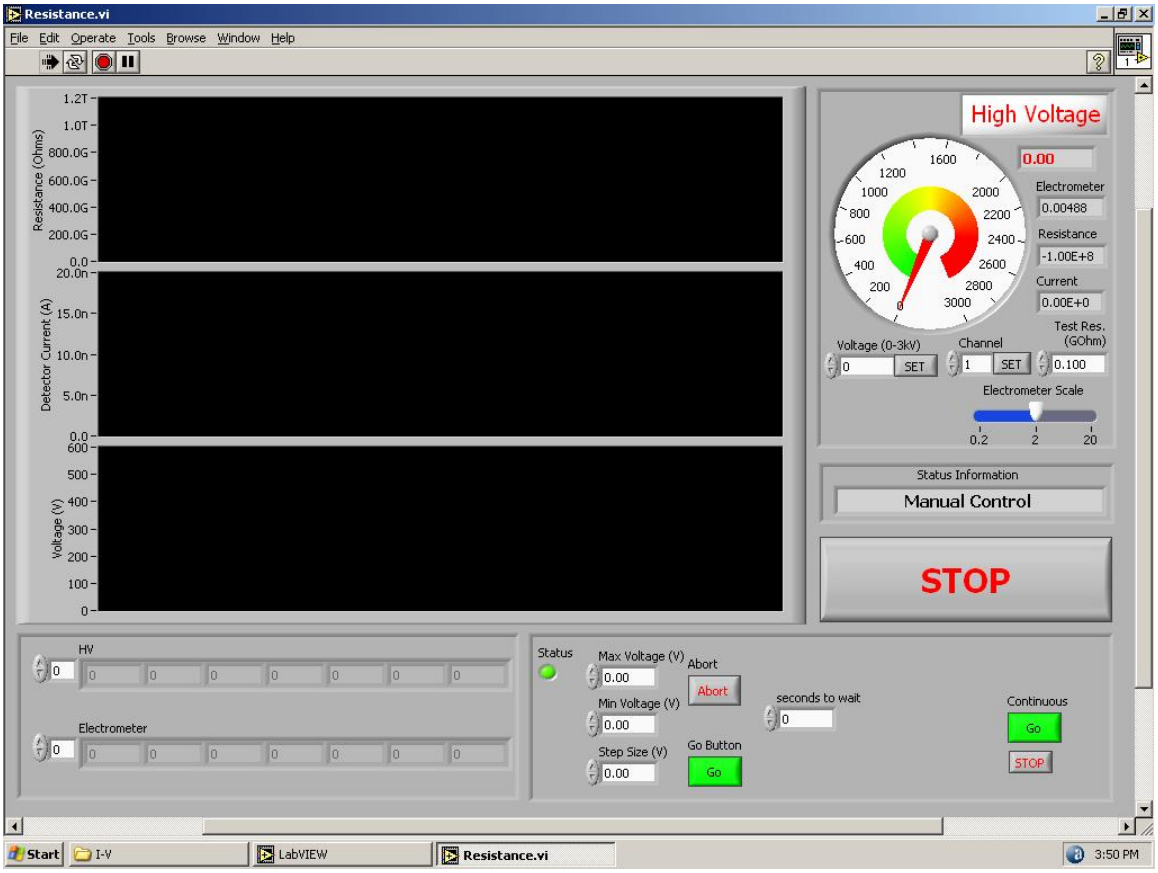

FIGURE C.3: Figure of the front panel of the LabView interface to IV measurement. There are three plots shown in the top left (in order from top to bottom: Resistance, Current and Voltage). The bottom right of the screen are the actual raw data values plotted. The top right of the screen includes a voltage meter as well as the current values of the electrometer, resistance and current. There are also controls to set the voltage and multiplexer channel as well as the test resistance used. The electrometer scale is also set here (it needs to match the scale chosen on the front panel of the electrometer. Below this panel is a status information window and a Stop button that should be used to quit the program. The bottom right of the screen are the run controls. On the left of this panel is the standard loop run (run the voltage up and down and loop over the channels) on the right is a continuous run option.

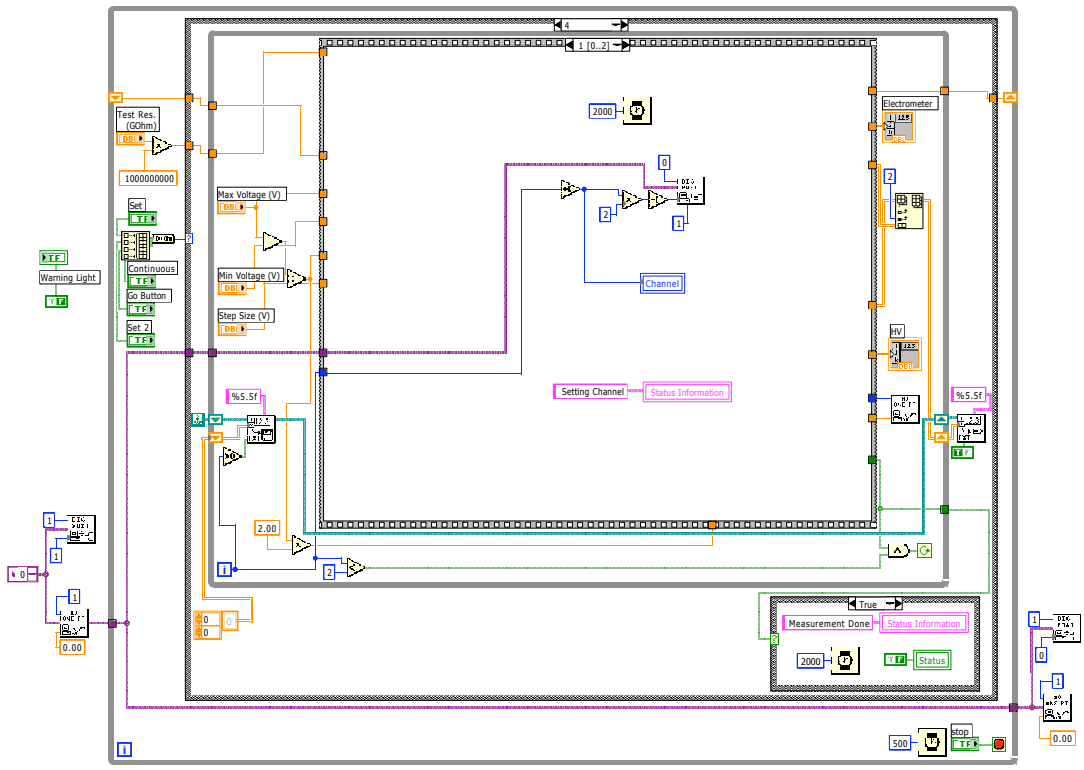

FIGURE C.4: Figure of the full LabView block diagram for controlling the automated IV measurements showing the overall logic of the program. The DAQ is setup on the bottom left by setting the digital and analog output ports. Following this, the main loop is initialized which is continued until the user hits the stop button on the main user screen (the logic for this is on the bottom right of this figure). Within this overall loop, there is a state machine which is chosen by the boolean array on the middle left of the image. This state machine specifies the task to be run and in this image is set up to run task '4' (see the number at the top of the screen) which is the main multiplexing measurement. Within this specific state there is an overall loop that continues until the measurement completes and within this there is a sequence structure (the 'film' like frame) that handles the data acquisition. See Figure C.6 for a description of this data acquisition sequence. For a description of all of the states see Figure C.5.

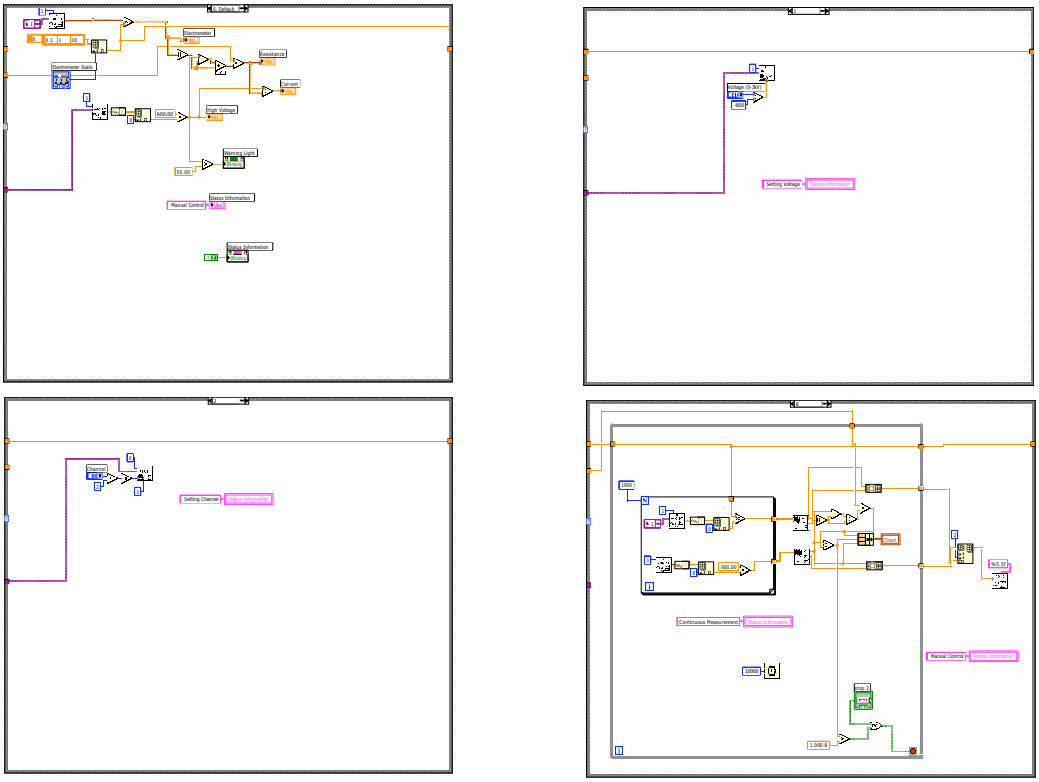

FIGURE C.5: Other possible states of the program. Clockwise from the top left: the default state which just reads the current values from the electrometer and high voltage supply, state 2 which is used to set the high voltage, state 1 which is used to set the digital channel (mixer channel), and the last state which performs a continuous measurement.

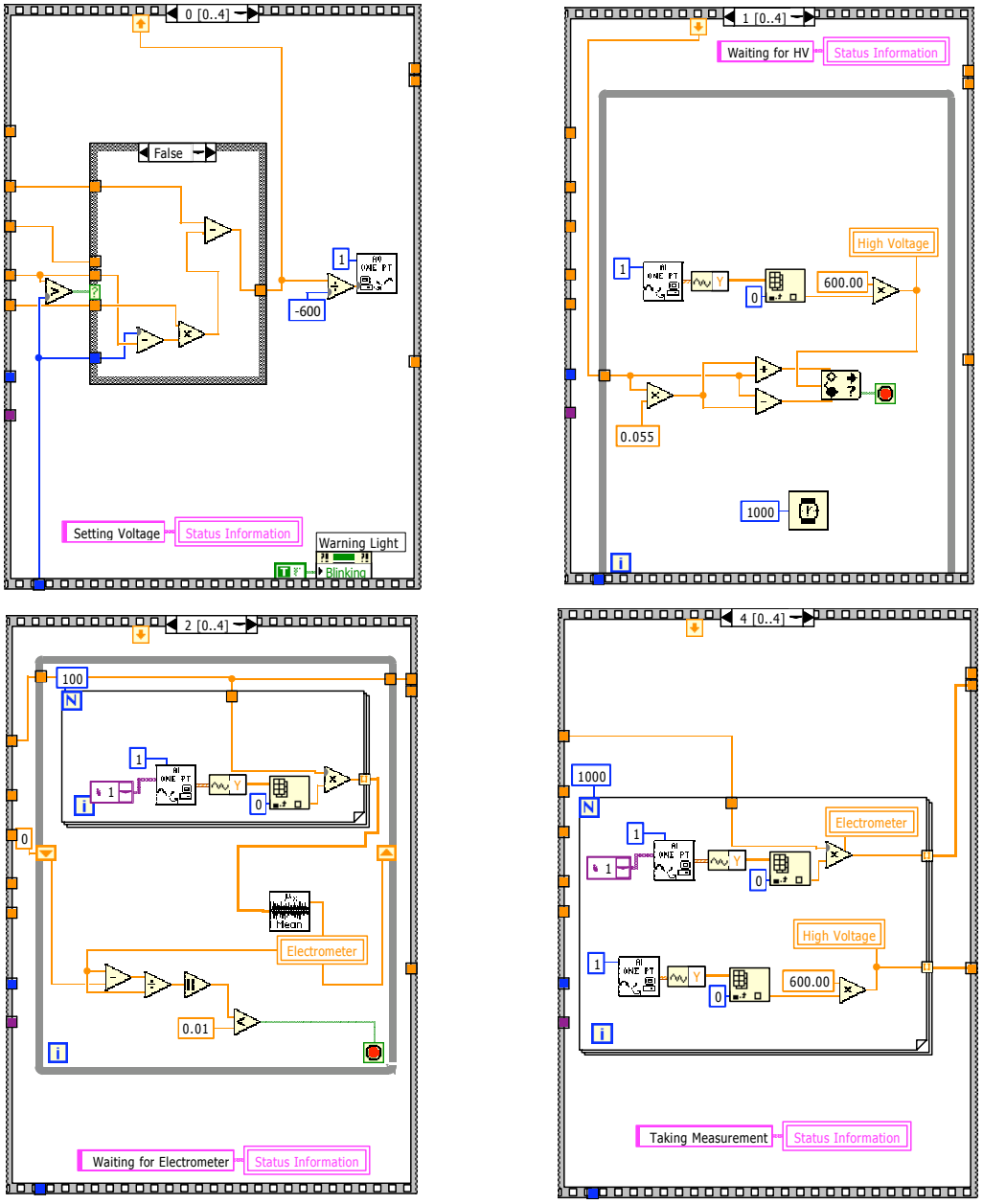

FIGURE C.6: The data acquisition sequence is shown in this figure. Step 0 sets the high voltage then step 1 waits for the voltage to settle to a good value. Step 2 waits for the electrometer to settle before taking a measurement. Step 3 (not shown here) waits for a user specified amount and then step 4 takes a measurement by averaging over 1000 samples.

C.2 Four Point Measurements

A four point measurement allows for the determination of the surface current through the detector. By passing a current through two points on the surface and measuring the voltage drop at a point between those points we can determine the surface resistivity. We assume that the current flows through a very thin layer along the surface of the detector. For a very thin layer (thickness $t << s$), we get current rings instead of spheres. Therefore, the expression for the area is $A = 2\pi xt$. The derivation is as follows:

$$R = \int_{x_1}^{x_2} \rho \frac{dx}{2\pi xt} = \int_{s}^{2s} \frac{\rho}{2\pi t} \frac{dx}{x} = \frac{\rho}{2\pi t} \ln x|_{s}^{2s} = \frac{\rho}{2\pi t} \ln 2 \tag{C.5}$$

Consequently, for $R = V/2I$, the sheet resistivity for a thin sheet is:

$$\rho = \frac{\pi t}{\ln 2} \left(\frac{V}{I} \right) \tag{C.6}$$

Note that this expression is independent of the probe spacing s. Furthermore, this latter expression is frequently used for characterization of semiconductor layers, such as a diffused N+ region in a p-type substrate. In general, the sheet resistivity $R_s = \rho/t$ can be expressed as

$$R_s = k \frac{V}{I} \tag{C.7}$$

where the factor k is a geometric factor. IN the case of a semi-infinite sheet, k = 4.53, which is just $\pi / \ln 2$ from the derivation. The factor k will be different for

non-ideal samples.

C.2.1 Apparatus

Figure C.7 shows a schematic of the apparatus. The physical setup involves a mount for a single detector with for adjustable probes mounted around it. Position each of the probes at a point on the detector (taking care not to touch them together). The two middle probes are connected to a BNC connector and this should be connected to the electrometer (or some other voltage measuring device). The outer two probes should be connected through a $1M\Omega$ test resistor to a voltage supply (such as a Keithly 0 - 10V). A multimeter can be used to measure the voltage drop across this resistor. At this point, set the voltage supply at varying voltages recording the voltage drop across the resistor and the electrometer (the inner two probes touching the detector). The current through the detector can then be calculated using the formulas above.

C.2.2 Data

I performed a preliminary 4-point measurement on D0 (gold on both sides). Table C.3 shows the results.

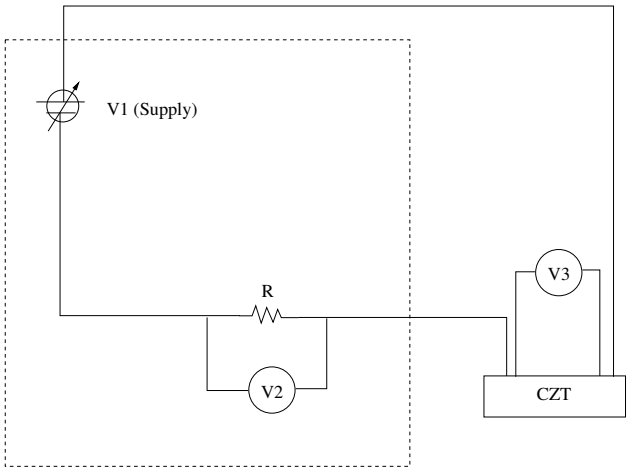

FIGURE C.7: Schematic of the 4-point measurement. V_1 is the supply voltage, R is a $1M\Omega 1\%$ resistor used in conjunction with the V_2 measurement to simulate a current supply (shown within the dashed box). The current is supplied through the outer contacts on the CZT and I measure the voltage drop at V_3.

TABLE C.3: Data for a single 4-point measurement on D0 (with gold contacts). All values are in volts and the various measurement names are from Figure C.7.

V_1	$V_2(\pm 0.001)$	$V_3(\pm 0.001)$	$I = V_2/R(nA)$
0.5	0.003	0.03	3 ± 0.03
1.0	0.004	0.06	4 ± 0.04
1.5	0.006	0.09	6 ± 0.06
2.0	0.009	0.13	9 ± 0.09
2.5	0.010	0.16	10 ± 0.1
3.0	0.012	0.20	12 ± 0.2

Continued on next page.

V_1	$V_2(\pm 0.001)$	$V_3(\pm 0.001)$	$I = V_2/R(nA)$
3.5	0.015	0.24	15 ± 0.15
4.0	0.021	0.26	21 ± 0.21
4.5	0.026	0.29	26 ± 0.26
5.0	0.033	0.32	33 ± 0.33
5.5	0.038	0.35	38 ± 0.38
6.0	0.042	0.38	42 ± 0.42
6.5	0.045	0.42	45 ± 0.45
7.0	0.046	0.45	46 ± 0.46
7.5	0.052	0.48	52 ± 0.52
8.0	0.055	0.51	55 ± 0.55
8.5	0.058	0.54	58 ± 0.58
9.0	0.062	0.57	62 ± 0.62
9.5	0.065	0.60	65 ± 0.65
10.0	0.070	0.64	70 ± 0.70

C.2.3 Analysis

From the schematic, you can see that the current through the outer probes is $I = V_2/R$ and in this case, R is a 1% $1M\Omega$ resistor. Now, from Equation C.7 you can get R_s by plotting V_3 versus I and fit a line to the slope and from that, calculate

TABLE C.4: Error Analysis (fitted line with parameters r(x) = a*x + b).

degrees of freedom (ndf)	18
rms of residuals(stdfit)=sqrt(WSSR/ndf)	0.0261646
variance of residuals(reduced chisquare)=WSSR/ndf	0.000684586

TABLE C.5: Results (fitted line with parameters r(x) = a*x + b).

a (Volts/nA)	$0.00826403 \pm 0.0002664(3.223\%)$
b (Volts)	$0.0583285 \pm 0.01069(18.33\%)$

the sheet resistance. Figure C.8 shows the fit and the data while the results of the fit are given in Tables C.4 and C.5. The slope comes out to be 0.00826 V/nA which translates to $8.26 \times 10^6 \Omega$ and if I use $k = 4.53$ that means that the final value I get is $R_s = 37.4 M\Omega$ which is on the order of what we expect.

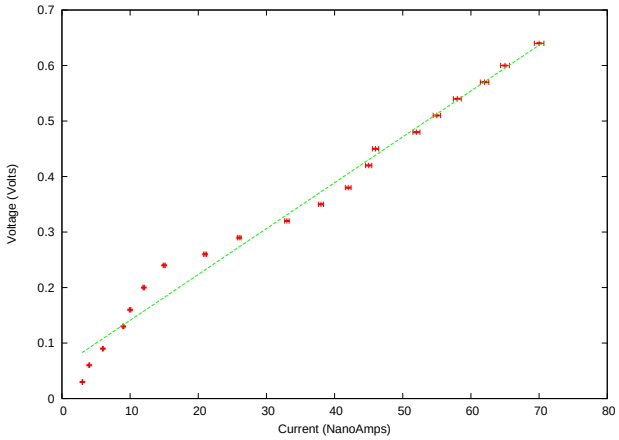

FIGURE C.8: The fit and the data.

Appendix D

Data Acquisition System for X-ray Spectroscopy

D.1 Apparatus

This system is setup to acquire a spectrum from a CZT detector using a fast 500Mhz oscilloscope readout for three pixels as well as the cathode so as to provide timing information. Sixteen more pixels are read out using an ASIC and only provide amplitude information. A schematic of the system is shown in Figure D.1 and an image of the detector mounted as well as the pixel layout is shown in Figure D.2.

D.2 Code

```
#include <iostream>
#include <errno.h>
```

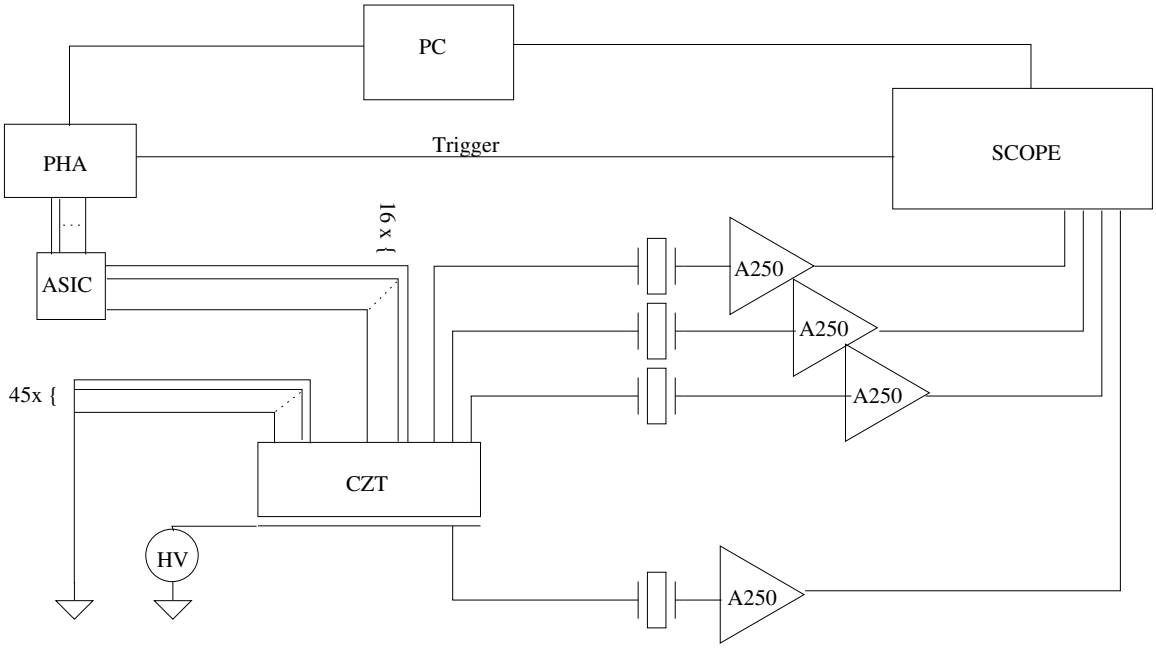

FIGURE D.1: DAQ Schematic.

```
//Root Stuff
#include <TTree.h>
#include <TFile.h>

//Hardware Stuff
extern "C" {
#include "LeCroySocket.h"
#include "pdio.h"
#include "pdrelay.h"
#include "pdpha.h"
}

#include "ProgressBar.h"
#include "data_structure.h"

#define PORT            1861
#define HOST            "scope"

#define WAVESIZE        30000
#define FLUSH           1000

#define SEND            's'
```

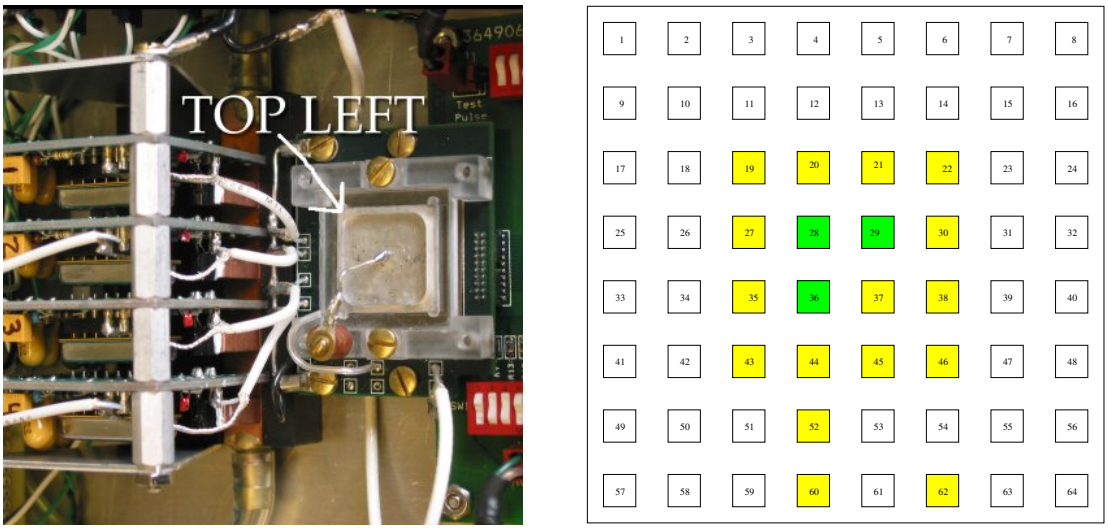

FIGURE D.2: Pixel Layout. The panel on the left shows a CZT detector mounted in the DAQ system pointing out the location of the top left corner. Using this location as a reference, the right panel diagrams the pixel mapping. The pixels in green are connected to the A250 and through the oscilloscope while the pixels in yellow are connected to the ASIC and through the PHA boards. Pixels in white are grounded.

```
#define READ            'r'
#define QUIT            'Q'
#define MENU            'm'
#define GRABPHA         'p'
#define GRABSCP         'g'
#define GRABN           'n'
#define CHANNELS        'c'
#define HEADER          'h'
#define SETTHRESH       't'
#define KWICK           'k'
#define DEBUG           'd'

using namespace std;

static int ScopeSend(char*, int);
static void ScopeRead(void);
static void grabP(int mesg, int disp, int type);
static void quit(void);
static void grabS(int);
static void grabN(int);
static void SetChannels();
static double GetTrigTime(void);
```

```
static void GetHeader(void);
static float GetOption(int,char*);
static void WaitCoin(void);
static void SetThresholds(int);
static void SetTriggerScope(void);
static void InitTrees(TTree**, TTree**, TTree**);
static void DeleteTrees(TTree**, TTree**, TTree**);
static void WriteTrees(char*,TTree*,TTree**, TTree*, TTree*);
static void QuickSetChans(int);
static void DebugSwitch();

int sockfd;                                /*Socket Reference*/

static int Npha;
static int Nwds;
static unsigned short *D;                  /* data buffer */
static short Intdac = 200;                 /* internal dac value */

bool debug = false;

#define NLINES 3
char *progmenu[NLINES];
#define LINELEN 80

static void initmenu(void);
static void menu(void);

char *menuformat[] = {
    "%c=send   %c=grabpha  %c=channels              %c=menu  ",
    "%c=read   %c=grabScp  %c=grabN                 %c=header",
    "%c=setTh  %c=kwick    %c=debug                 %c=quit  ",
};

int waveforms[4][WAVESIZE];
Int_t pha[16];
DATA data;
HEAD head;

int main(int argc, char *argv[])
{

    int i;
    char key;
    char buffer[256];
```

```
//Connect to the Scope
sockfd = connectToScope(PORT,HOST);
if (sockfd < 0)
    cout << "ERROR opening socket" << endl;
else
    cout << "Connected to scope." << endl;
if(errno){
    fprintf(stderr, "Can't initialize board (%s)\n", strerror(errno));
}
//Initialize PHA Boards
printf("Initializing Board...\n");
pdpha_init();
if(errno){
    fprintf(stderr, "Can't initialize board (%s)\n", strerror(errno));
}
else{
    printf("Initialized.\n");
    Npha = pdpha_get_nphadet();
    Nwds = 6 + (Npha * 12);
    D = (short unsigned int*)malloc(Nwds * sizeof(short));
    if (D == NULL) {
        fprintf(stderr, "%s: can't malloc\n", argv[0]);
        exit(1);
    }

    SetThresholds(1);



}

initmenu();

while(1) {
    cout << ": ";
    cin >> key;
    switch(key) {
    case SEND:
        ScopeSend(buffer,1);
        break;
    case READ:
        ScopeRead();
        break;
    case QUIT:
```

```
            quit();
            break;
        case MENU:
            initmenu();
            break;
        case GRABPHA:
            grabP(1,1,0);
            break;
        case GRABSCP:
            grabS(1);
            break;
        case GRABN:
            grabN(0);
            break;
        case CHANNELS:
            SetChannels();
            break;
        case HEADER:
            GetHeader();
            break;
        case SETTHRESH:
            SetThresholds(0);
            break;
        case KWICK:
            QuickSetChans(0);
            break;
        case DEBUG:
            DebugSwitch();
            break;
        default:
            if(key != '\r' && key != '\n')
                printf("␣%c?␣What␣is␣that?\n\r", key);
            break;
        }
    }
}

static void SetChannels(){

    int i;

    for(i=0;i<5;i++){
        if(i==4)
            cout << "Disable/Enable␣PHA's␣(1/0)?" << endl;
```

```
        else
            cout << "Disable/Enable Channel " << i+1 << " (1/0)?" << endl;
        cin >> head.channels[i];
    }

    for(i=0;i<5;i++){
        if(i==4)
            cout << "Trigger from PHA's (1/0)?" << endl;
        else
            cout << "Trigger from Channel " << i+1 << " (1/0)?" << endl;
        cin >> head.triggers[i];
        if(head.triggers[i])
            data.trigger = i;
    }

}

static void QuickSetChans(int choice){

    int i;

    //A250 Set Up
    if(choice == 0){
        for(i=0;i<4;i++)
            head.channels[i] = true;
        head.channels[4] = false;
        for(i=1;i<4;i++)
            head.triggers[i] = true;
        head.triggers[0] = false;
        head.triggers[4] = false;

        cout << "Set up channels for A250 (Triggering on 2,3,4)." << endl;
    }

}




static int ScopeSend(char* buffer,int type){

    string str;
    int n;
```

```
    if(type == 1){
        cout << "Please enter the message: \r" << endl;
        fgets(buffer,255,stdin);
        fgets(buffer,255,stdin);
if(debug){
        cout << "ScopeSend: '" << buffer << "'" << endl;
}
        n = sendToScope(buffer,sockfd);
    }
    else{
if(debug){
        cout << "ScopeSend: '" << buffer << "'" << endl;
}
        n = sendToScope(buffer,sockfd);
        if (n < 0)
            cout << "ERROR writing to socket ('" << buffer << "')" << endl;
    }

    return n;

}


static void ScopeRead(void){

  char buffer[256];
  int waveform[WAVESIZE];
  int n,i;

  bzero(buffer,256);
  n = readFromScope(buffer,sockfd,waveform);
  if (n < 0)
    cout << "ERROR reading from socket" << endl;
  printf("%s\n",buffer);
  if (n > 256){
   cout << "Recieved Waveform of size " << n << endl;
  }

}

static void grabS(int type){

  char buffer[256];
  int n,i;
```

```
  bool first = true;

 //Read the channels
  for(i=0;i<4;i++){
      if(head.channels[i]){
          if(type == 1 && first){
              cout << "Enter a trigger Channel" << endl;
              cin >> data.trigger;
              SetTriggerScope();
              ScopeSend("arm;wait",0);
          }
          sprintf(buffer,"c%i:wf? dat1",i+1);
          ScopeSend(buffer,0);
          bzero(buffer,256);
          n = readFromScope(buffer,sockfd,&waveforms[i][0]);
          if (n < 0)
              cout << "ERROR reading from socket" << endl;
          //Ok, don't know why this works, but it does.  Sometimes you have to
          //ask again nicely.
          if(buffer[11]!='#')
              n = readFromScope(buffer,sockfd,&waveforms[i][0]);
if(debug){
          printf("%s\n",buffer);
          if (n > 256)
              cout << "Recieved Waveform of size " << n << endl;
}
          first = false;

      }
  }
}


static void grabN(int number){

    int i,j,k;
    char filename[256];
    char temp[256];

    cout << "Enter a file root (eg: test): " << endl;
    cin >> filename;

    // create the trees
    TTree *wave[4];
```

```
TTree *pha_T;
TTree *event;
TTree *header = new TTree("header","Run_Information");
ProgressBar *progress;

// set up the TTrees
header->Branch("head", &head, "vertical_gain[4]/F:vertical_offset[4]/F:horiz_interval[4]/F:horiz_offset[4]/F:po
InitTrees(wave,&pha_T,&event);

// set up the looping
if(number<1){
    cout << "Enter the number of events (0 to exit):" << endl;
    cin >> number;
}
//ProgressBar progress(number,"Chan 0");

cout << "Enter in the Cathode Channel." << endl;
cin >> head.cathode;


//Fill the header
GetHeader();
header->Fill();

//Grab the data and fill the waveforms
k=0;
for(data.trigger=0;data.trigger<5;data.trigger++){
    if(head.triggers[data.trigger]){
        sprintf(temp,"Chan %i",data.trigger+1);
        if(!debug)
            progress = new ProgressBar(number,temp);
        SetTriggerScope();
        for(i=0;i<number;i++){
            data.eventnum = i+k;
            WaitCoin();
            grabS(0);
            if(head.channels[4]){
                grabP(1,0,1);
                pha_T->Fill();
            }
            for(j=0;j<4;j++){
                if(head.channels[j]){
                    if(debug){
                        cout << "Filling Waveform " << j << endl;
```

```
                    }
                    wave[j]->Fill();
                }
            }
            data.time = GetTrigTime();
            event->Fill();
            //Save to disc ever so often for safety!
            if(data.eventnum%FLUSH == 0 && data.eventnum > 0){
                WriteTrees(filename,header,wave,pha_T,event);
                DeleteTrees(wave,&pha_T,&event);
                InitTrees(wave,&pha_T,&event);
            }
            if(!debug)
                progress->print(i);
            if(debug)
                cout << "Event " << i+k << endl;
        }
        k+=number;
        if(!debug){
            progress->printClear();
            delete progress;
        }
        cout << "Finished with channel " << data.trigger+1 << " (" << i << " events)." << endl;
    }
}

    WriteTrees(filename,header,wave,pha_T,event);
    DeleteTrees(wave,&pha_T,&event);
}

static void
grabP(int mesg, int disp, int type)
{
  static long evtno = 0L;
  int i,j;
  unsigned long *lp;
  int ret;
  unsigned short *sp;

  if(type==0){

      data.trigger = 4;
      SetTriggerScope();
```

```
    if (mesg) {
        printf(
               " Waiting for coincidence. Press any key to stop wait.\n\r");
    }

    WaitCoin();

    if (disp) {
        printf(" \n\rEvtno: %ld\n\r", evtno);
    }
}

sp = D;
*sp++ = 0x90AF;                 /* evt signature */
*sp++ = Npha; /* no. of pha boards */

lp = (unsigned long *)sp;
*lp++ = evtno++;       /* evt number */
*lp++ = clock();       /* tick count */

sp = (unsigned short *)lp;
for (i=0; i<Npha; i++) {
  if (i == 14) {
    printf(" PRESS ANY KEY TO CONTINUE");
    //GETKEY;
    printf(" \n\r");
  }

  if (pdpha_rd_pha_bd(i, sp) == (unsigned short *)0) {
    printf(" grab1: pdpha_rd_pha_bd() error (%d)\n", i);
    return;
  }

  if (disp) {
    printf(
           "%04u %04u %04u %04u %04u %04u %04u %04u ",
           sp[0], sp[1], sp[2], sp[3], sp[4], sp[5], sp[6], sp[7]);
  }

  for(j=0;j<8;j++){
      pha[i*8+j] = sp[j];
  }

  sp += 8;
```

```
    *sp++ = pdpha_rd_sum_scaler(i);      /* S scaler */
    *sp++ = pdpha_rd_sel_scaler(i);      /* SC scaler */
    *sp++ = pdpha_get_sel_chan(i);       /* SC channel */
    *sp++ = pdpha_pha_addr_map(i);       /* board address */

    if (disp) {
      printf("␣CD=%05u␣SC=%05u␣chan=%01d␣bd=%d\n\r",
             sp[-4], sp[-3], sp[-2], sp[-1]);
    }
  }

  pdio_coin_clr();

}


static void
initmenu(void)
{
        int i;
        for(i=0; i<NLINES; i++)
                if((progmenu[i] = (char*)malloc(strlen(menuformat[i] + 1))) == NULL)
                        fprintf(stderr, "Bad␣malloc␣(%s)\n", strerror(errno));

        sprintf(progmenu[0], menuformat[0], SEND, GRABPHA, CHANNELS, MENU);
        sprintf(progmenu[1], menuformat[1], READ, GRABSCP, GRABN, HEADER);
        sprintf(progmenu[2], menuformat[2], SETTHRESH,KWICK,DEBUG,QUIT);
        menu();
}

static void
menu(void)
{
    int i;
    for (i=0; i<NLINES; i++) {
        printf("␣%s\n", progmenu[i]);
    }
 }

static void
quit(void)
{
    char key;
```

```
    cout << "Are you sure you want to quit? (y/N):";
    cin >> key;
    if(key == 'y'){
        cout << "I'm Quittting Now." << endl;
        exit(0);
    }
    else{
        cout << "Not really quitting." << endl;
        return;
    }

}


double
GetTrigTime(void){

    int dummywave[WAVESIZE];
    char buffer[256];
    string temp,trig_time;
    double h,m,s,seconds;
    int n,t1,t2,i;

    bzero(buffer,255);
    if(data.trigger<4)
        sprintf(buffer,"c%i:insp? 'trigger_time'",data.trigger+1);
    else
        sprintf(buffer,"c1:insp? 'trigger_time'");
    ScopeSend(buffer,0);
    bzero(buffer,255);
    n = readFromScope(buffer,sockfd,dummywave);
    if (n < 0)
        cout << "ERROR reading from socket (" << buffer << ")" << endl;
    if(debug){
        cout << buffer;
    }
    i=0;
    //Ok, don't know why this works, but it does.  Sometimes you have to
    //ask again nicely.
    while(buffer[i]!='T' && i<256)
        i++;
    if(buffer[i]!='T'){
        if(debug){
            cout << "Asking for time again." << endl;
```

```
        }
        bzero(buffer,255);
        if(data.trigger<4)
            sprintf(buffer,"c%i:insp? 'trigger_time'",data.trigger+1);
        else
            sprintf(buffer,"c1:insp? 'trigger_time'");
        ScopeSend(buffer,0);
        bzero(buffer,255);
        n = readFromScope(buffer,sockfd,dummywave);
    }

    temp = &buffer[8];
    t1 = temp.find_first_of("=",0);
    t1 = temp.find_first_of("=",t1+1);
    t2 = temp.find_first_of("\"",t1);

    trig_time = temp.substr(t1+2,t2-t1-2);
    h = atof(trig_time.substr(0,2).c_str());
    m = atof(trig_time.substr(3,2).c_str());
    s = atof(trig_time.substr(6,10).c_str());
    seconds = s+60*m+60*60*h;

    if(debug){
        cout << "Trig Time: "<< h <<":"<< m <<":"<< s << " ("<< seconds <<" s total)" << endl;
    }

    return seconds;

}

void
GetHeader(void){

    int i;

    for(i=0;i<4;i++){
        head.points_per_screen[i] = (int)GetOption(i+1,"PNTS_PER_SCREEN");
        head.vertical_gain[i] = GetOption(i+1,"VERTICAL_GAIN");
        head.vertical_offset[i] = GetOption(i+1,"vertical_offset");
        head.horiz_interval[i] = GetOption(i+1,"horiz_interval");
        head.horiz_offset[i] = GetOption(i+1,"horiz_offset");
    }

}
```

```
float
GetOption(int channel, char* option){

    int dummywave[WAVESIZE];
    char buffer[256];
    float value;
    int n;

    bzero(buffer,255);
    sprintf(buffer,"c%i:insp? '%s'",channel,option);
    ScopeSend(buffer,0);
    bzero(buffer,255);
    n = readFromScope(buffer,sockfd,dummywave);
    value = atof(&buffer[30]);
    if(debug){
        cout << buffer;
        cout << value << endl;
    }

    return value;

}

void
SetThresholds(int init){

    int i;

    if(!init){
        cout << "Enter a threshold value." << endl;
        cin >> Intdac;
    }

    printf("Setting thresholds...\n");
    for (i=0; i < Npha; i++) {
        pdpha_set_thr_dac(i, Intdac);
    }
    printf("Thresholds set.\n");
}

void
WaitCoin(void){
```

```
    int i =0;
    int sum=0;

    if(head.channels[4]){

        if(debug){
            printf("Clearing PHA coincidnece.\n");
        }

        pdio_coin_clr();

        if(debug){
            printf("..Cleared.\n");
        }
        for(i=0;i<4;i++)
            sum+=head.channels[i];
        if(sum>0){
            ScopeSend("arm",0);
            //You need to wait a bit after sending the arm command to the scope
            //Otherwise, the pd coin might get there before the scope is ready
            usleep(500000);
        }

        if(debug){
            printf("PHA Waiting...\n");
        }

        while (!pdio_coincidence()) {
            //if (kbhit()) {
            //getch();
            //printf(" Cancelled\n\r");
            //return;
            //}
        }
    }
    else
        ScopeSend("arm;wait",0);

}

void
SetTriggerScope(void){
```

```
    char buffer[256];
    int n;

    //Stop the scope This could probably be done elsewhere to make
    //the aquisition faster.
    ScopeSend("stop",0);

    //Set the trigger This could probably be done elsewhere to make
    //the aquisition faster.
    //Set up the scope to trigger externally if we're triggering off
    //of the PHA's
    bzero(buffer,256);
    if(data.trigger<4)
        sprintf(buffer,"trse edge,sr,c%i",data.trigger+1);
    else
        sprintf(buffer,"trse edge,sr,ex");
    ScopeSend(buffer,0);

}

void
InitTrees(TTree **wave, TTree **pha_T, TTree **event){

    //This function initializes the trees for data acquisition.

    int i;
    char temp1[50],temp2[50];

    if(debug){
        cout << "Initiallizing event Tree." << endl;
    }
    *event = new TTree("data","Event Information");
    (*event)->Branch("data",&data,"eventnum/I:time/D:trigger/I");

    for(i=0;i<4;i++){
        if(head.channels[i]) {
            if(debug){
                cout << "Initiallizing wave Tree number: " << i << endl;
            }
            sprintf(temp1,"chan%i",i+1);
            wave[i] = new TTree(temp1,temp1);
            sprintf(temp2,"waveform[%i]/I",WAVESIZE);
            wave[i]->Branch(temp1,&waveforms[i][0],temp2);
        }
```

```
    }
    if(head.channels[4]){
        if(debug){
            cout << "Initiallizing pha Tree." << endl;
        }
        *pha_T = new TTree("pha","PHA Events");
        (*pha_T)->Branch("pha",pha,"pha[16]/I");
    }

}

void
DeleteTrees(TTree **wave, TTree **pha_T, TTree **event){

    //This function deletes the trees for data acquisition.

    int i;

    delete (*event);

    for(i=0;i<4;i++){
        if(head.channels[i]) {
            wave[i]->Delete();
        }
    }
    if(head.channels[4]){
        delete (*pha_T);
    }

}

void
WriteTrees(char *filename, TTree *header, TTree **wave, TTree *pha_T, TTree *event){

    //This function writes the data to file

    int j;
    char outfile[256];

    sprintf(outfile,"%s-%i.root",filename,data.eventnum);
    if(debug){
        cout << "Flushing data to disc." << endl;
        cout << "Filename: " << outfile << endl;
    }
```

```
    TFile *f = new TFile(outfile,"RECREATE");
    if(debug){
        cout << "Writing trees..." << endl;
    }
    //f->Flush();
    header->Write();
    if(head.channels[4])
        pha_T->Write();
    event->Write();
    for(j=0;j<4;j++){
        if(head.channels[j]){
            wave[j]->Write();
        }
    }
    if(debug){
        cout << "Done." << endl;
        cout << "Closing file..."<<endl;
    }
    f->Write();
    f->Close();
    if(debug){
        cout << "Done." << endl;
    }
    delete f;

}

void
DebugSwitch(){

    debug = !debug;

    cout << "Debug is now " << debug << endl;

}
```

Appendix E

Upper Limit Calculation

The following code computes an upper limit based on the Baysian method of Helene (1983). This specific algorithm was used for the upper limit calculation presented in this thesis. Note that it depends on the GNU Scientific Library (GSL) for the gaussian statistics computations.

E.1 Code

```
#include <gsl/gsl_cdf.h>

double upper(double, double, double);

int main(int argc, char *argv[]){

  double sigma
  double sigma_in_percent;
  double flux,error;

  cin >> sigma;
  cin >> flux;
  cin >> error;
```

```
  //Calculate the sigma wanted in percent.
  sigma_in_percent       = 1 - 1.*gsl_cdf_gaussian_Q(sigma,1);

  //Compute the upper limit based on the flux and error
  cout << upper(flux,error,sigma_in_percent) << endl;

}

double upper(double mu,double error,double sigma){

    double upper;
    double total_pos;
    double confidence_pos;

    //The percentage of the gaussian above 0 is computed here
    //The 'Q' cdf is the cdf from some value x up to inf.  If
    //you have a gaussian centered on mu, then to find the pos
    //percentage, you sum from -mu up to inf.
    total_pos = gsl_cdf_gaussian_Q(-mu,error);

    //The percentage of the gausian within the confidence interval
    //above zero is
    confidence_pos = (1.0 - sigma)*total_pos;

    //The 'Qinv' function finds the value of x for a given percentage
    //We're looking for the 90% of the positive percentage and upper
    //then gives the value of the excess at the 90% of the positive
    //percentage -> ie. the 90% confidence limit.
    upper = gsl_cdf_gaussian_Qinv(confidence_pos,error);

    //You have to add 'mu' to the upper limit because the zero level
    //is different from the standard gaussian and the one we want to
    //calculate
    upper+=mu;

    return upper;

}
```

Bibliography

Aharonian, F., Akhperjanian, A. G., Aye, K.-M., Bazer-Bachi, A. R., Beilicke, M., Benbow, W., Berge, D., Berghaus, P., Bernlöhr, K., Bolz, O., Boisson, C., Borgmeier, C., Breitling, F., Brown, A. M., Bussons Gordo, J., Chadwick, P. M., Chitnis, V. R., Chounet, L.-M., Cornils, R., Costamante, L., Degrange, B., Djannati-Ataï, A., O'C. Drury, L., Ergin, T., Espigat, P., Feinstein, F., Fleury, P., Fontaine, G., Funk, S., Gallant, Y., Giebels, B., Gillessen, S., Goret, P., Guy, J., Hadjichristidis, C., Hauser, M., Heinzelmann, G., Henri, G., Hermann, G., Hinton, J. A., Hofmann, W., Holleran, M., Horns, D., de Jager, O. C., Jung, I., Khélifi, B., Komin, N., Konopelko, A., Latham, I. J., Le Gallou, R., Lemoine, M., Lemière, A., Leroy, N., Lohse, T., Marcowith, A., Masterson, C., McComb, T. J. L., de Naurois, M., Nolan, S. J., Noutsos, A., Orford, K. J., Osborne, J. L., Ouchrif, M., Panter, M., Pelletier, G., Pita, S., Pohl, M., Pühlhofer, G., Punch, M., Raubenheimer, B. C., Raue, M., Raux, J., Rayner, S. M., Redondo, I., Reimer, A., Reimer, O., Ripken, J., Rivoal, M., Rob, L., Rolland, L., Rowell, G., Sahakian, V., Saugé, L., Schlenker, S., Schlickeiser, R., Schuster, C., Schwanke, U., Siewert, M., Sol, H., Steenkamp, R., Stegmann, C., Tavernet, J.-P., Théoret, C. G., Tluczykont, M., van der Walt, D. J., Vasileiadis, G., Vincent, P., Visser, B., Völk, H. J., and Wagner, S. J.: 2004, *Astronomy and Astrophysics* **425**, L13

Aharonian, F., Akhperjanian, A. G., Bazer-Bachi, A. R., Beilicke, M., Benbow, W., Berge, D., Bernlöhr, K., Boisson, C., Bolz, O., Borrel, V., Braun, I., Breitling, F., Brown, A. M., Chadwick, P. M., Chounet, L.-M., Cornils, R., Costamante, L., Degrange, B., Dickinson, H. J., Djannati-Ataï, A., O'C. Drury, L., Dubus, G., Emmanoulopoulos, D., Espigat, P., Feinstein, F., Fontaine, G., Fuchs, Y., Funk, S., Gallant, Y. A., Giebels, B., Gillessen, S., Glicenstein, J. F., Goret, P., Hadjichristidis, C., Hauser, M., Heinzelmann, G., Henri, G., Hermann, G., Hinton, J. A., Hofmann, W., Holleran, M., Horns, D., Jacholkowska, A., de Jager, O. C., Khélifi, B., Komin, N., Konopelko, A., Latham, I. J., Le Gallou, R., Lemière, A., Lemoine-Goumard, M., Leroy, N., Lohse, T., Martin, J. M., Martineau-Huynh, O., Marcowith, A., Masterson, C., McComb, T. J. L., de Naurois, M., Nolan, S. J., Noutsos, A., Orford, K. J., Osborne, J. L., Ouchrif, M., Panter, M., Pelletier, G., Pita, S., Pühlhofer, G., Punch, M., Raubenheimer, B. C., Raue, M., Raux, J., Rayner, S. M., Reimer, A., Reimer, O., Ripken, J., Rob, L., Rolland, L., Rowell, G., Sahakian, V., Saugé, L., Schlenker, S., Schlickeiser, R., Schuster, C., Schwanke, U., Siewert, M., Sol, H., Spangler, D., Steenkamp, R., Stegmann, C., Tavernet, J.-

P., Terrier, R., Théoret, C. G., Tluczykont, M., Vasileiadis, G., Venter, C., Vincent, P., Völk, H. J., and Wagner, S. J.: 2005, *Resolving the Extragalactic Background Light with gamma-ray spectra from distant blazars*, astro-ph/0508073

Aharonian, F. A.: 2005, *American Astronomical Society Meeting Abstracts* **207**,

Alexandreas, D. E., Berley, D., Biller, S., Dion, G. M., Goodman, J. A., Haines, T. J., Hoffman, C. M., Horch, E., Lu, X.-Q., Sinnis, C., Yodh, G. B., and Zhang, W.: 1993, *Nuclear Instruments and Methods in Physics Research A* **328**, 570

Barret, H. H., Eskin, J. D., and Barber, H. B.: 1995, *Phys. Rev. Let.* **75**, 156

Benbow et. al., W.: 2005, in F. A. Aharonian, H. J. Völk, and D. Horns (eds.), *AIP Conf. Proc. 745: High Energy Gamma-Ray Astronomy*, pp 611–616

Bergström, L., Ullio, P., and Buckley, J. H.: 1998, *Astroparticle Physics* **9**, 137

Blanton, E. L.: 2004, in T. Reiprich, J. Kempner, and N. Soker (eds.), *The Riddle of Cooling Flows in Galaxies and Clusters of galaxies*, pp 181–+

Blanton, E. L., Sarazin, C. L., McNamara, B. R., and Wise, M. W.: 2001, *ApJL* **558**, L15

Blasi, P. and Colafrancesco, S.: 1999, *Astroparticle Physics* **12**, 169

Boehringer, H., Voges, W., Fabian, A. C., Edge, A. C., and Neumann, D. M.: 1993, *MNRAS* **264**, L25

Böhringer, H., Matsushita, K., Churazov, E., Ikebe, Y., and Chen, Y.: 2002, *Astronomy and Astrophysics* **382**, 804

Bolotnikov, A. E., Chen, C. M. H., Cook, W. R., Harrison, F. A., Kuvvetli, I., and Schindler, S. M.: 2002, *IEEE Transactions on Nuclear Science* **49**, 1941

Bolotnikov, A. E., Cook, W. R., Harrison, F. A., Wong, A.-S., Schindler, S. M., and Eichelberger, A. C.: 1999, *Nuclear Instruments and Methods in Physics Research A* **432**, 326

Bowyer, S. and Berghöfer, T. W.: 1998, *ApJ* **506**, 502

Buckley, J. H., Akerlof, C. W., Carter-Lewis, D. A., Catanese, M., Cawley, M. F., Connaughton, V., Fegan, D. J., Finley, J. P., Gaidos, J. A., Hillas, A. M., Krennrich, F., Lamb, R. C., Lessard, R. W., McEnery, J. E., Mohanty, G., Quinn, J., Rodgers, A. J., Rose, H. J., Rovero, A. C., Schubnell, M. S., Sembroski, G., Srinivasan, R., Weekes, T. C., and Zweerink, J.: 1998, *Astronomy and Astrophysics* **329**, 639

Byram, E. T., Chubb, T. A., and Friedman, H.: 1966, *Science* **152**, 66

Carilli, C. L., Perley, R. A., and Harris, D. E.: 1994, *MNRAS* **270**, 173

Churazov, E., Forman, W., Jones, C., and Böhringer, H.: 2003, *ApJ* **590**, 225

Churazov, E., Sunyaev, R., Forman, W., and Böhringer, H.: 2002, *MNRAS* **332**, 729

Clarke, T. E., Blanton, E. L., and Sarazin, C. L.: 2004, *ApJ* **616**, 178

Colafrancesco, S.: 2001, in *AIP Conf. Proc. 587: Gamma 2001: Gamma-Ray Astrophysics*, p. 427

Colina, L. and Perez-Fournon, I.: 1990, *ApJS* **72**, 41

Condon, J. J., Cotton, W. D., Greisen, E. W., Yin, Q. F., Perley, R. A., Taylor, G. B., and Broderick, J. J.: 1998, *AJ* **115**, 1693

Conselice, C. J., Gallagher, J. S., and Wyse, R. F. G.: 2001, *AJ* **122**, 2281

Davies, J. M. and Cotton, E. S.: 1957, *Solar Energy Sci. and Eng.* 1

Donahue, M. and Voit, G. M.: 2004, in J. S. Mulchaey, A. Dressler, and A. Oemler (eds.), *Clusters of Galaxies: Probes of Cosmological Structure and Galaxy Evolution*, pp 143–+

Donahue, M. E., Voit, G. M., and Cavagnolo, K.: 2004, *American Astronomical Society Meeting Abstracts* 205

Edge, A. C. and Stewart, G. C.: 1991, *MNRAS* **252**, 414

Edge, D. O., Shakeshaft, J. R., McAdam, W. B., Baldwin, J. E., and Archer, S.: 1959, *Mem. R. Astron. Soc.* **68**, 37

Enßlin, T. A. and Biermann, P. L.: 1998, *Astronomy and Astrophysics* **330**, 90

Fabian, A. C.: 1994, *Ann. Rev. Astron. Astrophys.* **32**, 277

Fabian, A. C., Hu, E. M., Cowie, L. L., and Grindlay, J.: 1981, *ApJ* **248**, 47

Fabian, A. C., Sanders, J. S., Taylor, G. B., Allen, S. W., Crawford, C. S., Johnstone, R. M., and Iwasawa, K.: 2006, *MNRAS* **366**, 417

Fabian, A. C., Zarneck, J. C., Culhane, J. L., Hawkins, F. J., Peacock, A., Pounds, K. A., and Parkinson, J. H.: 1974, *ApJL* **189**, L59+

Falcone, A. D., Badran, H. M., Blaylock, G., Bond, I. H., Boyle, P. J., Bradbury, S. M., Buckley, J. H., Byrum, K., Carter-Lewis, D. A., Celik, O., Cogan, P., Cui, W., Daniel, M., de La Calle Perez, I., Dowkontt, P., Duke, C., Fegan, D. J., Fegan, S. J., Finley, J. P., Fortson, L. F., Gammell, S., Gibbs, K., Gillanders, G. H., Grube, J., Guiterrez, K. J., Hall, J., Hanna, D., Holder, J., Horan, D., Hughes, S.,

Humensky, T. B., Jung, I., Kenny, G. E., Kertzman, M., Kieda, D., Kildea, J., Knapp, J., Kosack, K., Krawczynski, H., Krennrich, F., Lang, M. J., Le Bohec, S., Linton, E., Lloyd-Evans, J., Mendoza, D., Merriman, A., Milovanovic, A., Moriarty, P., Nagai, T., Olevitch, M., Ong, R. A., Pallassini, R., Perkins, J., Petry, D., Pizlo, F., Pohl, M., Power-Mooney, B., Quinn, J., Quinn, M., Ragan, K., Rebillot, P., Reynolds, P. T., Rose, H. J., Schroedter, M., Sembroski, G. H., Swordy, S. P., Syson, A., Valcarcel, L., Vassiliev, V. V., Wagner, R., Wakely, S. P., Walker, G., Weekes, T. C., White, R. J., Zweerink, J., and VERITAS Collaboration: 2005, in F. A. Aharonian, H. J. Völk, and D. Horns (eds.), *AIP Conf. Proc. 745: High Energy Gamma-Ray Astronomy*, pp 633–638

Fegan, S. J., Badran, H. M., Bond, I. H., Boyle, P. J., Bradbury, S. M., Buckley, J. H., Carter-Lewis, D. A., Catanese, M., Celik, O., Cui, W., Daniel, M., D'Vali, M., de la Calle Perez, I., Duke, C., Falcone, A., Fegan, D. J., Finley, J. P., Fortson, L. F., Gaidos, J. A., Gammell, S., Gibbs, K., Gillanders, G. H., Grube, J., Hall, J., Hall, T. A., Hanna, D., Hillas, A. M., Holder, J., Horan, D., Jarvis, A., Jordan, M., Kenny, G. E., Kertzman, M., Kieda, D., Kildea, J., Knapp, J., Kosack, K., Krawczynski, H., Krennrich, F., Lang, M. J., Le Bohec, S., Lessard, R. W., Linton, E., Lloyd-Evans, J., Milovanovic, A., McEnery, J., Moriarty, P., Mukherjee, R., Muller, D., Nagai, T., Nolan, S., Ong, R. A., Pallassini, R., Petry, D., Power-Mooney, B., Quinn, J., Quinn, M., Ragan, K., Rebillot, P., Reynolds, P. T., Rose, H. J., Schroedter, M., Sembroski, G. H., Swordy, S. P., Syson, A., Vassiliev, V. V., Wakely, S. P., Walker, G., Weekes, T. C., and Zweerink, J.: 2005, *ApJ* **624**, 638

Feretti, L.: 2003, in *Texas in Tuscany. XXI Symposium on Relativistic Astrophysics*, pp 209–220

Feretti, L., Giovannini, G., Klein, U., Mack, K.-H., Sijbring, L. G., and Zech, G.: 1998, *Astronomy and Astrophysics* **331**, 475

Finley, J. P., Krennrich, F., Badran, H. M., Bond, I. H., Bradbury, S. M., Buckley, J. H., Carter-Lewis, D. A., Catanese, M., Cui, W., Dunlea, S., Das, D., de la Calle Perez, I., Fegan, D. J., Fegan, S. J., Gaidos, J. A., Gibbs, K., Gillanders, G. H., Hall, T. A., Hillas, A. M., Holder, J., Horan, D., Jordan, M., Kertzman, M., Kieda, D., Kildea, J., Knapp, J., Kosack, K., Lang, M. J., LeBohec, S., McKernan, B., Moriarty, P., Müller, D., Ong, R., Pallassini, R., Petry, D., Quinn, J., Reay, N. W., Reynolds, P. T., Rose, H. J., Sembroski, G. H., Sidwell, R., Stanton, N., Swordy, S. P., Vassiliev, V. V., Wakely, S. P., and Weekes, T. C.: 2001, in *International Cosmic Ray Conference*, p. 2827

Fusco-Femiano, R., dal Fiume, D., Feretti, L., Giovannini, G., Grandi, P., Matt, G., Molendi, S., and Santangelo, A.: 1999, *ApJL* **513**, L21

Fusco-Femiano, R., Orlandini, M., Brunetti, G., Feretti, L., Giovannini, G., Grandi, P., and Setti, G.: 2004, *ApJL* **602**, L73

Garmire, G. P., Bautz, M. W., Ford, P. G., Nousek, J. A., and Ricker, G. R.: 2003, in *X-Ray and Gamma-Ray Telescopes and Instruments for Astronomy. Edited by Joachim E. Truemper, Harvey D. Tananbaum. Proceedings of the SPIE, Volume 4851, pp. 28-44 (2003).*, pp 28–44

Giovannini, G. and Feretti, L.: 2000, *New Astronomy* **5**, 335

Giovannini, G., Feretti, L., Venturi, T., Kim, K.-T., and Kronberg, P. P.: 1993, *ApJ* **406**, 399

Giovannini, G., Tordi, M., and Feretti, L.: 1999, *New Astronomy* **4**, 141

Girardi, M., Giuricin, G., Mardirossian, F., Mezzetti, M., and Boschin, W.: 1998, *ApJ* **505**, 74

Grindlay, J. E.: 2005, *New Astronomy Review* **49**, 436

Gruber, D. and Rephaeli, Y.: 2002, *ApJ* **565**, 877

Gutierrez, K. and Krawczynski, H.: 2005, *ApJ* **619**, 161

Harris, D. E., Krawczynski, H., and Taylor, G. B.: 2002, *ApJ* **578**, 60

Harrison et. al., F.: 2004, *AAS/High Energy Astrophysics Division* **8**,

He, Z., Li, W., Knoll, G. F., Wehe, D. K., Berry, J., and Stahle, C. M.: 1999, *Nuclear Instruments and Methods in Physics Research A* **422**, 173

Heinz, S., Choi, Y.-Y., Reynolds, C. S., and Begelman, M. C.: 2002, *ApJL* **569**, L79

Helene, O.: 1983, *Nuclear Instruments and Methods in Physics Research* **212**, 319

Hillas, A. M.: 1985, in *International Cosmic Ray Conference*, pp 445–448

Hong, J., Bellm, E. C., Grindlay, J. E., and Narita, T.: 2004, in *X-Ray and Gamma-Ray Instrumentation for Astronomy XIII. Edited by Flanagan, Kathryn A.; Siegmund, Oswald H. W. Proceedings of the SPIE, Volume 5165, pp. 54-62 (2004).*, pp 54–62

Horns, D.: 2005, *Physics Letters B* **607**, 225

Hornschemeier, A. E., White, N. E., and Tananbaum, H.: 2005, in R. Smith (ed.), *AIP Conf. Proc. 774: X-ray Diagnostics of Astrophysical Plasmas: Theory, Experiment, and Observation*, pp 383–389

Jackson, J. D.: 1999, *Classical Electrodynamics*, John Wiley and Sons, Inc, New York, 3rd edition

Jansen, F., Lumb, D., Altieri, B., Clavel, J., Ehle, M., Erd, C., Gabriel, C., Guainazzi, M., Gondoin, P., Much, R., Munoz, R., Santos, M., Schartel, N., Texier, D., and Vacanti, G.: 2001, *Astronomy and Astrophysics* **365**, L1

Jelley, J. V.: 1958, *Cerenkov Radiation and its Applications*, Pergamon Press, New York, NY

Jones, C. and Forman, W.: 1984, *ApJ* **276**, 38

Jung, I., Groza, M., Perkins, J., Krawczynski, H., and Burger, A.: 2005, in R. B. James, L. A. Franks, and A. Burger (eds.), *Advances in Metrology for X-Ray and EUV Optics. Edited by Assoufid, Lahsen; Takacs, Peter Z.; Taylor, John S. Proceedings of the SPIE, Volume 5922, pp. 1-8 (2005).*, pp 1–8

Kalemci, E. and Matteson, J. L.: 2002, *Nuclear Instruments and Methods in Physics Research A* **478**, 527

Kang, H. and Jones, T. W.: 2005, *ApJ* **620**, 44

Kawasaki, W. and Totani, T.: 2002, *ApJ* **576**, 679

Kempner, J. C. and Sarazin, C. L.: 2001, *ApJ* **548**, 639

King, I. R.: 1972, *ApJL* **174**, L123

Kneiske, T. M., Mannheim, K., and Hartmann, D. H.: 2002, *Astronomy and Astrophysics* **386**, 1

Kosack, K.: 2005, *Ph.D. thesis*, Washington University in St. Louis

Kosack, K., Badran, H. M., Bond, I. H., Boyle, P. J., Bradbury, S. M., Buckley, J. H., Carter-Lewis, D. A., Celik, O., Connaughton, V., Cui, W., Daniel, M., D'Vali, M., de la Calle Perez, I., Duke, C., Falcone, A., Fegan, D. J., Fegan, S. J., Finley, J. P., Fortson, L. F., Gaidos, J. A., Gammell, S., Gibbs, K., Gillanders, G. H., Grube, J., Gutierrez, K., Hall, J., Hall, T. A., Hanna, D., Hillas, A. M., Holder, J., Horan, D., Jarvis, A., Jordan, M., Kenny, G. E., Kertzman, M., Kieda, D., Kildea, J., Knapp, J., Krawczynski, H., Krennrich, F., Lang, M. J., Le Bohec, S., Linton, E., Lloyd-Evans, J., Milovanovic, A., McEnery, J., Moriarty, P., Muller, D., Nagai, T., Nolan, S., Ong, R. A., Pallassini, R., Petry, D., Power-Mooney, B., Quinn, J., Quinn, M., Ragan, K., Rebillot, P., Reynolds, P. T., Rose, H. J., Schroedter, M., Sembroski, G. H., Swordy, S. P., Syson, A., Vassiliev, V. V., Wakely, S. P., Walker, G., Weekes, T. C., and Zweerink, J.: 2004, *ApJL* **608**, L97

Krawczynski, H.: 2002, *ApJL* **569**, L27

Krawczynski, H., Harris, D. E., Grossman, R., Lane, W., Kassim, N., and Willis, A. G.: 2003, *MNRAS* **345**, 1255

Leahy, D. A. and Yin, D.: 2000, *MNRAS* **313**, 617

Li, T.-P. and Ma, Y.-Q.: 1983, *ApJ* **272**, 317

Li, W., He, Z., Knoll, G. F., Wehe, D. K., and Berry, J. E.: 2001, *Nuclear Instruments and Methods in Physics Research A* **458**, 518

Lieu, R., Ip, W.-H., Axford, W. I., and Bonamente, M.: 1999, *ApJL* **510**, L25

Lieu, R., Mittaz, J. P. D., Bowyer, S., Breen, J. O., Lockman, F. J., Murphy, E. M., and Hwang, C.-Y.: 1996, *Science* **274**, 1335

Longair, M. S.: 1992, *High Energy Astrophysics*, Vol. 1, Cambridge University Press, Cambridge, 2nd edition

Malkan, M. A. and Stecker, F. W.: 2001, *ApJ* **555**, 641

Mannheim, K., Hartmann, D., and Funk, B.: 1996, *ApJ* **467**, 532

Markevitch, M., Forman, W. R., Sarazin, C. L., and Vikhlinin, A.: 1998, *ApJ* **503**, 77

Mason, K. O., Breeveld, A., Much, R., Carter, M., Cordova, F. A., Cropper, M. S., Fordham, J., Huckle, H., Ho, C., Kawakami, H., Kennea, J., Kennedy, T., Mittaz, J., Pandel, D., Priedhorsky, W. C., Sasseen, T., Shirey, R., Smith, P., and Vreux, J.-M.: 2001, *Astronomy and Astrophysics* **365**, L36

Matteson, J. L., Pelling, M. R., and Skelton, R. T.: 2003, in *Proc. SPIE Vol. 4784, p. 1-13, X-Ray and Gamma-Ray Detectors and Applications IV, Ralph B. James; Larry A. Franks; Arnold Burger; Edwin M. Westbrook; Roger D. Durst; Eds.*, pp 1–13

McNamara, B. R., Nulsen, P. E. J., Wise, M. W., Rafferty, D. A., Carilli, C., Sarazin, C. L., and Blanton, E. L.: 2005, *Nature* **433**, 45

McNamara, B. R. and O'Connell, R. W.: 1989, *AJ* **98**, 2018

McNamara, B. R., Wise, M., Nulsen, P. E. J., David, L. P., Sarazin, C. L., Bautz, M., Markevitch, M., Vikhlinin, A., Forman, W. R., Jones, C., and Harris, D. E.: 2000, *ApJL* **534**, L135

McNamara, B. R., Wise, M. W., Nulsen, P. E. J., David, L. P., Carilli, C. L., Sarazin, C. L., O'Dea, C. P., Houck, J., Donahue, M., Baum, S., Voit, M., O'Connell, R. W., and Koekemoer, A.: 2001, *ApJL* **562**, L149

Miley, G. K. and Perola, G. C.: 1975, *Astronomy and Astrophysics* **45**, 223

Mitchell, R. J., Culhane, J. L., Davison, P. J. N., and Ives, J. C.: 1976, *MNRAS* **175**, 29P

Mushotzky, R. F. and Smith, B. W.: 1980, *Highlights of Astronomy* **5**, 735

Narita, T., Bloser, P. F., Grindlay, J. E., and Jenkins, J. A.: 2000, in *Proc. SPIE Vol. 4141, p. 89-96, Hard X-Ray, Gamma-Ray, and Neutron Detector Physics II, Ralph B. James; Richard C. Schirato; Eds.*, pp 89–96

Narita, T., Bloser, P. F., Grindlay, J. E., Jenkins, J. A., and Yao, H. W.: 1999, in *Proc. SPIE Vol. 3768, p. 55-65, Hard X-Ray, Gamma-Ray, and Neutron Detector Physics, Ralph B. James; Richard C. Schirato; Eds.*, pp 55–65

Nevalainen, J., Oosterbroek, T., Bonamente, M., and Colafrancesco, S.: 2004, *ApJ* **608**, 166

Pacholczyk, A. G.: 1970, *Radio astrophysics. Nonthermal processes in galactic and extragalactic sources*, Series of Books in Astronomy and Astrophysics, San Francisco: Freeman, 1970

Pedlar, A., Ghataure, H. S., Davies, R. D., Harrison, B. A., Perley, R., Crane, P. C., and Unger, S. W.: 1990, *MNRAS* **246**, 477

Perkins, J.-S., Badran, H. M., Blaylock, G., Bradbury, S. M., Cogan, P., Chow, Y. C. K., Cui, W., Daniel, M. K., Falcone, A. D., Fegan, S. J., Finley, J. P., Fortin, P., Fortson, L. F., Gillanders, G. H., Gutierrez, K. J., Grube, J., Hall, J., Hanna, D., Holder, J., Horan, D., Hughes, S. B., Kenny, G. E., Kertzman, M., Kieda, D. B., Kildea, J., Kosack, K., Krawczynski, H., Krennrich, F., Lang, M. J., LeBohec, S., Maier, G., Moriarty, P., Ong, R. A., Pohl, M., Ragan, K., Rebillot, P. F., Sembroski, G. H., Steele, D., Swordy, S. P., Valcarcel, L., Vassiliev, V. V., Wakely, S. P., Weekes, T. C., and Williams, D. A.: 2006, *ApJ*, astro-ph/0602258

Peterson, J. R., Kahn, S. M., Paerels, F. B. S., Kaastra, J. S., Tamura, T., Bleeker, J. A. M., Ferrigno, C., and Jernigan, J. G.: 2004, in T. Reiprich, J. Kempner, and N. Soker (eds.), *The Riddle of Cooling Flows in Galaxies and Clusters of galaxies*, pp 119–+

Pfrommer, C. and Enßlin, T. A.: 2004, *Astronomy and Astrophysics* **413**, 17

Pigot, C., Belsole, E., Bennie, P. J., Ferrando, P., Sauvageot, J. L., Marty, P. B., and Sembay, S.: 1999, in *Proc. SPIE Vol. 3765, p. 251-264, EUV, X-Ray, and Gamma-Ray Instrumentation for Astronomy X, Oswald H. Siegmund; Kathryn A. Flanagan; Eds.*, pp 251–264

Primack, J. R., Bullock, J. S., and Somerville, R. S.: 2005, in F. A. Aharonian, H. J. Völk, and D. Horns (eds.), *AIP Conf. Proc. 745: High Energy Gamma-Ray Astronomy*, pp 23–33

Punch, M. and Fegan, D. J.: 1991, in *AIP Conf. Proc. 220: High Energy Gamma Ray Astronomy*, pp 321–328

Read, A. M. and Ponman, T. J.: 2003, *Astronomy and Astrophysics* **409**, 395

Reimer, O., Pohl, M., Sreekumar, P., and Mattox, J. R.: 2003, *ApJ* **588**, 155

Rephaeli, Y.: 1977, *ApJ* **218**, 323

Rephaeli, Y., Gruber, D., and Blanco, P.: 1999, *ApJL* **511**, L21

Reynolds, P. T., Akerlof, C. W., Cawley, M. F., Chantell, M., Fegan, D. J., Hillas, A. M., Lamb, R. C., Lang, M. J., Lawrence, M. A., Lewis, D. A., Macomb, D., Meyer, D. I., Mohanty, G., O'Flaherty, K. S., Punch, M., Schubnell, M. S., Vacanti, G., Weekes, T. C., and Whitaker, T.: 1993, *ApJ* **404**, 206

Ritz, S., Grindlay, J., Meegan, C., Michelson, P. F., and GLAST Mission Team: 2005, *American Astronomical Society Meeting Abstracts* **207**,

Romney, J. D., Walker, R. C., Kellermann, K. I., Vermeulen, R. C., and Dhawan, V.: 1996, in *IAU Symp. 175: Extragalactic Radio Sources*, pp 27–+

Rosati, P., Tozzi, P., Ettori, S., Mainieri, V., Demarco, R., Stanford, S. A., Lidman, C., Nonino, M., Borgani, S., Della Ceca, R., Eisenhardt, P., Holden, B. P., and Norman, C.: 2004, *AJ* **127**, 230

Ryu, D., Kang, H., Hallman, E., and Jones, T. W.: 2003, *ApJ* **593**, 599

Sanders, J. S., Fabian, A. C., and Dunn, R. J. H.: 2005, *MNRAS* **360**, 133

Sarazin, C.: 1988, *X-Ray Emission from Clusters of Galaxies*, Cambridge University Press, Cambridge

Sarazin, C. L., O'Connell, R. W., and McNamara, B. R.: 1992, *ApJL* **389**, L59

Scharf, C. A. and Mukherjee, R.: 2002, *ApJ* **580**, 154

Seyfert, C. K.: 1943, *ApJ* **97**, 28

Shakeshaft, J. R., Ryle, M., Baldwin, J. E., Elsmore, B., and Thomson, J. H.: 1955, *Mem. R. Astron. Soc.* **67**, 106

Struble, M. F. and Rood, H. J.: 1999, *ApJS* **125**, 35

Strüder, L., Briel, U., Dennerl, K., Hartmann, R., Kendziorra, E., Meidinger, N., Pfeffermann, E., Reppin, C., Aschenbach, B., Bornemann, W., Bräuninger, H., Burkert, W., Elender, M., Freyberg, M., Haberl, F., Hartner, G., Heuschmann, F., Hippmann, H., Kastelic, E., Kemmer, S., Kettenring, G., Kink, W., Krause, N., Müller, S., Oppitz, A., Pietsch, W., Popp, M., Predehl, P., Read, A., Stephan, K. H., Stötter, D., Trümper, J., Holl, P., Kemmer, J., Soltau, H., Stötter, R., Weber, U., Weichert, U., von Zanthier, C., Carathanassis, D., Lutz, G., Richter,

R. H., Solc, P., Böttcher, H., Kuster, M., Staubert, R., Abbey, A., Holland, A., Turner, M., Balasini, M., Bignami, G. F., La Palombara, N., Villa, G., Buttler, W., Gianini, F., Lainé, R., Lumb, D., and Dhez, P.: 2001, *Astronomy and Astrophysics* **365**, L18

Taylor, G. B., Barton, E. J., and Ge, J.: 1994, *AJ* **107**, 1942

Taylor, G. B., Govoni, F., Allen, S. W., and Fabian, A. C.: 2001, *MNRAS* **326**, 2

Trifoglio, M., Gianotti, F., Stephen, J. B., Balasini, M., Hochedez, J.-F. E., Chiappetti, L., Glukhov, R. A., Hainaut, O., Jourdain, E., La Palombara, N., Marty, P. B., Moreno, T., and Musso, C.: 1998, in *Proc. SPIE Vol. 3445, p. 558-565, EUV, X-Ray, and Gamma-Ray Instrumentation for Astronomy IX, Oswald H. Siegmund; Mark A. Gummin; Eds.*, pp 558–565

Tsuchiya, K., Enomoto, R., Ksenofontov, L. T., Mori, M., Naito, T., Asahara, A., Bicknell, G. V., Clay, R. W., Doi, Y., Edwards, P. G., Gunji, S., Hara, S., Hara, T., Hattori, T., Hayashi, S., Itoh, C., Kabuki, S., Kajino, F., Katagiri, H., Kawachi, A., Kifune, T., Kubo, H., Kurihara, T., Kurosaka, R., Kushida, J., Matsubara, Y., Miyashita, Y., Mizumoto, Y., Moro, H., Muraishi, H., Muraki, Y., Nakase, T., Nishida, D., Nishijima, K., Ohishi, M., Okumura, K., Patterson, J. R., Protheroe, R. J., Sakamoto, N., Sakurazawa, K., Swaby, D. L., Tanimori, T., Tanimura, H., Thornton, G., Tokanai, F., Uchida, T., Watanabe, S., Yamaoka, T., Yanagita, S., Yoshida, T., and Yoshikoshi, T.: 2004, *ApJL* **606**, L115

Turner, M. J. L., Abbey, A., Arnaud, M., Balasini, M., Barbera, M., Belsole, E., Bennie, P. J., Bernard, J. P., Bignami, G. F., Boer, M., Briel, U., Butler, I., Cara, C., Chabaud, C., Cole, R., Collura, A., Conte, M., Cros, A., Denby, M., Dhez, P., Di Coco, G., Dowson, J., Ferrando, P., Ghizzardi, S., Gianotti, F., Goodall, C. V., Gretton, L., Griffiths, R. G., Hainaut, O., Hochedez, J. F., Holland, A. D., Jourdain, E., Kendziorra, E., Lagostina, A., Laine, R., La Palombara, N., Lortholary, M., Lumb, D., Marty, P., Molendi, S., Pigot, C., Poindron, E., Pounds, K. A., Reeves, J. N., Reppin, C., Rothenflug, R., Salvetat, P., Sauvageot, J. L., Schmitt, D., Sembay, S., Short, A. D. T., Spragg, J., Stephen, J., Strüder, L., Tiengo, A., Trifoglio, M., Trümper, J., Vercellone, S., Vigroux, L., Villa, G., Ward, M. J., Whitehead, S., and Zonca, E.: 2001, *Astronomy and Astrophysics* **365**, L27

Uson, J. M., Boughn, S. P., and Kuhn, J. R.: 1991, *ApJ* **369**, 46

Völk, H. J. and Atoyan, A. M.: 1999, *Astroparticle Physics* **11**, 73

Weekes, T. C.: 1996, *Space Science Reviews* **75**, 1

Weekes, T. C., Cawley, M. F., Fegan, D. J., Gibbs, K. G., Hillas, A. M., Kowk, P. W., Lamb, R. C., Lewis, D. A., Macomb, D., Porter, N. A., Reynolds, P. T., and Vacanti, G.: 1989, *ApJ* **342**, 379

Weisskopf, M. C., Brinkman, B., Canizares, C., Garmire, G., Murray, S., and Van Speybroeck, L. P.: 2002, *Publ. Astron. Soc. Pac.* **114**, 1

White, D. A., Fabian, A. C., Allen, S. W., Edge, A. C., Crawford, C. S., Johnstone, R. M., Stewart, G. C., and Voges, W.: 1994, *MNRAS* **269**, 589